ABSTRACT

Title of Dissertation:	EXPERIMENTAL EVALUATION AND SIMULATION RESEARCH ON NOVEL VARIABLE REFRIGERANT FLOW SYSTEM
	Xiaojie Lin, Doctor of Philosophy, 2017
Dissertation directed by:	Minta Martin Professor Reinhard Radermacher, Department of Mechanical Engineering

Variable refrigerant flow (VRF) system is a popular building air conditioning system which could provide cooling or heating to individual rooms independently. The system is called “variable refrigerant flow” system due to its capability of regulating the refrigerant flow via the precise control of variable speed compressors and electronic expansion valves in each indoor unit. In this dissertation, an advanced VRF system which could provide space cooling, heating and water heating is experimentally evaluated in cooling and heating season for both heat recovery operation and water

heating operation. The VRF system is simulated in EnergyPlus and validated with experimental data. Based on the deviation analysis and literature review, it is found that the existing VRF model could not fully reflect the operation characteristic of VRF systems, leading to a high uncertainty in cooling/heating energy and energy consumption. A new VRF model is thereafter proposed, validated in this research and resulted in a model uncertainty less than 5%. Based on the new model, the seasonal performance of an energy saving control strategy and the concept of chilled water storage are investigated. Meanwhile, to solve the mismatch between the building's thermal load and cooling/heating capability of the VRF system, a new VRF system with phase change material (PCM) based thermal energy storage (TES) is proposed. The new VRF system utilizes single TES device to support both cooling and heating season operation. The performance of new VRF system with PCM based TES is investigated and compared to that of the baseline VRF system. It is found that the new VRF system with PCM based TES could achieve both energy efficiency and demand response goals in cooling and heating season. Based on the comparison, the effect of operation strategies and grid incentive program are discussed. Finally, the economic analysis of the new VRF system with PCM based TES based on annual performance is carried out.

EXPERIMENTAL EVALUATION AND SIMULATION RESEARCH OF NOVEL VARIABLE REFRIGERANT FLOW SYSTEM

By

Xiaojie Lin

Dissertation submitted to the Faculty of the Graduate School of the
University of Maryland, College Park, in partial fulfillment
of the requirements for the degree of
Doctor of Philosophy
2017

Advisory Committee:

Professor, Jelena Srebric, Chair

Associate Professor, Peter Sunderland, Dean's Representative

Associate Professor, Nikhil Chopra

Professor, Marino diMarzo

Research Professor, Yunho Hwang

Dedication

In dedication to my grandfather

You are loved by your family and will always be.

Acknowledgement

I would like to thank my advisor Prof. Reinhard Radermacher for his support and advice during my PhD study in CEEE. His insights and vision in this area always inspire me. Prof. Reinhard Radermacher once said: “Have your own plan. Otherwise, you become part of other people’s plan”. I will never forget that. I would also thank Prof. Yunho Hwang for his support and invaluable advice during my PhD study. Prof. Yunho Hwang’s advice of “24+α” is by far the most useful life tip I have ever heard of. It always encourages me to explore more in this area. I also very grateful to my committee members: Dr. Srebric, Dr. diMarzo, Dr. Sunderland and Dr. Chopra. I would like to offer a special note of thanks to Dr. Srebric for her help during my dissertation. I also want to thank Dr. Hoseong Lee for his help and continuous guidance. He taught me how to be a professional researcher.

I would also thank Gang Li, Jan Muehlbauer, Dr. Jiazhen Ling, Dr. Hongtao Qiao and Dr. Suxin Qian for their help. Jan’s expertise and passion keep inspiring me to be a dedicated engineer. Dr. Qian’s advice is always insightful. Dr. Qiao gave me a lot of help in understanding the behavior of transient system. I would also thank all my colleagues in CEEE for all these helpful and illuminating discussions. I also want to express my gratitude to LG Electronics. This work could not be possible without their support. I really enjoyed the discussions with LG engineers. Their work ethic is impressive.

My deep thanks go to my parents and grandparents. Without their understanding and love, this work will never be possible. Last but not least, I would like to thank my girlfriend, Xinyi Ren, for her support and love during the tough times.

Table of Contents

Dedication ii

Acknowledgement iii

Table of Contents v

List of Tables ix

List of Figures xi

1 Introduction 1

2 Literature Review 4

2.1 Variable Refrigerant Flow System Working Principles 4

2.2 Experimental Study 9

2.3 Dynamic Modeling 15

2.3.1 History 15

2.3.2 Dynamic Models 17

2.3.3 Model Validation 25

2.4 Thermal Energy Storage 30

2.4.1 Overview 30

2.4.2 Air Conditioning with Phase Change Material 37

2.5 Research Gaps and Objectives 46

3 Experimental Evaluation of Multi-Functional Variable Refrigerant Flow System 49

3.1 Experiment Setup 49

3.1.1 Test Facility 49
3.1.2 Measurement 52
3.1.3 Test Conditions 54
3.1.4 Data Reduction 56
3.2 Results and Discussion 59
3.2.1 Effect of Water Heating 59
3.2.2 Effect of Heat Recovery Operation 66
4 New Dynamic Modeling of Variable Refrigerant Flow System 70
4.1 Model Improvement Discussion 70
4.2 Mapping Model Deviation Analysis 71
4.2.1 Water Heating Unit 71
4.2.2 Cooling and Heating Season Simulation 72
4.2.3 Hourly Data Analysis 77
4.3 New Modeling Approach 79
4.3.1 New Thermal Zone Concept 83
4.3.2 Water Heating Unit Modification 87
4.3.3 New Thermodynamic VRF Model 88
4.4 Results and Validation 92
4.4.1 Cooling Energy Validation 92
4.4.2 Energy Consumption Validation 95
4.5 Model Extensibility: Energy Saving Control 97
4.5.1 Variable-Speed System Control 98
4.5.2 Conventional VRF Control 102

4.5.3 Energy Saving Control 104
4.5.4 Seasonal Performance of Energy Saving Control 105
4.6 Model Extensibility: VRF with Chilled Water Storage 108
4.6.1 VRF with Chilled Water Storage 108
4.6.2 Seasonal Performance 111
5 Variable Refrigerant Flow System with Phase Change Material Based Thermal Energy Storage 114
5.1 New VRF System with PCM based TES Configuration 114
5.2 Operation Scenario 118
5.2.1 Overall Architecture 118
5.2.2 Operation Scheme 123
5.3 Preliminary Design Month Analysis 126
5.4 Phase Change Material Integrated Heat Exchanger 130
5.4.1 Phase Change Material Selection 130
5.4.2 Phase Change Material Integrated Heat Exchanger Design 132
5.4.3 Phase Change Material Integrated Heat Exchanger Simulation 138
5.4.4 Modeling Flowchart 151
5.5 Results and Discussion 154
5.5.1 Design Month Performance 154
5.5.2 Economic Analysis 168
6 Conclusions and Future Work 172
6.1 Conclusions 172
6.2 Future Work 175

6.3 Contributions..... 176

6.3.1 List of Contributions..... 176

6.3.2 List of Publications..... 177

Abbreviation 179

Symbols.....181

Reference 187

List of Tables

Table 2-1 Summary of experimental studies 10

Table 2-2 Summary of dynamic modeling studies 19

Table 2-3 Summary of dynamic VRF model validation studies..... 29

Table 2-4 Comparison of different energy storage options 35

Table 2-5 PCM in building HVAC..... 44

Table 3-1 System nominal capacities 50

Table 3-2 Specifications of instrument..... 53

Table 3-3 Cooling main test..... 55

Table 3-4 Heating main test..... 55

Table 4-1 Deviation reduction 76

Table 4-2 Validation criteria..... 81

Table 4-3 Detailed information of rooms 85

Table 4-4 Cooling and heating capacity of system..... 85

Table 4-5 CvRMSE and NMBE in hourly cooling energy validation..... 95

Table 4-6 CvRMSE and NMBE in hourly energy consumption validation 97

Table 4-7 Built-in cooling operation control parameters..... 103

Table 4-8 Control strategy comparison..... 104

Table 4-9 New control strategy cooling energy saving variation by location 108

Table 4-10 New control strategy heating energy saving variation by location 108

Table 4-11 VRF with CWS energy saving variation by location 113

Table 5-1 PCM comparison..... 131

Table 5-2 Designed PCM integrated heat exchanger 137

Table 5-3 Material properties..... 143

Table 5-4 Fin efficiency..... 144

Table 5-5 Refrigerant side heat transfer coefficient calculation..... 147

Table 5-6 Hourly average melting/solidification power..... 149

Table 5-7 Cooling incentive programs 166

Table 5-8 Heating incentive programs..... 167

Table 5-9 Cost comparison between new system and conventional system 170

List of Figures

Figure 2-1 Schematic diagram of HPVRF system in cooling mode 5

Figure 2-2 Schematic diagram of HRVRF system in cooling main mode 6

Figure 2-3 Schematic diagram of HRVRF system in heating main mode 6

Figure 2-4 Schematic diagram of MFVRF system 9

Figure 2-5 Typical HPVRF model flowchart (Zhou and Wang 2006) 21

Figure 2-6 TES categories 31

Figure 2-7 Working process of strontium chloride and ammonia pair (Li *et al.* 2015) 32

Figure 2-8 Melting temperature and fusion energy of PCM (Dieckmann 2016; Li *et al.* 2012) 37

Figure 2-9 Three types of phase change material storage design (Mehling *et al.* 2008) 38

Figure 2-10 PCM integrated into wall: space heating (Schossig *et al.* 2005)..... 43

Figure 2-11 PCM integrated into ceiling: space cooling (Stritih and Butala 2010) ... 43

Figure 2-12 Energy efficiency and demand response (Palensky and Dietrich 2011). 46

Figure 3-1 Schematic Diagram of MFVRF system 51

Figure 3-2 Variation of DPF with outdoor temperature 60

Figure 3-3 Variation of energy consumption with cooling energy..... 60

Figure 3-4 Variation of DPF with HRR..... 61

Figure 3-5 Variation of pressure ratio with compressor frequency 61

Figure 3-6 Variation of PLR with average outdoor temperature..... 64

Figure 3-7 Variation of DPF with average outdoor temperature 64
Figure 3-8 Variation of compressor frequency with PLR 65
Figure 3-9 Variation of DPF with PLR..... 65
Figure 3-10 Variation of HPF with hourly ambient temperature 67
Figure 3-11 Variation of PLR with hourly ambient temperature 68
Figure 3-12 Variation of discharge pressure with ambient temperature..... 68
Figure 3-13 Variation of pressure ratio with ambient temperature..... 69
Figure 4-1 MFVRF mapping method model flowchart..... 72
Figure 4-2 Hourly cooling energy validation..... 74
Figure 4-3 Hourly cooling energy consumption validation..... 75
Figure 4-4 Hourly heating energy validation..... 75
Figure 4-5 Hourly heating energy consumption validation 76
Figure 4-6 Compressor frequency in overestimated region..... 78
Figure 4-7 Compressor frequency in underestimated region..... 79
Figure 4-8 New VRF model flowchart 82
Figure 4-9 Floor plan 84
Figure 4-10 Original building thermal zone 84
Figure 4-11 Proposed thermal zone distribution..... 87
Figure 4-12 Thermodynamic VRF model..... 92
Figure 4-13 Hourly cooling energy validation with previous building thermal zone. 94
Figure 4-14 Hourly cooling energy validation with proposed building thermal zone 94
Figure 4-15 Hourly cooling energy consumption validation with previous approach 96

Figure 4-16 Hourly cooling energy consumption validation with proposed new model 97
Figure 4-17 Variable-speed system cooling capacity control 101
Figure 4-18 Variable-speed system heating capacity control 101
Figure 4-19 Conventional VRF control 102
Figure 4-20 Hourly cooling energy consumption validation with conventional VRF control 103
Figure 4-21 Daily energy consumption comparison between two control strategies in cooling (Miami, FL) 106
Figure 4-22 Daily energy consumption comparison between two control strategies in heating (Chicago, IL) 107
Figure 4-23 VRF with CWS in charging mode 110
Figure 4-24 VRF with CWS in discharging mode 110
Figure 4-25 Flowchart of VRF with CWS 111
Figure 4-26 Daily energy consumption comparison for VRF systems with and without CWS (Miami, FL) 112
Figure 5-1 Overview of new VRF system with PCM based TES 116
Figure 5-2 New VRF system with TES cooling mode: PCM solidification 116
Figure 5-3 New VRF system with TES cooling mode: PCM melting 117
Figure 5-4 New VRF system with TES heating mode: PCM melting 117
Figure 5-5 New VRF system with TES heating mode: PCM solidification 118
Figure 5-6 Overall architecture of demand response and energy efficiency operation 119

Figure 5-7 Time-of-use pricing 121
Figure 5-8 Time-of-use with critical peak pricing 122
Figure 5-9 Day-ahead real-time pricing 122
Figure 5-10 Time-wise operation illustration 124
Figure 5-11 Energy consumption and congestion of operation 124
Figure 5-12 Cost of operation 125
Figure 5-13 Cooling: effect of melting temperature on energy consumption reduction 128
Figure 5-14 Cooling: effect of melting temperature on congestion reduction 129
Figure 5-15 Heating: effect of melting temperature on energy consumption reduction 129
Figure 5-16 Heating: effect of melting temperature on congestion reduction 130
Figure 5-17 Solidification of PCM outside a tube segment 133
Figure 5-18 Designed PCM heat exchanger 138
Figure 5-19 Melting process considering fin effect 140
Figure 5-20 Fin temperature decay 145
Figure 5-21 Segment heat transfer calculation 148
Figure 5-22 Cooling operation: hourly PCM solidification 149
Figure 5-23 Cooling operation: hourly PCM melting 150
Figure 5-24 Heating operation: hourly PCM solidification 150
Figure 5-25 Heating operation: hourly PCM melting 151
Figure 5-26 Model flowchart change of VRF with PCM based TES 153
Figure 5-27 Operation sequence generation method 154

Figure 5-28 Cooling: typical 24-hr energy consumption of new VRF system..... 156
Figure 5-29 Cooling: typical 24-hr status of PCM based TES 156
Figure 5-30 Heating: typical 24-hr performance of new VRF system 157
Figure 5-31 Heating: typical 24-hr status of PCM based TES 157
Figure 5-32 Cooling: hourly COP comparison between new system and baseline system 159
Figure 5-33 Heating: hourly COP comparison between new system and baseline system 160
Figure 5-34 Cooling: effect of operation strategy on design month energy saving.. 162
Figure 5-35 Cooling: effect of operation strategy on design month cost reduction . 163
Figure 5-36 Cooling: effect of operation strategy on design month congestion reduction 163
Figure 5-37 Heating: effect of operation strategy on design month energy saving.. 164
Figure 5-38 Heating: effect of operation strategy on design month cost reduction.. 164
Figure 5-39 Heating: effect of operation strategy on design month congestion reduction 165
Figure 5-40 Effect of cooling season incentive programs on cost reduction..... 167
Figure 5-41 Effect of heating season incentive programs on cost reduction..... 168
Figure 5-42 Monthly cost savings with day ahead real-time incentive program..... 170
Figure 5-43 Monthly cost savings with day ahead real-time incentive program (double gap) 171

1 Introduction

In the modern society, building air condition system is a necessity to daily life. With the technical advancement in air conditioning industry, the concept of air conditioning has been also changed. The concept of air conditioning has changed from cooling in single zone to a comprehensive cooling solution for the whole building, including space heating, space cooling, ventilation and even hot water supply. Together with widespread building air conditioning system, the energy consumption and efficiency of the system naturally become one of the central topics in both building and air conditioning industry.

According to the 2011 building data book published by Department of Energy (DOE), in 2010, the building section consumed 41.1% of the primary energy(Department of Energy 2012), followed by the transportation industry sector. Within the building energy sector, the split of primary energy based on end-use shows that space cooling, space heating and water heating account for 22.5%, 14.8% and 9.0% of the primary energy consumed by the whole sector. It can be concluded that the building air conditioning and water heating system account for 18.6% of the whole primary energy consumed by the whole United States. Therefore, the energy saving of the building air conditioning system is key to the energy saving of the whole building.

Variable refrigerant flow (VRF) system, also knowns as variable refrigerant volume (VRV) system, is one of the widely used type of building air conditioning systems. When compared with traditional air conditioning or heat pump system, VRF systems are well-known for its installation flexibility and systematic modularity. VRF system

usually consists of multiple direction expansion indoor units (IUs), a variable speed compressor, several electronic expansion valves (EEVs) and flow rate distribution units. The system could provide a precise control of the refrigerant flow rate via the cooperation of variable speed compressor and EEVs. Meanwhile, the system also allows individual control of each IU. Therefore, VRF systems are also regarded as multi-split system or multi-evaporator system in the open literature.

Since 2008, the VRF technology has underwent a rapid development. Conventional heat pump VRF systems and heat recovery VRF systems have been experimentally evaluated by researchers. One trend in both industry and academia is to introduce more functions in the VRF system to make it a comprehensive building air conditioning solution in both residential and commercial buildings. Meanwhile, because the VRF systems are widely used as a building HVAC solution, the performance estimation of building VRF systems with building energy simulation tools has also become the interest of research. With the development of new VRF technology, it is necessary to create new tools to simulate the new VRF systems. Moreover, in addition to the energy efficiency (EE) operation, the future VRF system should also be able to take the demand response (DR) operation into consideration. This dissertation covers both the simulation and experimental study of novel VRF systems. In this dissertation, a comprehensive review of the recent development of novel VRF technologies is carried out in Chapter 2. Based on the research gaps found in literature view, the research objectives of this study are thereby formulated and fulfilled in the following chapters. Chapter 3 focuses on the experimental set up and field testing of a multi-functional VRF system. Chapter 4 focuses on the development of new dynamic VRF model.

Chapter 5 focuses on the development of a novel VRF system with thermal storage capability.

2 Literature Review

2.1 Variable Refrigerant Flow System Working Principles

There are two main categories of the VRF systems available in the commercial market: a heat pump type VRF (HPVRF) system and a heat recovery type VRF (HRVRF) system. For either kind of VRF system, the following components could be usually found:

- Compressors with capacity regulation capability, such as variable speed compressors
- Electronic expansion valves
- Operation mode regulation components, such as HRUs and MCUs
- Variable speed fans

Accumulators are also widely used in VRF system. Moreover, for high-capacity VRF systems, it is also common to have receivers.

Literally, the core difference between the two types of the system is whether the system is capable of conducting heat recovery operation among the indoor units. The HPVRF system could operate only in either cooling or heating mode. A schematic diagram of the typical HPVRF in cooling operation mode is shown in Figure 2-1.

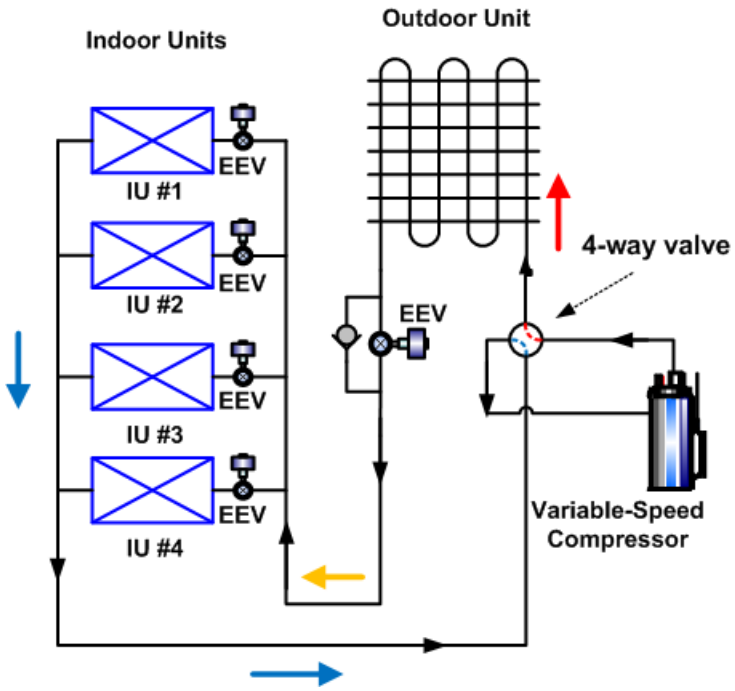

Figure 2-1 Schematic diagram of HPVRF system in cooling mode

The working principle is similar to that of a typical vapor compression system except having multiple indoor units. In the cooling operation, the refrigerant flow discharged from the compressor is condensed to the subcooled liquid phase in the outdoor heat exchanger (HX), flows through the check valve and supplied to indoor units. In the indoor units, the refrigerant is first expanded through EEVs, evaporated to superheated vapor phase by absorbing heat from air through the indoor HX, and returns to the compressor. In the heat pumping operation, the direction of the refrigerant flow is reversed by the four-way valve so that the function of indoor and outdoor HXs can be switched. The working principle of the HRVRF is shown in Figure 2-2 and Figure 2-3, which have four IUs and one OU as an example.

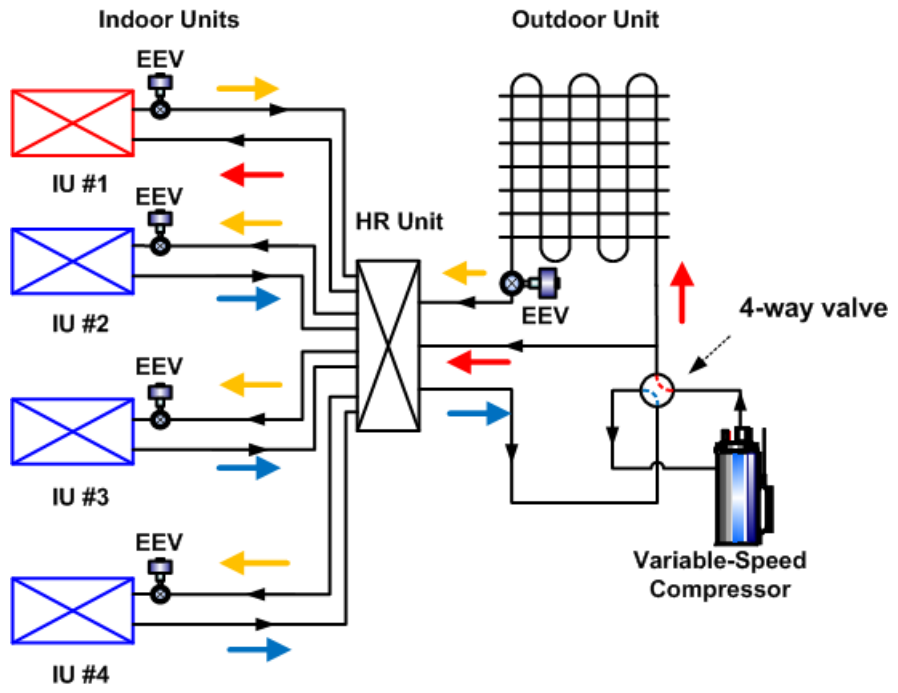

Figure 2-2 Schematic diagram of HRVRF system in cooling main mode

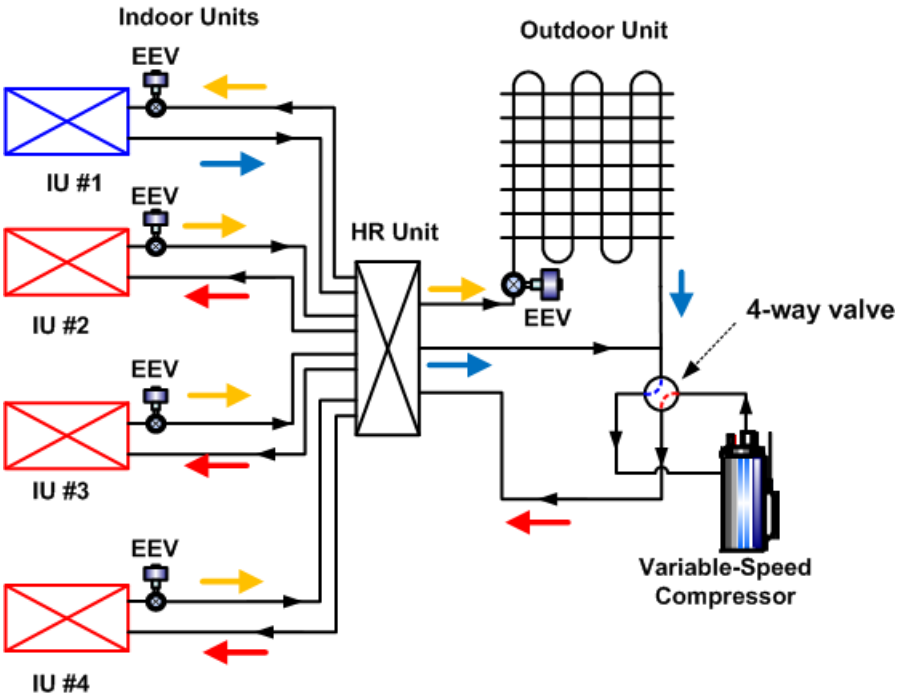

Figure 2-3 Schematic diagram of HRVRF system in heating main mode

The main components of the system are similar to the HPVRF except the heat recovery unit (HRU) installed between the indoor and outdoor units. With a HRU, the HRVRF system supports more operating modes than the HPVRF. It could provide five modes of operating: cooling only, heating only, cooling main, heating main and balanced operation (cooling and heating balanced operation). The cooling only and heating only modes are same as those of the HPVRF system. The cooling main operation mode means that the system has concurrent cooling and heating demands while the cooling demand is higher than the heating demand. Similarly, in the heating main operation mode the system has a higher heating demand than the cooling demand. The balanced operation mode means that the system has a balanced cooling and heating load. Figure 2-2 shows the HRVRF system working in a cooling main mode (IU#1 in heating mode, the rest of IUs in cooling mode). The refrigerant discharged from the compressor is divided into two flows: a part of the refrigerant is supplied to the OUHX while the rest bypasses the condenser and is directly supplied to HRU. The refrigerant supplied to the OU HX is condensed and expanded through the EEV before it enters the HRU. In the HRU, two streams of refrigerant at different states (high pressure superheat vapor and subcooled liquid) are distributed to individual IUs according to the thermal load in each IU. The refrigerant leaving the IU under heating operation returns to the HRU and is mixed with the flow from the OUHX, and is redistributed by the HRU, which means it could be used to cool down the other rooms. In this process, the heat is recovered and the system could provide cooling and heating at the same time. The key component of heat recovery operation is the HRU. The HRUs are designed to temporarily store and thereafter deliver a precise amount of refrigerant to the IUs during the operation of the

system. Therefore, the inlet of a HRU would be connected to OU via three pipes, i.e., reflecting three different possible states of refrigerant leaving OU. Such a HRVRF is also regarded as three-pipe HRVRF system. Manufactures have also developed two-pipe HRVRF systems which require only two pipes. Similarly, the outlet of the HRUs is connected to IUs through refrigerant ports. These ports provide IUs access to different states of refrigerant through solenoid valves, thus provide cooling or heating to the room. The HRUs could have further capabilities which can improve the reliability and efficiency of the system. For example, in the cooling operation, HRUs could have a bypass valve in the liquid refrigerant line, thus precisely controlling the amount of refrigerant available to the cooling indoor IUs. The HRVRF could also be used in buildings with different loads in winter season as shown in Figure 2-3. In Figure 2-3, IU#1 is in cooling mode while the rest of IUs are in heating mode. Based on the concept of heat recovery, the indoor units of the HRVRF system could also include a water heater or water chiller. For example, it is possible to have a refrigerant-to-water heat exchanger to provide service hot water and/or service chilled water to the buildings. Such a VRF system is called as a multifunctional VRF (MFVRF) system (Kwon *et al.* 2012a, Kwon 2013, Kwon *et al.* 2014, Lin *et al.* 2014). As shown in Figure 2-4, the VRF has a refrigerant-to-water heat exchanger for water heating. The water heater could be regarded as a special indoor unit which is always in heating mode. The advantage of a MFVRF system is the generation of useful hot water by using waste heat.

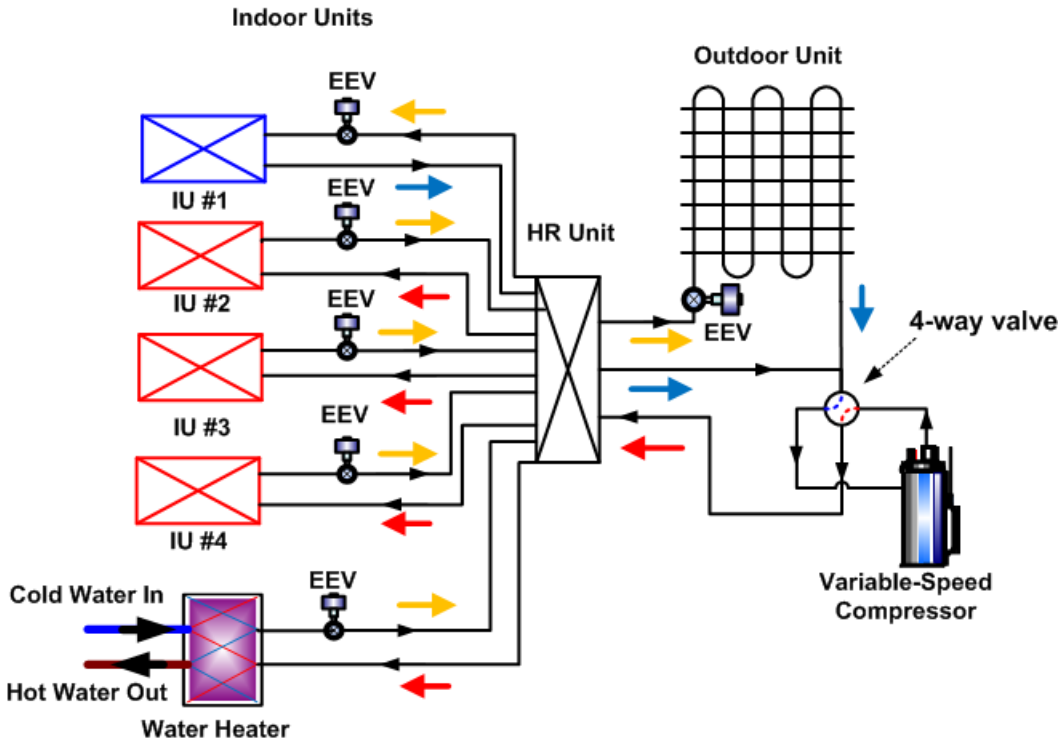

Figure 2-4 Schematic diagram of MFVRF system

2.2 Experimental Study

The existing experimental study focused on the investigation of the operation characteristics of the system under one or more modes. The possible basic operating modes of a typical VRF system are as follows: (1) cooling only operation, (2) heating only operation (heat pump mode), (3) cooling main operation (heat recovery mode), (4) heating main operating (heat recovery mode), (5) balanced heating and cooling operation (heat recovery mode), (6) defrosting operation, and (7) oil return operation. The existing experiment studies are summarized in Table 2-1 and their highlights are also included.

Table 2-1 Summary of experimental studies

Authors (Year)	Type	IU #	OU Capacity (kW)	Modes	Note	Highlights
Fujimoto *et al.* (2011a)	HP	4	28	Cooling	Laboratory test	Increase evaporating temperature
Fujimoto *et al.* (2011b)	HP	4	28	Cooling	Laboratory test	Compare three methods of evaluation
Zhang *et al.* (2011)	HP	4	31.5	Cooling, Heating	Laboratory test	Capacity modulation scroll compressor
Tu *et al.* (2011)	HP	5	30	Cooling	Laboratory test	Capacity modulation scroll compressor controller
Kwon *et al.* (2012)	HP	6	23	Cooling	Field test	Subcooler heat exchanger
Jiang *et al.* (2014)	HP	6	28	Cooling, Heating	Field test	Temperature and humidity control with solid desiccant

Tu *et al.* (2012)	HP	5	45	Defrosting	Laboratory test	Defrosting criterion
Kang *et al.* (2009)	HR	4	11.5	Cooling, Heating, Heat recovery	Laboratory test	Regulate EEV opening
Joo *et al.* (2011)	HR	4	11.5	Cooling, Heating, Heat recovery	Laboratory test	Part load operation
Kwon *et al.* (2014)	MF	7	35	Heat Recovery in Heating Season	Field test	Introduce water heating capability

Fujimoto *et al.* (2011a) investigated the laboratory evaluation methods of VRF system and compared three different approaches based on air enthalpy method used in Japanese Industrial Standards (JIS). The compressor curve method was found to be the best, followed by the refrigerant mass flow meter method. Fujimoto *et al.* (2011b) also discussed the improvement by introducing a modified control when the unit was not in active cooling mode. It was found the COP could be improved from 3.44 to 4.64. Kang *et al.* (2009) and Joo *et al.* (2011) investigated the part load and full load performance of a VRF system in the laboratory conditions under five different modes (cooling only, heating only, entire heat recovery, cooling main and heating main). The EEVs (either

in the IUs or OU) were regulated such that the capacity of the indoor units reached the rated capacity. In the cooling main mode, the EEV opening of the OU was regulated to change the bypass ratio of the refrigerant. The optimal performance was obtained with a bypass ratio of 27%. In the heating main mode, two control strategies were used: decreasing the opening of the outdoor EEV and increasing the EEV opening of the cooling indoor units. It was found that the COP improvement under a balanced heating and cooling condition could be 7.69, 146.5% higher than the cooling only operation due to both the increase of total capacity and the decrease of the compressor energy consumption. In the field testing part, Kwon *et al.* (2012b) investigated the effectiveness of the subcooler heat exchanger (SCHX), which used the subcooled refrigerant to preheat the suction line refrigerant. In SCHX, part of the inlet liquid refrigerant expanded in EEVs and cooled down the rest liquid refrigerant. Bypass ratio was defined as the ratio of refrigerant mass flow rate through EEV to the total mass flow rate. Kwon *et al.* (2012b) investigated the cooling performance factor and the mass flow rate across the SCHX within a bypass EEV opening range from 0 to 20%. With a higher opening, the refrigerant mass flow rate of the indoor units could be reduced, leading to a lower cooling energy. However, the subcooler heat exchanger also reduced the condensing pressure of the system. It was found that with a bypass rate of 5.3%, the system could obtain an optimal COP, which was 8.7% higher than the baseline VRF system. Kwon *et al.* (2014) also conducted field testing of a MFVRF system with the capability of providing hot water. The system was able to provide space cooling, heating and service hot water at the same time. The tests were conducted during the heating season to investigate the performance of the system in heat recovery

operation. It was found that the hot water demand could improve the part load performance of the system. Moreover, the heat recovery effect between the cooling units and heating units also contributed to the enhancement of the performance. A daily performance factor of 2.14 and 3.54 was observed when the ratio of the cooling energy to the daily total energy (space cooling, heating and water heating) was 13.0% and 28.4%, respectively. The authors found that a reduced pressure ratio across the compressor contributed to the energy saving.

It should be pointed out that the current research found in the open literature mainly focused on the heating and cooling operation modes rather than operation modes such as defrosting mode and oil recovery mode. As for the defrosting mode, Tu *et al.* (2012) experimentally investigated the defrosting operation of VRF systems. Their work developed a defrosting criterion in terms of time, coil temperature and condensation temperature. The criterion was defined in four ranges of outdoor temperature: lower than -9°C, from -9°C to 0°C, from 0°C to 4°C and from 4°C to 21°C. The defrosting criterion also included a criterion time constant and accumulative coefficient to provide a minimum defrosting cycle. It was suggested that the reasonable defrosting time should be five minutes.

Regarding the researches focusing on VRF system component, Zhang *et al.* (2011) and Tu *et al.* (2011) applied a capacity modulation scroll compressor to the VRF system. Zhang *et al.* (2011) described the relationship between the performance of the system and the part load ratio. The performance of the system under cooling and heating conditions was found to be optimal when under a certain range of the part load ratio. However, the authors didn't provide more details on the part load testing methodology

of the system. They also analyzed the performance of VRF system based on hourly cooling and heating performance data and claimed that none of three efficiency related factors (EER, IPLV and SEER) was a satisfying criterion to rate the performance of the system. Tu *et al.* (2011) focused on the control design and stability of the capacity modulation scroll compressor system based on pulse width modulation (PWM) valve. The control algorithm adapted from inverter compressor was tested first but was not able to stabilize the system. The second algorithm, proposed based on period averaged suction pressure, was designed and tested. It was found that with the new method, the capacity modulation scroll compressor based system could achieve an outlet air temperature with a deviation less than 0.2 K.

New VRF systems, which could be differentiated by either new capabilities such as water heating or new components such as desiccant material, were also found in the experimental study. Jiang *et al.* (2014a, 2014b) experimentally studied the performance of a novel VRF system with a solid desiccant heat pump. The basic idea was to realize temperature and humidity independent control (THIC) of the air. The approach was to separate the sensible and latent load of the VRF system while introducing fresh air into the buildings. It was realized by two desiccant coated heat exchangers. By switching the mode of the solid desiccant unit, desiccant material kept absorbing the moisture and was regenerated. The experimental study was divided into two parts: cooling season and heating season. To show the energy saving potential of the integrated solid desiccant and VRF system (IDVS), a joint heat recovery ventilation and VRF system (JHVS) was also built. The two systems were compared to see the energy saving and

performance improvement of the IDVS. It was found that system could increase the COP by 25.7% and 45.2% in cooling and heating season, respectively.

From Table 2-1, it could also be found that, the researches of VRF system start with HPVRF, moves to HRVRF and continues with new VRF systems such as MFVRF. Meanwhile, the studies start with lab testing. After that, the field tests of such systems further indicate the improvement and benefit of the system. These field tests results will also be used during the development and validation of dynamic VRF models.

2.3 Dynamic Modeling

2.3.1 History

Most of the current dynamic modeling studies are based on the building simulation tools, such as EnergyPlus (Li and Wu 2010, Jiang *et al.* 2013, Jiang *et al.* 2014), eQuest (Liu and Hong 2010) and TRNSYS (Zhu *et al.* 2014a, Zhu *et al.* 2014b, Zhu *et al.* 2014c).

There were two major energy simulation tools supported by government funding in 1970s: DOE-2/DOE-2.2 and Building Loads Analysis and System Thermodynamics (BLAST). In later 1990s, EnergyPlus, a new project based on the modular concept of programming, was launched by U.S. Department of Energy as an effort to merge the two tools. While the development of BLAST ceased, DOE-2.2 and DOE-2.2-based software are still in development. For example, eQUEST is based on DOE-2.2. TRNSYS was developed in 1970s independently the tools mentioned above. TRNSYS is based on FORTRAN and the first version developed for Windows was released in 1993. However, TRNSYS has not provided support for VRF system yet.

The reason for researchers to choose these tools is that researchers could obtain thermal load of the buildings once the specification of the building and ambient conditions are given. Therefore, with proper weather data, simulations based on these tools could reveal the energy saving potential of the HVAC systems.

However, these simulation tools usually do not support VRF systems, especially in the earlier versions. Moreover, even if heat pump VRF system is supported, the heat recovery feature could be missing. For example, EnergyPlus did not provide simulation capability of the HPVRF/HRVRF system until version 7.2, which was released in 2012. Therefore, researchers developed different HPVRF/HRVRF models for EnergyPlus. Moreover, EnergyPlus is designed to be a simulation engine used by other building energy simulation packages. However, the development of simulation packages does not always catch up with the development of the engine. Therefore, even though the engine supports VRF system, it is still possible that VRF systems are not supported by third-party tools. For EnergyPlus, Zhou *et al.* (2006, 2007, 2008) developed the earliest HPVRF system model. The outdoor and indoor temperatures were used as the parameters to evaluate the capacity and energy consumption. Each indoor unit was treated as a direct expansion (DX) unit. After all indoor units being simulated, the model calculated the outdoor unit energy consumption. This model was further enhanced in Li *et al.*'s research (2010a, 2010b) to include water-cooling VRF systems and heat recovery operation. The encapsulated model of VRF system in EnergyPlus was developed based on the work done by Florida Solar Energy Center (Raustad 2013; Raustad *et al.* 2013; Nigusse and Raustad 2013). Their studies also evaluated the impact of heat recovery operation by introducing the heat recovery correction factors. Shen *et*

al. (2012, 2013) also developed a HPVRF system model both on EnergyPlus version 6.0 and TRNSYS. The model used the same independent variables as previous methods and a water heater model was included. Hong (2014) proposed a new modeling approach of the VRF system in EnergyPlus 7.2. The improvement in the new approach was that the indoor and outdoor units' air temperatures were used to calculate the capacity and energy consumption. Meanwhile, the fan part in the VRF model was improved by using a variable volume fan instead of a constant volume fan. Zhu *et al.* (2013) proposed a general component simulation framework for VRF systems in TRNSYS. The components of the VRF systems were all simulated as lumped parameter models. The simulation results indicated that the model could agree with the experimental data under different ambient temperature. However, it should also be pointed out that the detailed structure of the VRF system was less discussed by the existing simulation studies. Meanwhile, there were less validation researches when compared to the simulation researches.

2.3.2 Dynamic Models

Existing simulation studies of the VRF system focused on a running period which ranged from one hour to whole year. The studies were carried out in the scope of building energy simulation. These existing studies are summarized in Table 2-2. As can be found, most of the studies were based on EnergyPlus. These studies used different VRF models due to the fact that the earlier versions of EnergyPlus were not able to support VRF systems. These studies emphasized different operation aspects of VRF system such as heat pump operation, heat recovery operation or ventilation. In

addition, there are also some preliminary simulation studies focusing on the comparison between VRF system and ground source heat pump (GSHP).

Table 2-2 Summary of dynamic modeling studies

Authors (Year)	Software	System	Weather Condition	Validation	Model Highlights
Liu *et al.* (2010)	EnergyPlus, eQuest	HRVRF, GSHP	Miami, Chicago	No	GSHP and VRF simulated in eQuest and EnergyPlus
Li *et al.* (2010)	EnergyPlus	Water Source HR VRF	Shanghai	No	New model of water source HRVRF
Pan *et al.* (2012)	N/A	Dual Evaporator System	N/A	No	Effect of piping length; Optimization of OU location
Jiang *et al.* (2013,2014)	EnergyPlus	HPVRF with SDHP	Shanghai	Yes	New model of SDHP;
Hong (2014)	EnergyPlus	HPVRF	California	No	New VRF model
Raustad *et al.* (2013)	EnergyPlus	HRVRF	Measured local weather data	Yes	EnergyPlus official HRVRF model

Shen *et al.* (2012,2013)	EnergyPlus, TRNSYS	HPVRF with Water Heater	N/A	No	New water heater model; new HPVRF model
Zhu *et al.* (2013, 2014)	TRNSYS	VAV-VRF Combined	Shanghai	Yes	VRF model in TRNSYS; Optimal control
Cheung *et al.* (2014)	N/A	Dual Evaporator System	N/A	No	Gray box based VRF model
Wang (2014)	EnergyPlus	HRVRF, GSHP	Chicago, Baltimore, Atlanta	No	Comparison of GSHP and VRF in EnergyPlus

The heat pump VRF system model was firstly propose by Zhou and Wang in 2006. The concept could be explained in Figure 2-5. The EnergyPlus engine firstly calculated the cooling load of individual IUs. The IU model was adopted from the window AC model. After that, the model searched iteratively in two performance maps to find the energy consumption of the OU that could provide such amount of cooling/heating.

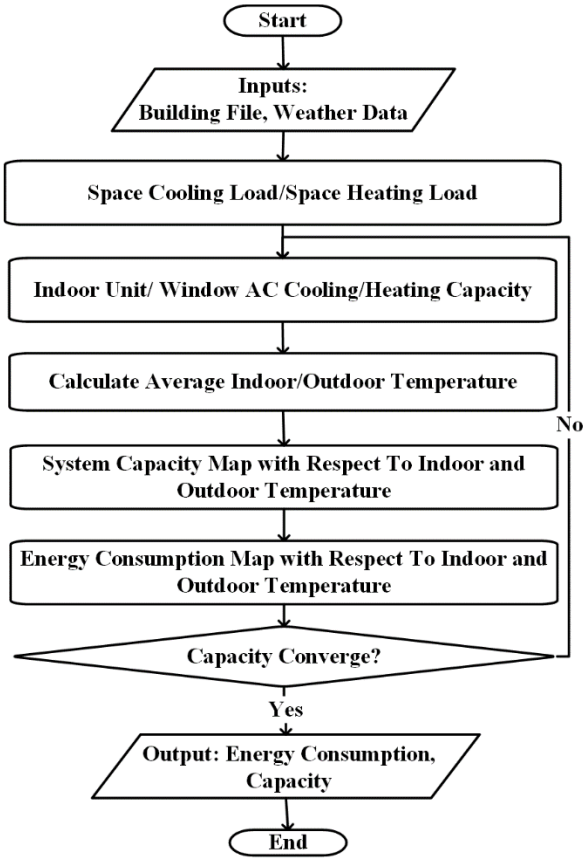

Figure 2-5 Typical HPVRF model flowchart (Zhou and Wang 2006)

This concept was used by other researchers although the individual approach might be different. For example, to account for the heat recovery feature of VRF system, Li *et al.* (2010b) created a HRVRF model in EnergyPlus based on the previously developed heat pump VRF model (Zhou *et al.* 2007; Zhou *et al.* 2008; Zhou and Wang 2006). The proposed model firstly calculated the cooling/heating load and cooling/heating energy consumption of the IUs. The sum of the total cooling load and total cooling energy consumption was compared to the total heating load. If the heating load was higher, the system was in heating dominant mode. If not, the mode of the system was cooling dominant. A comparison between the heat recovery system and the heat pump system

revealed an energy saving of 6% when the set-points for cooling and heating were 25˚C and 19˚C, respectively. The control of the thermostats of the HRVRF was adjusted to allow for a certain dead band temperature to avoid the frequent switch between the operational modes. The energy saving of the HRVRF was then improved to 17%. It was also found that, with a higher set point, the energy saving of HRVRF decreased. After doubling the amount of occupants in the cooling zone, the energy saving of the HRVRF was elevated to 21% when the set points for cooling and heating were 24˚C and 20˚C, respectively.

Despite the better energy efficiency introduced by heat recovery operation, the VRF systems also have its disadvantages in indoor air quality (IAQ) control and indoor ventilation. One possible solution is to have an energy recovery ventilator (ERV). However, the joint control of the ERV and VRF system would be a challenge. The recent development in this area included the introducing of concepts such as desiccant coated heat exchangers and combined VAV-VRF systems.

Jiang *et al.* (2013) simulated a hybrid system of solid desiccant heat pump (SDHP) system and VRF system in EnergyPlus. The overall system was a compound system which combined both VRF and SDHP. The VRF model part was based on the previously developed HPVRF models. The developed SDHP model used the air temperature and humidity of both the outdoor and return air as variables to develop a performance map of the SDHP under ventilation, humidification and dehumidification modes. In this system, the SDHP removed the moisture of the air and VRF system removed the remained (mainly sensible) load of the zones. The SDHP model was validated against the manufacturer's data and the error was less than 15%. It was found

that the humidity and the part load ratio had a significant impact on the system performance. When sensible heat ratio (SHR) was less than 0.5, the VRF system rarely worked. When SHR was higher than 0.5, VRF system took major part of the cooling demand. However, the performance of the system decreased along with the increase of PLR. The combined system was compared to a conventional hybrid system of VRF and heat recovery ventilator. It was found that the combined SDHP and VRF system could save 18.7% of energy annually while yielding a better thermal comfort. Jiang *et al.* (2014) also compared the performance of a desiccant and VRF combined system with two ventilation options: a heat recovery ventilator and standalone ventilation system. The simulation results were compared to experimental data, which showed a deviation of 15% in energy consumption. The COP deviation was within 30%. It was found that the desiccant assisted system consumed less energy than the other two systems. The simulation results also showed that the desiccant VRF systems yielded a COP of 5.3 and 4.6 in summer and winter, respectively.

Zhu *et al.* (2013) proposed a VRF system with an outdoor air (OA) processor to solve the issue of ventilation. A direct expansion rooftop unit provided processed outdoor air to the building. The VAV box thereafter distributed the processed air into different zones according to the IAQ requirements. The VRF system would deal with the rest of thermal load of the zones. The performance of the hybrid system was simulated in TRNSYS. The results were validated against experimental data. The average daily errors of heating energy, energy consumption and COP were 7.87%, 12.45% and 6.19%, respectively. The simulation results showed that the IAQ could be well controlled in all the thermal zones. Zhu *et al.* (2014) further studied the controlling

issues of the combined VAV and VRF system. The performance evaluation of the system revealed that the OA supply temperature would greatly affect the energy consumption of the system. Based on this, the authors investigated the optimal control of the OA supply temperature (Zhu *et al.* 2014). It was found that the real-time optimal control was better than the daily average optimal control method. In heating season, the real-time optimal control could lead to an energy saving of 2.5% with an efficiency improvement of 3.4%. However, in the cooling season, the real-time optimal control of the OA supply temperature could result a 32.2% increase of energy consumption, which lead to a 12.2% drop in efficiency.

Regarding the comparison between other air conditioning systems to the VRF system, Liu *et al.* (2010) simulated and compared the performance of GSHP to air source VRF system in two locations: Miami and Chicago. The VRF system was simulated in EnergyPlus and the GSHP was simulated in eQuest. It was claimed that the GSHP saved 9.4% to 24.1% of energy when compared with VRF system due to the "free" energy obtained from the ground. Wang (2014) also compared GSHP to VRF system in EnergyPlus in different climate zones of USA. The VRF system used in the comparison was the template VRF system in EnergyPlus, which had cooling and heating COP of 3.29 and 3.54, respectively. The GSHP data was claimed to be provided by manufacturers and no details were given. It was also concluded that the GSHP could annually save 20% of energy consumption when compared to air source HRVRF system with a peak saving higher than 31%%. However, the comprehensive and detailed comparison of GSHP and VRF system, both experimentally and numerically, has not been found in open literature yet.

Till this point, most of the researches covered are based on curve-fitting methods. The thermodynamic characteristics of the VRF system were less considered in these studies since the whole unit was calculated as a curve-fitting object. However, there are also some studies simulating the VRF systems based on thermodynamic principles. In general, such VRF models focus on the structure and physical process of the VRF system.

Cheung (2014) simulated a VRF system in a component-based grey box model. The system included two evaporators and one accumulator. The moving boundary methods were used in the heat exchangers. The compressors, EEVs and pressure drop across the piping lines were modeled based on correlation equations. The accumulator was modeled as an ideal gas and liquid separation component. The model was tuned and validated. The model obtained an error within 10% against experimental data. The model was later used for parametric study to see the effect of the indoor air temperature, load ratio, fan speed and indoor load. Pan (2012) investigated the effect of piping length of refrigerant based on a dual-evaporator air conditioning system model. It was concluded and suggested that the highest COP would be achieved when the OU was located equally between the IUs.

2.3.3 Model Validation

The VRF system has been simulated in different models in the researches mentioned above. However, it should be noted that the accuracy of these models is not discussed in details. It is necessary to discuss the accuracy of these models. The existing validation studies are summarized in Table 2-3.

Zhou *et al.* (2007a, 2008b, 2008c) carried out experimental validation of the proposed VRF system model. The validation was carried out in the cooling season considering four aspects: cooling energy, cooling energy consumption, COP and PLR. In the daily data based validation, the average error of cooling energy was 15.4% with a maximum of 27.1%. The average error of energy consumption was 15.6% with a maximum of 32.2%. The COP had an average error of 10.2%. The authors pointed out that the system was not able to capture the cyclic operation during the first hour, which was a typical start-up process. When the first hour data was excluded from the comparison, the COP had an agreement with the experimental data within 5.7%. When the authors included the weekly based experimental data, the average error of energy consumption was 25.2% with a maximum of 36%. The average error of cooling energy was 28.3% with a maximum of 43.6%. The error of COP was found to be 6.4% in average with a maximum of 17%. The PLR was only validated based on weekly data. The deviation of PLR was 18.4% with a maximum of 32.9%. The authors concluded that good agreement could be achieved only when the model could be tuned with more accurate parameters such as the schedules, weather conditions, and specifications of components. In addition, the author also recommended focusing on the relationship between the capacity and energy consumption under different operation conditions. However, the author did not provide the details of processing the experimental data.

Raustad *et al.* (2013) and Sharma and Raustad (2013) also carried out the validation of the EnergyPlus VRF model. The validation was carried out from August to December in 2012. The VRF system had a nominal cooling capacity of 21.1 kW with a cooling COP of 3.8. The nominal heating capacity and COP were 23.4 kW and 3.87,

respectively. The simulated daily energy consumption was compared against the measured data. 72% of the data points were within a deviation of 25% against experimental data. 79% of the data points were within a deviation of 35% against experimental data. The deviation of monthly energy consumption varied in different seasons. In the cooling season, that error was 3%. However, in the heating season, the error could be as high as 30% in December.

In Li *et al.*'s work (2010), the researchers also compared the experimental data to the simulation results of a water-cooled VRF system. Although details of the experimental data processing were not given, the previous study (Zhou and Wang 2006) implied that the proprietary software from the manufactures was used in the processing of the experimental data. The average error of the energy consumption was 33.9%. The average error of cooling energy was 22.4%. The performance of the system was not stable during the last two hours (15:00 ~ 17:00), which caused a higher error. The average error of COP would be 4.8% when data from the last two hour was excluded from the results. If included, the COP error would be 8.3%. The author claimed that the data from the manufacturers could not properly reflect the transient features in the start-up stage. 83% of the measured energy consumption data fell within ±35% deviation of the simulation results; 81% of the cooling energy fell within ±25% deviation of the simulation results. The errors come from following aspects: deviation in the buildings load estimation and the unaccounted components in the system. For example, the model did not include accurate building thermal walls. Meanwhile, the random activity of occupants and the solar radiation also contributed to the error. The authors suggested that a longer period of validation could reduce the uncertainty. The

authors also employed statistical analysis to prove that the simulation could be used to find the relationship between the energy consumption and cooling energy.

Aynur *et al.* (2008) also compared the simulation results to the field testing data of a HPVRF system. It was found that the simulation could capture the indoor conditions. The energy consumption agreed with the experimental data with a ±25% of error. The author accounted two factors for the deviation: The first was that the catalog data provided by the manufacture was not able to capture the "on/off" cycling operation of the inverter compressor. The second was that the solar radiation data was not accurate.

Table 2-3 Summary of dynamic VRF model validation studies

Authors	System	Mode	Deviation (%)				Time Scale
			Cooling/ Heating	Energy Consumption	COP	PLR	
Zhou *et al.* (2006, 2008)	HPVRF	Cooling	15.4	15.5	10.2	N/A	Daily
			28.3	25.2	6.4	18.4	Weekly
Li *et al.* (2010)	Water Source HRVRF	Cooling	22.4	33.9	8.3	N/A	Daily
Aynur *et al.* (2008)	HPVRF	Cooling	N/A	25	N/A	N/A	Daily
Sharma and Raustad (2013)	HRVRF	Cooling; Heating	72% of the energy consumption data were within a deviation of 25%				Daily

In summary, in the validation researches, only the COP of simulated results could agree with the experimental data with a deviation less than 15%. However, the deviation of energy consumption or cooling/heating energy was much higher (15% to 35%). The existing studies discussed two general improvement options: increase the accuracy of

the load estimation and improve the accuracy of the map. However, these options have not been analyzed.

2.4 Thermal Energy Storage

2.4.1 Overview

A longstanding challenge building air conditioning systems face is the fluctuation of building thermal load. The building thermal load is affected not only by the weather, but also by factors such as occupant behavior, lighting, building plug load and even the building management system. Building thermal load is the centerpiece of air conditioning system design. The air conditioning system is usually designed based on the rated design day performance of the building. For example, the design day is selected to make sure the designed system could cover the building thermal load for 96% of the time. However, such design could leads to a redundant system during the off-peak period where the building load is much lower than the cooling delivered by the air conditioning system. The drawback is degradation of the system performance. To solve this issue, thermal energy storage (TES) system is introduced. The human society has a long history of using TES. For example, ice is the most widely used thermal storage material. The attempts of harvesting ice could date back to as early as 1000 B.C. The stored ice could be used to provide cooling to the occupants or to preserve the food. The modern approach of ice-making and refrigeration did not start until the 19^{th} century system. Since then, the development of thermal storage system has been an essential part of HVAC&R industry. With the development of modern air conditioning system, the concept of TES also evolves to include more types of TES. In

addition, TES is also used in industries other than air conditioning, such as solar power generation. In order to apply TES to applications based on different temperature levels, researchers developed the class of phase change material (PCM) based TES, which has a wider operation temperature range than water/ice.

Overall, based on the mechanism behind the energy storage process, TES could be divided into two categories: the chemical process basis and the physical process basis. The physical process based TES can be further divided into sensible heat storage and latent heat storage. The categories are shown in Figure 2-6.

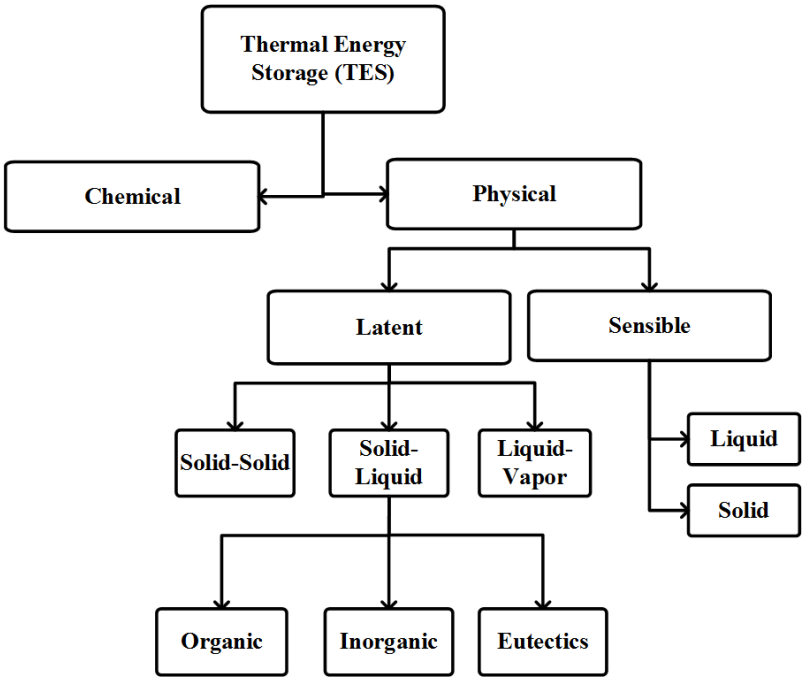

Figure 2-6 TES categories

2.4.1.1 Chemical Energy Storage

The chemical process based TES shown in Figure 2-6 uses the chemical bonds between the molecules to store energy. A typical example is the thermochemical energy storage with a working pair of strontium chloride and ammonia, as shown in Figure 2-7. The

chemical process involved in the chemical storage process could be shown in the following reactions:

$$S_rCl_2 \cdot NH_3 + 7NH_3 \overset{Reaction}{\Longleftrightarrow} S_rCl_2 \cdot 8NH_3 + \Delta H_1$$

$$NH_3(lid) + \Delta H_2 \overset{Phase\ Change}{\Longleftrightarrow} NH_3(gas)$$

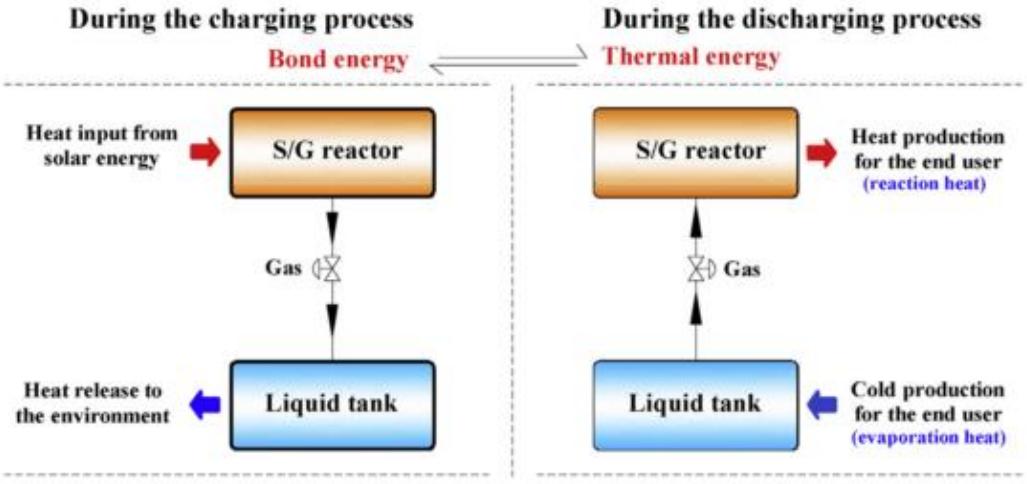

Figure 2-7 Working process of strontium chloride and ammonia pair (Li *et al.* 2015)

The basic concept is to use a heat input such as solar energy to decompose the compound and generate ammonia vapor. The ammonia vapor is cooled to liquid by releasing heat to the ambient. During the discharging process, ammonia absorbs heat from the end users and provides air conditioning or refrigeration. Since the chemical reaction is reversible, the vapor ammonia reacts with strontium chloride and releases the energy stored in the chemical bonds. Based on the reaction pressure, it could provide heating to the end user at different temperatures. As can be seen, the key of chemical thermal storage is to find the proper working pairs. Yan *et al.* (2015) reviewed

and discussed the chemical working pairs used so far by the researchers based on the following perspectives: the applicable temperature range, the complexity of reaction, and necessity of catalysts. Overall, the chemical storage has gain more popularity during the past decade and it could be a future solution for long-term and durable TES.

2.4.1.2 Sensible and Latent Energy Storage

As to the physical storage, the sensible heat is the simplest and most widely used TES solution. The principle of sensible heat storage is to increase the material temperature and use the specific heat as the energy storage. As shown in Figure 2-6, the selection of sensible heat storage could be either liquid or solid. The gaseous material is not used due to the fact that it usually has a low volumetric specific heat and is not suitable as a sensible heat storage solution. Therefore, the common materials used in the sensible heat storage are stones, bricks and water. For example, in the solar heating system, water is widely used as the thermal storage material. In residential applications, water is also used as storage material in domestic heating and hot water supply. The advantage of sensible heat storage is that the technology is well developed. However, the limitation of sensible heat storage is the low energy storage density.

Compared to the sensible storage, latent energy storage has a higher energy density due to the fact that the phase change process is used. Therefore, to provide the same energy storage capability, the latent storage system is much compacter than the sensible system. As shown Figure 2-6, three types of phase change mechanisms could be used: solid-solid, solid-liquid and liquid-vapor. When compared to solid-liquid and liquid-vapor, the solid-solid phase change has a lower energy density and is therefore less used. The liquid-vapor phase change is made up of two parts: evaporation and

condensation. The liquid-vapor phase change mechanism is widely used in absorption system. One of the disadvantages is that the performance of the system is affected by the boundary conditions. For example, the pressure of liquid-vapor system could change dramatically during the charging and discharging process when used in a system with fixed closure. Generally, the term “phase change material” is used to represent the solid-liquid phase change. The solid-liquid phase change process is made up of two parts: solidification and melting. During the solidification process, the material is cooled down. During the melting process, the heat is released by the material. So far, the most widely used latent storage material is ice.

A comparison of different TES is shown in Table 2-4. As can be seen, the mass specific enthalpy of water is 84 kJ/kg. However, the mass specific enthalpy of ice-water fusion is 330 kJ/kg. The evaporating enthalpy of water is even higher, at 2450 kJ/kg. The chemical energy storage based on hydrogen oxidation has a high mass specific enthalpy of $1.2e^5$ kJ/kg. However, the volume of the chemical storage is much larger than latent and sensible energy storage. As can be seen in Table 2-4, the volumetric specific enthalpy of water sensible storage is 1000 times higher than that of the chemical storage.

Table 2-4 Comparison of different energy storage options

	Mass Specific Enthalpy (kJ/kg)	Volumetric Specific Enthalpy (kJ/m^3)	Notes
Sensible Heat			
Water	84	84e3	ΔT=20K. Cheap. Needs large installation space
Latent Heat: Solid-liquid			
Water/Ice	330	3.1e6	Melt at: 0°C. Compact. Needs chiller system
Paraffin	~200	~1.8e6	Melt at: 5°C~130°C. Wide temperature Range. Low conductivity
Latent Heat: Liquid-vapor			
Water	2450	2.45e6	Atmospheric Pressure
Chemical Reaction			
Hydrogen oxidation	1.2e5	1.1e3	Atmospheric Pressure, 30°C

In this study, PCM refers to materials which store and release energy through the solid-liquid phase change process. As shown in Figure 2-6, they could be categorized into

three types: organic, inorganic and eutectics (Sharma *et al.* 2009). The melting temperature range and fusion energy of PCMs by chemical structures are shown in Figure 2-8 (Dieckmann 2016; Li *et al.* 2012). From Figure 2-8, it could be found that different chemical structures lead to different thermal energy storage temperature level. For example, melting temperature of the fluorides could be as high as 800°C while that of the fatty acids is close to 0°C. That is due to the fact that fusion process is affected by the molecular structure of the material. Therefore, materials within the same class have similar properties. Materials with a higher melting temperature, higher molecular weight and more chemical bonds also have high fusion energy. As shown in Figure 2-8, the carbonates have a higher fusion energy than paraffin. As Li *et al.* (2012) pointed out, the PCMs for the air conditioning system lay on the following categories: salt hydrates, eutectics, paraffin, fatty acids and refrigerant hydrates. As shown in Figure 2-8, eutectics have a melting temperature less than 0°C. Organic materials such as paraffin and inorganic materials such as salt hydrates have a higher melting temperature than eutectics. However, inorganic materials have corrosion issues when used with metal containers. On the other hand, paraffin has a better chemical stability. Moreover, it could support a wide range of melting temperature by changing the ingredients in the paraffin mixture. Besides, paraffin is a byproduct of industrial process and its price could be as low as $1/kg. Therefore, it is by far the most used type of PCM.

The selection of PCM should consider both physical and technical requirements (Cabeza *et al.* 2011). As to the physical requirements, PCM should have a narrow melting/solidification temperature range that matches the application. Meanwhile, the

enthalpy change during the phase change process should be high. In addition, the material should have a high conductivity to enhance the heat transfer performance. Technically, PCM should be non-toxic and non-flammable which means a high chemical stability. To ensure the PCM could be applied to various occasions, PCM should also be compatible with different containers without corrosion.

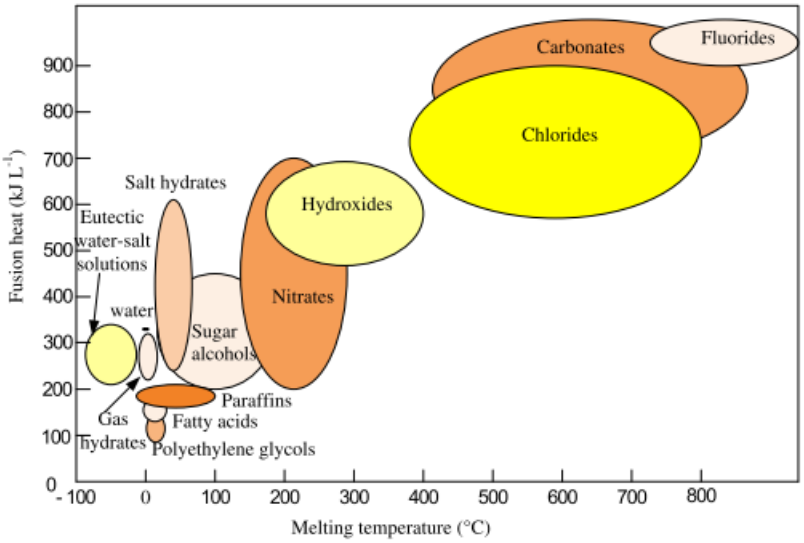

Figure 2-8 Melting temperature and fusion energy of PCM (Dieckmann 2016; Li *et al.* 2012)

2.4.2 Air Conditioning with Phase Change Material

To utilize PCM, it is necessary to take a look at the design of PCM heat exchangers. There are three basic designs: exchanging heat at the surface of PCM, within the PCM and direct exchange of the PCM. The difference could be shown in Figure 2-9.

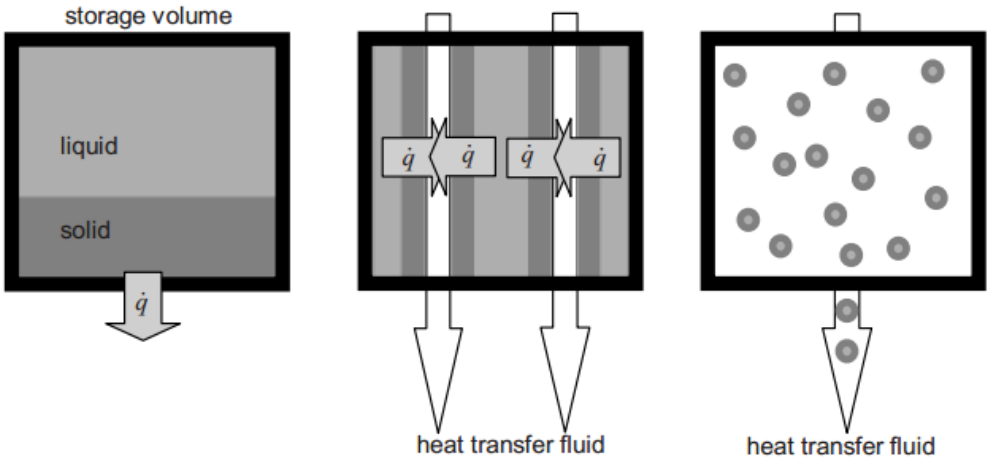

Figure 2-9 Three types of phase change material storage design (Mehling *et al.* 2008)

The first design is usually applied when the application does not have enough space for forced convection or the magnitude of melting/solidification power is not the first priority. For example, when PCM is installed in a narrow space of the building such as an inner layer of the wall, the goal is to provide free cooling during the peak period. In such case, the dominating effect is conduction through the wall or natural convection at the surface. The drawback of the first design is that the heat transfer coefficient is low and the total area of heat transfer is not sufficient. The second design uses the internal area within PCM to increase the heat transfer area. Meanwhile, if the heat transfer fluid in the channel is driven by pump or fan, the heat transfer coefficient is also higher when compared to the first design. Moreover, with heat transfer surface extension technologies such as fins, it is possible to achieve an even higher heat transfer area. The third design takes another perspective where the PCM is used both as the heat storage medium and the heat transfer fluid. For example, when PCM is prepared in the

form of slurry, the heat transfer process includes both the transport of the PCM and the heat transfer on the surface of the material. In the building PCM application, the first and second type of design are mostly used. Based on whether there is a mixing/movement of PCM material, TES could be categorized as dynamic or static. TES is also defined as active or passive based on the presence of forced convection. First type of design is static and passive. It is usually realized by embedding PCM into the building structure. For example, according to Sharma *et al.* (2009), PCM could be incorporated into the solar house to provide heating to the rooms via the following ways: in Trombe wall, in the wallboards, in the shutters, under the floor and in the ceiling boards. For example, Schossig *et al.* (2005) used micro-encapsulate PCM to replace the wallboard of a full-size room, as shown in Figure 2-10. During the day time, the PCM was melt by the solar radiation. In the night time, PCM released heat and warmed up the room through conduction and natural convection. Since there was no forced convection involved, this type of system was a passive TES application. To provide cooling, PCM needs to be incorporated with a cooling source. One idea is to use the night time air to solidify the PCM. For example, Stritih and Butala (2010) used a ceiling board embedded with PCM. The system is shown in Figure 2-11. The outside air was introduced through the window or by the fan during the night time. During the daytime, PCM was melt to provide free cooling to the rooms. Parameshwaran *et al.* (2012) concluded that in average the passive system could reduce 10% to 15% of the cooling/heating load and could maintain the room temperature in a comfortable level. However, the problem of using the first type of design in building application is that the performance depends on the weather condition such as the day time solar radiation

or the night time ambient air temperature (Zhai *et al.* 2013). Since it is passive, it could not actively reduce the peak period energy consumption. An active system, where an air conditioning system is integrated with PCM, could store the off-peak cooling/heating capability to reduce the overall electricity cost (Sharma *et al.* 2009). An active PCM based TES provides a higher operation flexibility and also a higher energy saving from 45% to 50% (Parameshwaran *et al.* 2012). An active building PCM solution relies on both the building air conditioning systems and the TES. It is also worthwhile to mention that the second design type is more suitable for active systems where the heat transfer fluid is driven to melt or solidify the PCM. Researchers have investigated the potential of using PCM with different HVAC systems in the buildings, as shown in Table 2-5. The key of integrating PCM based TES is to find the proper medium that connects the TES to the building air conditioning system. So far, the most widely used medium is water. Therefore, it is easier to implement such concept in chiller based cooling systems where the chilled water is used to gnerate supply air that cools down the room. As discussed by Al-Abidi *et al.* (2012), integrating PCM based TES into chilled water circuit has become more attractive in last two decades. For example, Parameshwaran *et al.* (2010) proposed and investigated the energy saving potential of incorporating PCM with a chiller-VAV system. In their study, two chillers provided chilled water to both the VAV terminals and the PCM tank. By solidifying the PCM during the off-peak period, the excessive cooling capability was stored. During peak period, PCM worked together with the chiller system to support the cooling coils in the VAV system. They found that the new system could achieve 28% and 47% of energy saving when compared to conventional chiller based system. Fang *et al.* (2010)

also investigated the potential of using PCM in a chiller based cooling system. The system had one chiller which provided chilled water to both the fan coil unit and the PCM based TES. The PCM based TES was in the form of spherical capsules. It was found that the new system had a stable discharging and charging process. COP during the latent heating releasing period was higher than 2.1, which was better than the conventional air-cooled ice storage system.

It is also possible to integrate PCM based TES in systems other than the chiller based systems. For example, Gu *et al.* (2004) proposed a PCM based TES system by utilizing heat recovery concept. The system had both PCM based TES and condenser in the high-pressure side. The discharged vapor from the compressor released heat in both the PCM based TES and condenser. The goal was to recover part of the condensing heat by melting the PCM. The heat stored in PCM was later used to provide hot water to the users. The system showed a stable discharging and charging process and the integrated energy efficiency ratio (IEER) reached 7.6 when the condensing temperature was 55°C. Hamada *et al.* (2007) used a snow-ice system with ground source heat pump to provide cool air to the rooms through natural convection for a building in a snowy area. The same system could also reduce the snow accumulations and enhance the snow-disposal process. Qi *et al.* (2008) investigated a solar assisted heat pump system where the solar radiation was used to generate warm water that could be used in the evaporator side of the heat pump. The air conditioning system thereby absorbed heat from the evaporator and provided heating to the room through heat pump operation. The PCM based TES was installed on the solar energy loop. The system was compared to a central solar heating system with hot water storage. It was found that the temperature of PCM could

be lower than the baseline and therefore the efficiency of the solar collector could be higher. During the heating season, the COP of the system was about 4.2. Long and Zhu (2008) combined PCM based TES with air source heat pump water heater. In the off-peak period, the refrigerant from the compressor melt the PCM in the condenser. During the peak period, the tap water could be heated up to 50°C. The average COP was found to be higher than 3.08. Benli (2011) used a PCM based TES to provide heating to a house located in Turkey. Benli's study used PCM based TES in parallel to GSHP. Therefore, the excessive heat provided by GSHP was stored in TES which was located on the air side. A fan circuit was built to facilitate the heat releasing from the PCM to the rooms. The system was tested under low ambient temperature between -5°C to -20°C. It was found that the COP of the whole system was from 2 to 3.5. Diaconu (2012) investigated a solar-assisted ejector air conditioning system with PCM based TES. Solar radiation was used to generate high-pressure fluid in the generator. PCM based TES was installed on the evaporator side as cooling energy storage device. The ejector air conditioning system provided cooling to the room through an air handling unit.

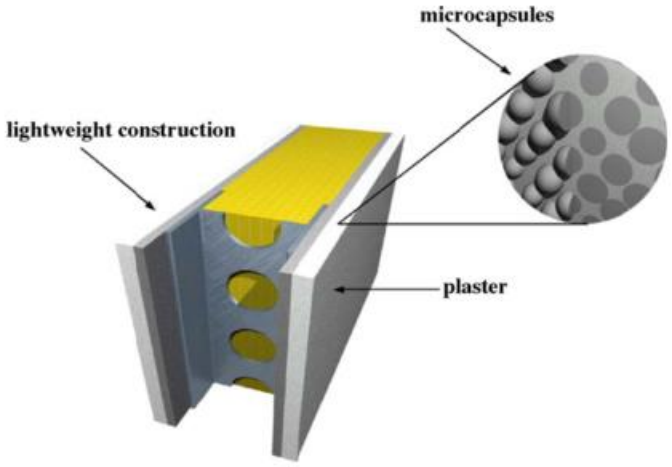

Figure 2-10 PCM integrated into wall: space heating (Schossig *et al.* 2005)

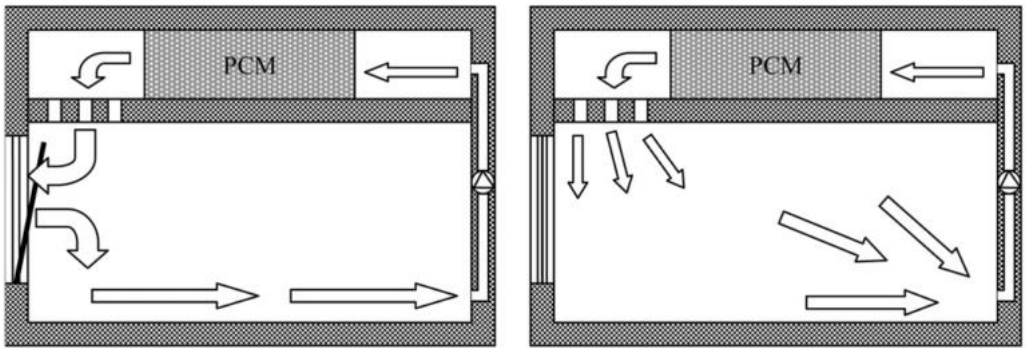

Figure 2-11 PCM integrated into ceiling: space cooling (Stritih and Butala 2010)

Table 2-5 PCM in building HVAC

Authors (Year)	Air Conditioning System	Operation Mode	Benefit
Gu *et al.* (2004)	N/A	Cooling, Water Heating	PCM recovers heat to generate hot water
Hamada *et al.* (2006)	Ground source heat pump	Cooling	Energy saving; Uses snow-ice as storage;
Qi *et al.* (2008)	Solar assisted heat pump	Heating	Smaller solar collector size
Long and Zhu (2008)	Air source heat pump water heater	Water Heating	Refrigerant heats up the PCM; COP improvement
Fang *et al.* (2010)	Chiller system, Fan Coil Unit	Cooling	Seasonal energy consumption reduction; Peak load reduction
Parameshwaran *et al.* (2010)	Combined VAV-Chilled Water System	Cooling	COP improvement; Seasonal energy consumption reduction
Benli (2011)	Ground source heat pump	Heating	COP improvement; Peak load shift
Diaconu (2012)	Ejector System	Cooling	Solar-powered ejector cooling

2.4.2.1 Demand Response and Energy Efficiency

As can be found from Table 2-5, these studies mainly focused on the energy saving potential of the system. Therefore, the key aspects researchers investigated were EE goals such COP improvement and the seasonal energy saving. However, one of benefits of these active systems, as pointed by Yau and Rismanchi (2012), is the balance of energy demand between peak and off-peak hours for both the grid and the end-users.

Yau and Rismanchi also found that the selection and operation of TES should consider peak/off-peak performance of the system as well as localized parameters such as climate profile and energy policy. As pointed out by Palensky and Dietrich (2011), the conventional energy systems operate in unidirectional and top-down mode that a series of power plants feed into the grid and try to control the balance in the grid at any time. In this sense, a higher EE leads to a lower overall electric demand from the user side, which facilitates the operation of the grid. However, the challenge is that the overall electricity consumption increases every year despite the improvement of EE, which adds up the complexity of the grid control. Moreover, with the introduction of renewable energy and distributed local energy generation, the controlling the balance of the grid becomes more challenging. The concept of DR is proposed due to fact that the conventional unidirectional EE-driven design is no longer sufficient. One of the advantages of DR is that the focus is now on the demand side, which is less expensive to be manipulated or influenced. The key of DR is to shape or curtail the load profile in the user side by economic incentives. However, it should be pointed out that the DR concept does not necessarily reduce the overall energy consumption. For example, Arteconi *et al.* (2013) investigated the DR potential of an air-to-water heat pump system coupled with hot water storage. It was found that storage was necessary in maintaining a stable room temperature in the heating season. However, when compared to baseline heat pump systems without TES, there was no significant reduction in the energy consumption. This could also be illustrated in Figure 2-12. With energy efficient operation, the overall energy consumption is reduced. With DR operation, the energy consumption during the DR event is reduced. However, it is possible that the energy

consumption of the hours following the event catches up and is even higher, which is called the "rebound" effect. Therefore, it is critical to consider both the EE and DR.

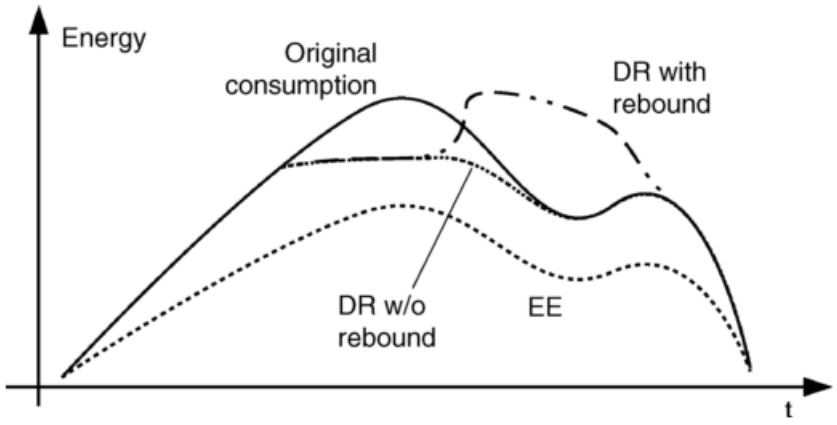

Figure 2-12 Energy efficiency and demand response (Palensky and Dietrich 2011)

The coordination of DR and EE is also called demand side management (Lee *et al.* 2016). As reported by Goldman *et al.* (2010), the combination of EE and DR is predicted to be able to reduce US summer peak load by 14% to 20% by 2020.

Meanwhile, a key feature of using PCM based TES in building air conditioning systems is to store the cooling/heating energy in the off-peak period and reduce the air conditioning system energy consumption in the peak period, which makes such systems an ideal playground to realize both EE and DR operation. However, Arteconi *et al.* (2012; 2013) found the potential of integration of heat pump systems and PCM based TES was still less discussed.

2.5 Research Gaps and Objectives

Based on the literature review, it is clear that the following research gaps have not been covered by the existing studies.

In the experimental study part, the performance of HRVRF is limited to lab testing. The field performance of novel VRF systems is even more limited, especially the MFVRF which could provide cooling, heating and water heating. The effects of HR operation and water heating operation on the performance enhancement of the MFVRF system are not discussed. In the simulation part, the validation work of dynamic VRF models is still limited and the uncertainty in capacity and energy consumption is still higher than expected. Moreover, since these VRF models are based on mapping method, it is also difficult to evaluate new system configurations or new control strategies based on these models. In the TES part, it can be seen that the existing studies of integrating of PCM based TES and building air conditioning system mainly focused on chiller systems and heat pump systems. However, none of existing studies considered the integrating of VRF systems and PCM based TES. Moreover, the existing studies focused on either cooling or heating. Since the VRF system is designed to operation in both cooling and heating season, it is necessary to consider using an integrated VRF system with single PCM based TES to cover both cooling and heating operation. Moreover, one key aspect missing in the investigation of the current air conditioning systems integrated with TES is the DR capability of the system. As found through the literature review, both EE and DR aspect should be considered.

Therefore, this dissertation defines the following research objectives to fill the research gaps:

- Carry out field tests of a MFVRF system to investigate and quantify the effect of heat recovery operation and water heating operation

- Simulate the MFVRF and analyze the source of deviation in dynamic VRF models
- Create a new dynamic VRF model with higher accuracy and evaluate the effect of energy saving operation and new VRF systems. The model should be able to estimate the energy consumption of the VRF system with an hourly deviation less than 10%
- Propose and evaluate a new VRF system integrated with single PCM based TES that could support both cooling and heating operation
- Investigate both EE and DR potential of the new VRF system and carry out economic analysis

3 Experimental Evaluation of Multi-Functional Variable Refrigerant Flow System

3.1 Experiment Setup

3.1.1 Test Facility

The MFVRF system in this study consisted of one OU, two HRUs, seven IUs, and one water heating system. The OU was connected to the HRU by three refrigerant pipes: a high-pressure gas pipe, a liquid pipe and a low-pressure gas pipe. The HRU could alter the direction of the refrigerant flow entering the indoor HXs during the mode switch and redistribute the mass flow of refrigerant among three pipes. The IUs were all connected to the HRUs. Because one HRU can only support up to four IUs, two HRUs were used in this study. The IUs were wall-mounted IUs consisting of a finned-tube HX, EEV and fan. There were three different types of IUs. The nominal cooling capacity of each type is 2.2, 3.6, and 5.6 kW, respectively. The water heating system included a plate HX, EEV, pump and water storage tank of 291 L. In the plate HX, the high temperature gas refrigerant generated hot water, which would be driven by the pump to heat up the water storage tank through cooper tubes. The nominal water heating capacity of the system was 15.9 kW. In the outdoor side, there were two fans on the top of the OU to drive the air across the two finned-tube refrigerant to air HXs as the system was an air sourced VRF system. Both of two OU HXs were connected to the inverter driven variable speed compressor via four-way valves. Finally, the compressor was capable of operating within a frequency range from 0 Hz to 90 Hz. When the system was in cooling mode, the OU could provide the IUs a total rated

cooling capacity of 35.2 kW. In the heating mode, the rated heating capacity of the OU was 39.6 kW. The nominal capacities of the system are shown in Table 3-1, including OU, IUs and water heating system.

Table 3-1 System nominal capacities

Component	Cooling Capacity [kW]	Heating Capacity [kW]
Outdoor Unit	28.1	31.6
Indoor Unit #1,#6,#7	2.2	2.5
Indoor Unit #2,#3	3.6	4.0
Indoor Unit #4,#5	5.6	6.3
Water heating system	14.1	15.9

The refrigerant flow diagram of the installed MFVRF system in the heating-main mode is shown in Figure 3-1. In Figure 3-1, five IUs and the water heating system were in heating mode, and only two IUs were in cooling mode. For example, in Figure 3-1, discharged refrigerant was cooled down in the water heating system and heating IUs. It was then sent back to the liquid pipe of the heat recover unit where part of the subcooled liquid would be sent to the cooling IUs. The rest of refrigerant would be sent to the outdoor HXs. This part of refrigerant would expand in the EEVs and absorb heat from the outdoor air. Finally, the superheated gas, either from IUs or OUs, merged at the suction line of the compressor.

In this MFVRF system, the water in the plate HX was firstly heated by the refrigerant in the plate HX. This part of high temperature water would heat the water in the tank

through copper tubes. In other words, the water tank was heated up indirectly. Finally, in the field testing, there was no actual water demand from the users. Therefore, an actuator was used to drain the hot water to the sewage according to the hot water demand to simulate the water consumption of the buildings.

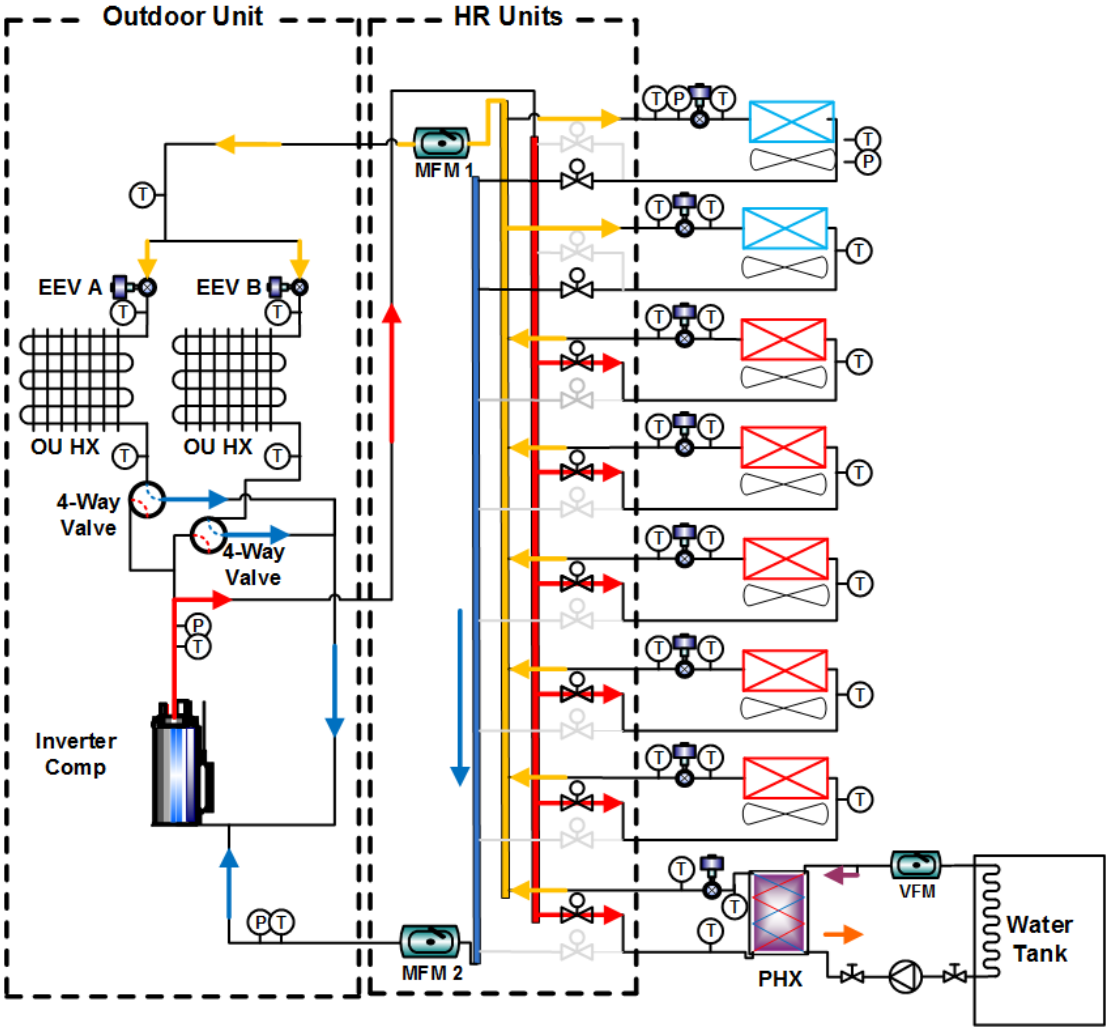

Figure 3-1 Schematic Diagram of MFVRF system

3.1.2 Measurement

Figure 3-1 also shows the sensor locations of the MFVRF system. The refrigerant-side temperature of the system was measured by T-type thermocouples installed on the surface of the refrigerant pipes. The inlet air-side temperature of the OU was measured by eight T-type thermocouples installed close to the HXs. The outlet air–side temperature of the OU was measured by the thermocouples installed close to the OU fan. The humidity of the air was measured by relative humidity (RH) sensors. In order to avoid the effect of radiation or rain, the exposed thermocouples and RH sensors were all shielded. The inlet air temperature and RH of the IU were measured by a T-type thermocouple and a RH sensor respectively that were installed at the inlet of the IU. Similarly, the temperature and RH of the air leaving the indoor HX were measured by a thermocouple and a RH sensor respectively installed at the outlet port. The water temperature of water heating system was measured by in-stream thermocouples. The water temperature within the tank was measured by six vertically inserted thermocouple probes.

The pressures of the system were measured by both the built-in sensors in the compressor and two pressure sensors at the IUs. The built-in sensors in the compressor measured the suction and discharging pressures. The pressure sensors at the IUs measured the pressure before the EEV and after the indoor HX.

As shown in Figure 3-1, the mass flow rates entering the HRUs were measured by two Coriolis mass flow meters located in the liquid line and the low pressure gas line. The mass flow rates of the IUs and water heating system were calculated by the correlation

equation of the EEV. The water flow rate of the plate HX in the water heating system was measured by the turbine flow meter installed in the main water loop.

The energy consumptions of the systems were measured by two watt meters: one watt meter for OU, and another watt meter for the rest of the system. The watt meter for the OU measured the energy consumption of the compressor and the fans of the outdoor HXs. The watt meter for the IUs measured the energy consumption of the all indoors units, water heating system, HRUs, and other parts of the VRF system. The specifications of instrument are listed in Table 3-2.

Table 3-2 Specifications of instrument

Measurement	Range	Accuracy
T-type Thermocouples	-200~350°C	±0.5K
Pressure Transducer (High pressure side)	0~6,770 kPa	±6.34kPa
Pressure Transducer (Low pressure Side)	0~3,339 kPa	±4.21kPa
Coriolis Flow Meter (Liquid line)	3~457.5 g/s	±0.2% FS
Coriolis Flow Meter (Gas line)	0~450 g/s	±0.2% FS
Wattmeter (Indoor units)	0~4 kW	±0.2% FS
Wattmeter (Outdoor Unit)	0~40 kW	±0.5% FS
RH Sensor	0~100%	3%

3.1.3 Test Conditions

The MFVRF system was installed in a building in College Park, Maryland. The types of tests involved in this study are listed in Table 3-3 and Table 3-4. In the cooling season tests, there was no space heating demand. Therefore, only water heating would be considered in the cooling season tests. In the heating season tests, there was space cooling demand from the rooms where IU#4, IU#5 and IU#7 were installed. Therefore, both the HR testing and hot water demand testing would be possible. Since the system was sized based on the cooling load, the rated heating capacity was actually oversized when compared to the heating load of the buildings in the heating and shoulder season. The hot water consumption considered in this study was obtained from the ASHRAE handbook (ASHRAE 2011). The set point for the water tank was 50°C. The room set temperature for the heating mode was 20°C, and that for the cooling units was 27°C. The cooling season tests were carried out before the heating season tests. In the cooling season tests, it was found that tests based a daily hot water consumption of 980 L had similar results as tests based on 738 L of hot water. Therefore, in the heating season, the hot water consumption was increased to 1230 L during the water heating tests.

Table 3-3 Cooling main test

Test mode	Cooling Units	Daily Hot Water Generation: L/day
Cooling Main Case 1	IU #1 #2 #3 #4 #5 #6 #7	0
Cooling Main Case 2	IU #1 #2 #3 #4 #5 #6 #7	738
Cooling Main Case 3	IU #1 #2 #3 #4 #5 #6 #7	980

Table 3-4 Heating main test

Test mode	Cooling Units	Heating Units	Daily Hot Water Generation: L/day
Heating Main Case 1	IU #7	IU #1 #2 #3 #4 #5 #6	0
Heating Main Case 2	IU #7	IU #1 #2 #3 #4 #5 #6	738
Heating Main Case 3	IU #7	IU #1 #2 #3 #4 #5 #6	1230
Heating Main Case 4	IU #4 #5	IU #1 #2 #3 #6 #7	0
Heating Main Case 5	None	IU #1 #2 #3 #4 #5 #6 #7	0

3.1.4 Data Reduction

The two mass flow meters measured the mass flow rates of the refrigerant as it entered the HRUs. The HRUs then distributed the refrigerant among the components according to the operation mode. The total mass flow rate during the heating main mode could be calculated in Equation 3-1 and Equation 3-2 for the cooling and heating modes.

$$\dot{m}_{total,heating} = \dot{m}_1 + \dot{m}_2 \qquad \text{Equation 3-1}$$

$$\dot{m}_{total,cooling} = \dot{m}_2 \qquad \text{Equation 3-2}$$

In Equation 3-1 and 3-2, $\dot{m}_1$is the mass flow rate measured in the liquid line and $\dot{m}_2$is the mass flow rate measured in the low pressure gas line. $\dot{m}_{total,heating}$ and $\dot{m}_{total,cooling}$ are the total mass flow rates of heating and cooling units, respectively. The total refrigerant flow rate of either cooling or heating needs to be divided to obtain the mass flow rate of each operating unit. The mass flow rate of each unit was calculated by Equation 3-3 and Equation 3-4.

$$R_i = C_d A_i \sqrt{2\Delta P_i \rho_i} \qquad \text{Equation 3-3}$$

$$\dot{m}_i = \frac{R_i}{\sum_1^n R_i} \dot{m}_{total} \qquad \text{Equation 3-4}$$

R_i is the calculated mass flow rate by the EEV correlation equation which consists of the flow efficient (C_d), the area of the EEV (A_i), the pressure drop across the EEV (ΔP_i) and the density at the inlet of the EEV (ρ_i). The individual mass flow rate is calculated by Equation 3-4 where $\dot{m}_{total}$ is the total mass flow rate for either cooling or heating. n is the number of cooling or heating units.

The approach to calculating the individual and total capacity for heating and cooling IUs are shown from Equation 3-5 to Equation 3-7.

$$\bar{Q}_{cooling/heating} = \dot{m}_{\iota}\Delta h \qquad \text{Equation 3-5}$$

$$\bar{Q}_{total,cooling} = \sum_1^n \bar{Q}_{cooling,i} \qquad \text{Equation 3-6}$$

$$\bar{Q}_{total,heating} = \sum_1^n \bar{Q}_{heating,i} \qquad \text{Equation 3-7}$$

$\bar{Q}_{cooling/heating}$ is the space cooling or heating capacity of the IUs. Δh is the enthalpy difference of refrigerants across the IU. $\bar{Q}_{total,cooling}$ and $\bar{Q}_{total,heating}$ are the calculated total space cooling and heating capacity of cooling and heating IUs of the system. The capacity of the water heating system is calculated according to the water side temperature difference rather than the refrigerant side. It is given in Equation 3-8.

$$\bar{Q}_{waterheating} = \dot{m}_w \mathrm{C_p}(T_{w,out} - T_{w,in}) \qquad \text{Equation 3-8}$$

$\bar{Q}_{waterheating}$ is the calculated water heating system capacity. $\dot{m}_w$ and $\mathrm{C_p}$ are the mass flow rate and specific heat of the water, respectively. $T_{w,out}$ and $T_{w,in}$ are the water outlet and inlet temperature of the plate HX, respectively.

The total cooling capacity, heating capacity, and water heating system capacity are used to evaluate the PLR of the system. The PLR is defined in Equation 3-9.

$$PLR = \frac{\bar{Q}_{total,cooling} + \bar{Q}_{total,heating} + \bar{Q}_{waterheating}}{\bar{Q}_{rated,cooling}} \qquad \text{Equation 3-9}$$

$\bar{Q}_{rated,cooling}$ is the rated heating capacity of the OU. The daily performance factor (DPF) and the hourly performance factor (HPF) of the system are evaluated by Equation 3-10 and Equation 3-11, respectively.

$$DPF = \frac{\sum_{n=1}^{n=24}\left(\bar{Q}_{total,cooling,hr} + \bar{Q}_{total,heating,hr} + \bar{Q}_{waterheating,hr}\right)}{\sum_{n=1}^{n=24}\left(\bar{P}_{OU,hr} + \bar{P}_{IU,hr} + \bar{P}_{Pump,hr}\right)} \quad \text{Equation 3-10}$$

$$HPF = \frac{\left(\bar{Q}_{total,cooling,hr} + \bar{Q}_{total,heating,hr} + \bar{Q}_{waterheating,hr}\right)}{\left(\bar{P}_{OU,hr} + \bar{P}_{IU,hr} + \bar{P}_{Pump,hr}\right)} \quad \text{Equation 3-11}$$

In Equation 3-11, hourly energy consumption of the whole system is made up of the hourly energy consumption of the OUs ($\bar{P}_{OU,hr}$), IUs ($\bar{P}_{IU,hr}$), and the pump in the water heating system ($\bar{P}_{pump,hr}$).

To estimate the extent of HR of the system, the daily heat recovery ratio (HRR) of the system during cooling main and heating main operation is defined in Equation 3-12 and Equation 3-13.

$$HRR_{heating} = \frac{\sum_{n=1}^{n=24} \bar{Q}_{total,cooling,hr}}{\sum_{n=1}^{n=24}(\bar{Q}_{total,heating,hr} + \bar{Q}_{waterheating,hr})} \quad \text{Equation 3-12}$$

$$HRR_{cooling} = \frac{\sum_{n=1}^{n=24}(\bar{Q}_{total,heating,hr} + \bar{Q}_{waterheating,hr})}{\sum_{n=1}^{n=24} \bar{Q}_{total,cooling,hr}} \quad \text{Equation 3-13}$$

Therefore, the HRR would be 0 during cooling or heating only mode. It becomes unity when there is balanced space cooling, space heating and water heating operation.

3.2 Results and Discussion

3.2.1 Effect of Water Heating

3.2.1.1 Cooling Main Mode

The effect of water heating system operation in cooling season is shown in Figure 3-2 and Figure 3-3. Figure 3-2 shows the effect of water heating system on the DPF with the outdoor temperature. When compared to cooling only mode, the DPFs in case 2 and case 3 were improved by 18% and 20.4%, respectively. Figure 3-3 shows the energy consumptions of all cases. When the water heating system was operating, the energy consumption of case 2 decreased by 21% when compared to case 1. One factor leading to the energy saving could be explained with HRR as shown in Figure 3-4. In the cooling main mode, the HRR increased to 0.1 by operating the water heating system. Moreover, the condensing pressure of the system also reduced because the condensing capacity was shared by both the water heating system and outdoor HXs. Water temperature was lower than ambient temperature by 5K. This resulted in a lower compressor frequency and pressure ratio, leading to a reduced energy consumption. The pressure ratios of the compressor in case 1 and case 2 are shown in Figure 3-5. It could be found that when compared to case 1, the compressor frequency of case 2 was reduced by 16.5% along with a 13.4% decrease of the pressure ratio.

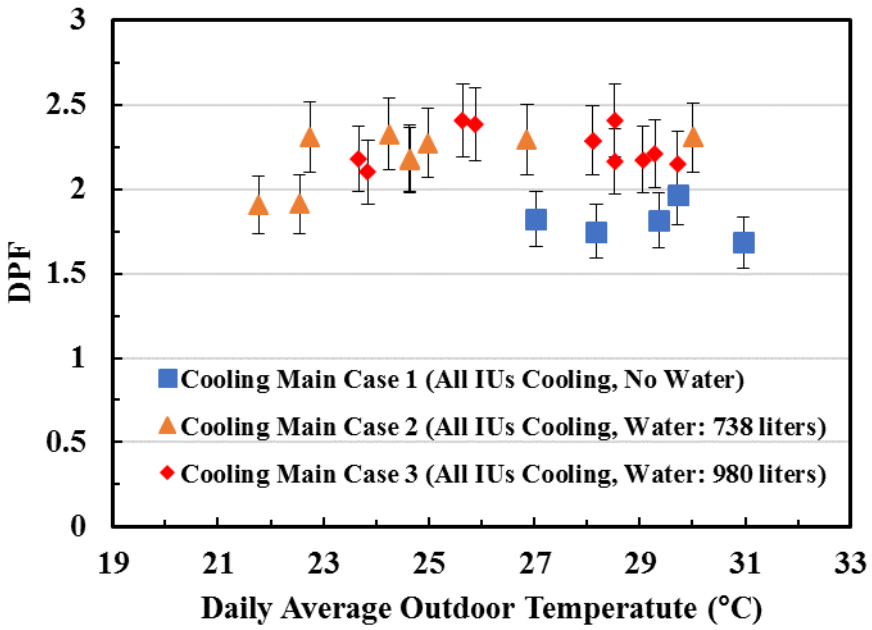

Figure 3-2 Variation of DPF with outdoor temperature

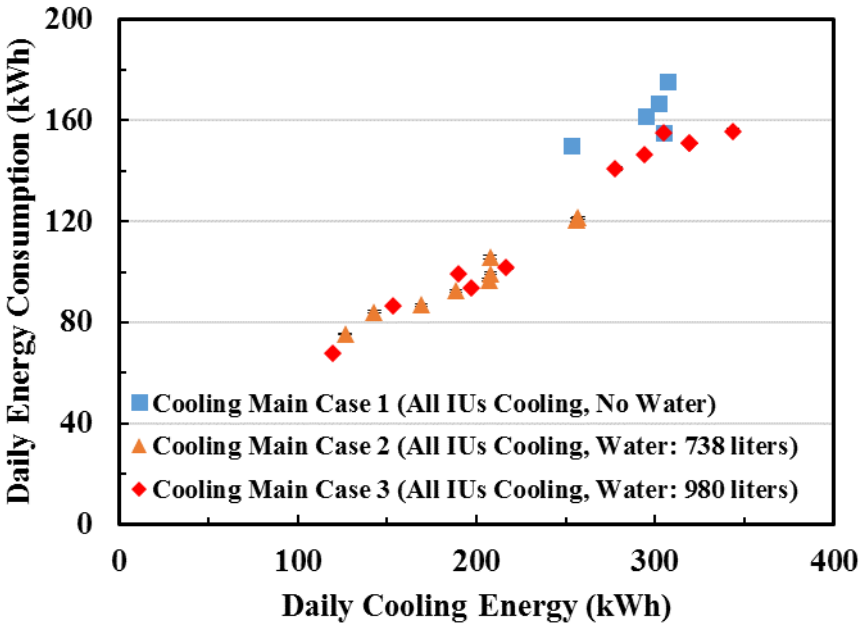

Figure 3-3 Variation of energy consumption with cooling energy

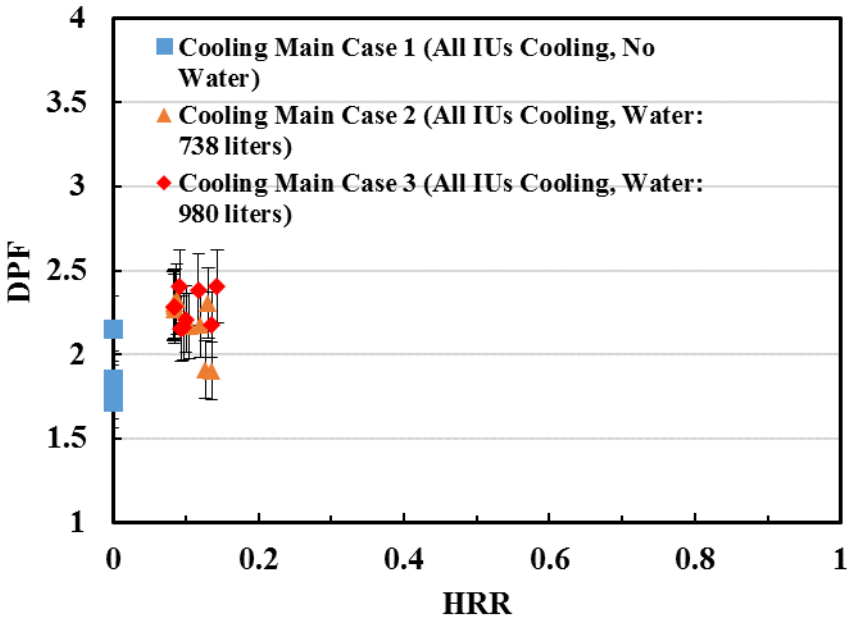

Figure 3-4 Variation of DPF with HRR

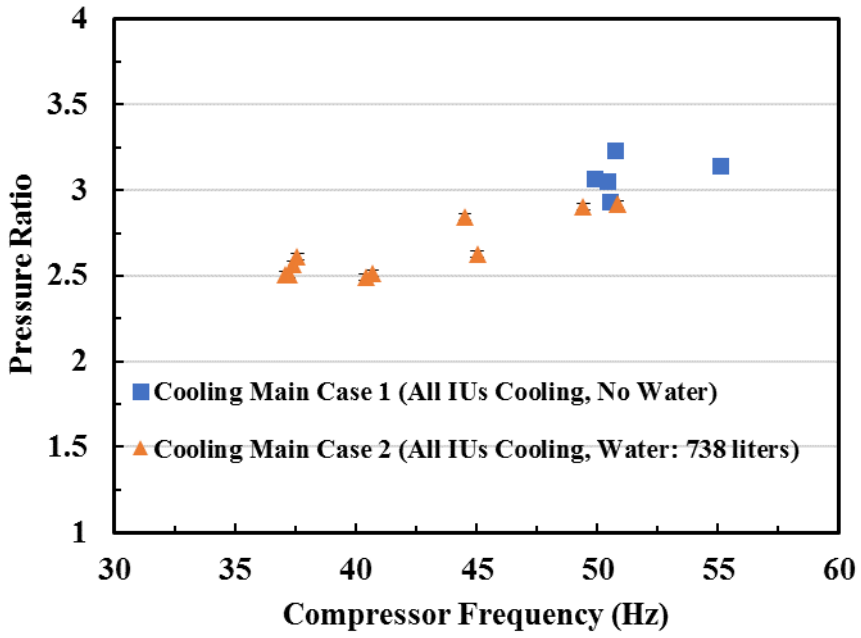

Figure 3-5 Variation of pressure ratio with compressor frequency

3.2.1.2 Heating Main Mode

Five types of tests were carried out in the heating main mode tests. In heating main case 1, the IU #7 was set in cooling mode while the rest of the indoor units were in heating mode. No water consumption was included in case 1. When compared to case 1, case 2 had a hot water demand of 738 L per day. Case 2 and 3 had the same IU setup as case 1. Due to the marginal effect of water heating operation found in cooling season case 3, the hot water demand in heating season case 3 was increased to 1230 L per day. In heating main case 4, IU #4 and IU #5 were set as cooling IUs while the rest of IUs were in heating mode. In case 5, all the IUs were in heating mode and the system was in a heating only mode. Case 1, case 2 and case 3 would be compared to see the effect of hot water demand. Case 1, case 4 and case 5 would be used for HR operation.

Figure 3-6 and Figure 3-7 show the effect of the water heating system operation on the system performance by displaying the variation of the PLR and DPF with the ambient temperature in heating main case 1, case 2 and case 3. It can be found from Figure 3-6 that in the case 1, the PLR of the system decreased when the ambient temperature increased from 0°C to 10°C. This was mainly due to the decreased heating demand of the IUs. When the ambient temperature was above 5°C, the PLR of the system was below 0.2, which yielded a low compressor frequency and caused unnecessary cycling loss in the compressor. Accordingly, in Figure 3-7, the DPF of the system decreased from 0 to 15°C.

With the operation of the water heating system, the influence of the decreased indoor capacity was partially offset. Therefore, by introducing water heating system, it was found that in Figure 3-6 and Figure 3-7 the PLR and DPF in both case 2 and case 3

increased. The improvement of PLR by the water heating system actually resulted in a stable compressor performance, as can be found in Figure 3-8. The operation range of the compressor was from 0 Hz to 90 Hz. With an increase of PLR, The average compressor speed was improved from 35 to 46 and 55 Hz, respectively. The standard deviation of the compressor was also reduced, which enhanced the inverter efficiency. Finally, as shown in Figure 3-9, when the hot water demand was set as 738 L, compared to case 1, the average PLR of the MFVRF system was elevated to 0.32. The DPF was improved by 7%. The improvement was less than the cooling main case because of the factor that the system was mainly benefiting from the improved part load operation of the compressor while in the cooling main mode, the water heating system also reduced the pressure ratio across the system. It could also be found that when the water heating demand increased to 1230 L, the system improvement was limited. It was because that the water heating system would require a longer period of higher discharge pressure to heat up the water tank, which would offset the energy saving brought by the water heating system.

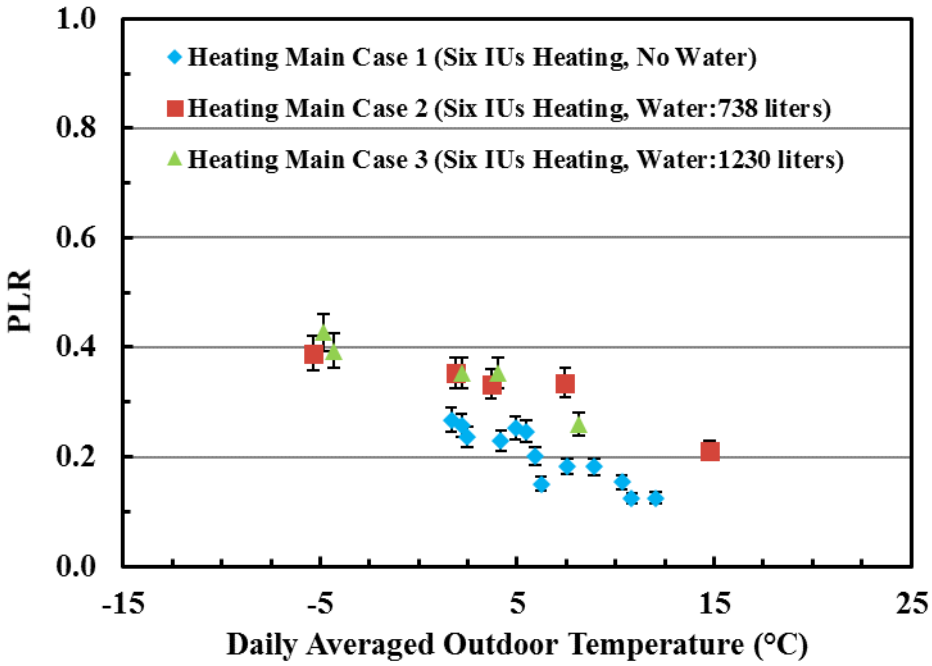

Figure 3-6 Variation of PLR with average outdoor temperature

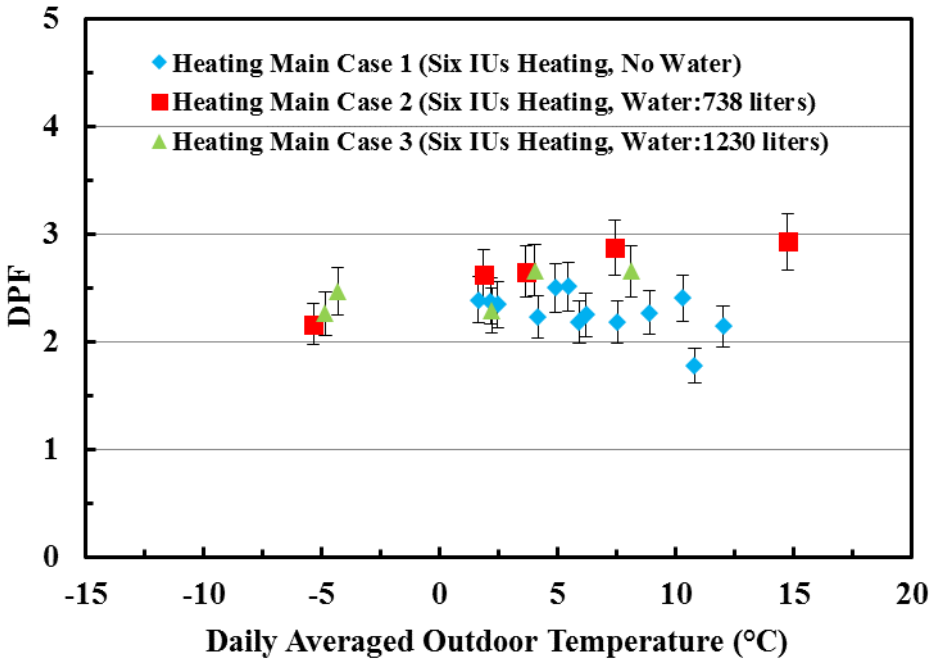

Figure 3-7 Variation of DPF with average outdoor temperature

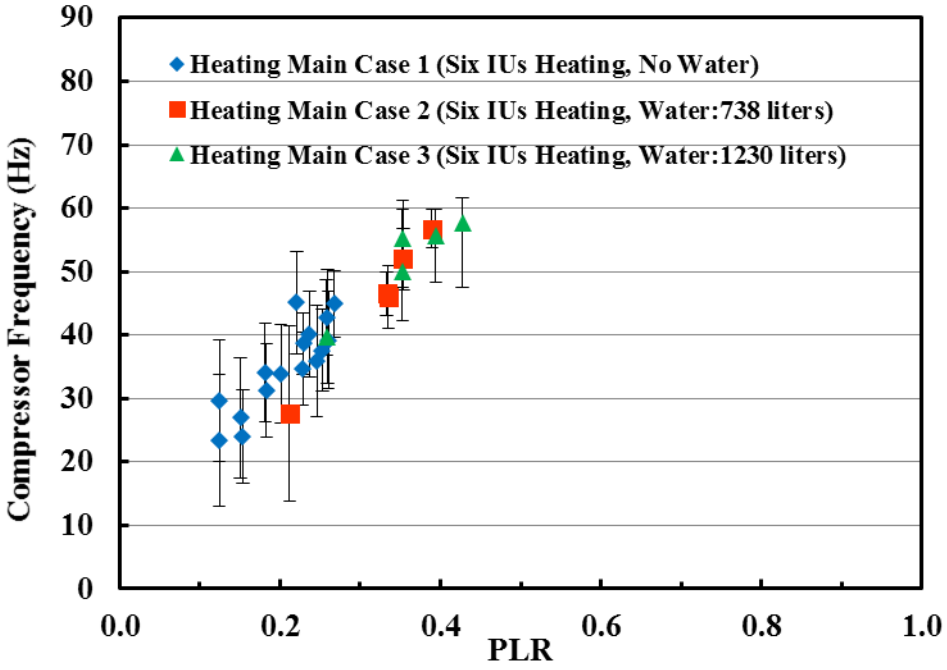

Figure 3-8 Variation of compressor frequency with PLR

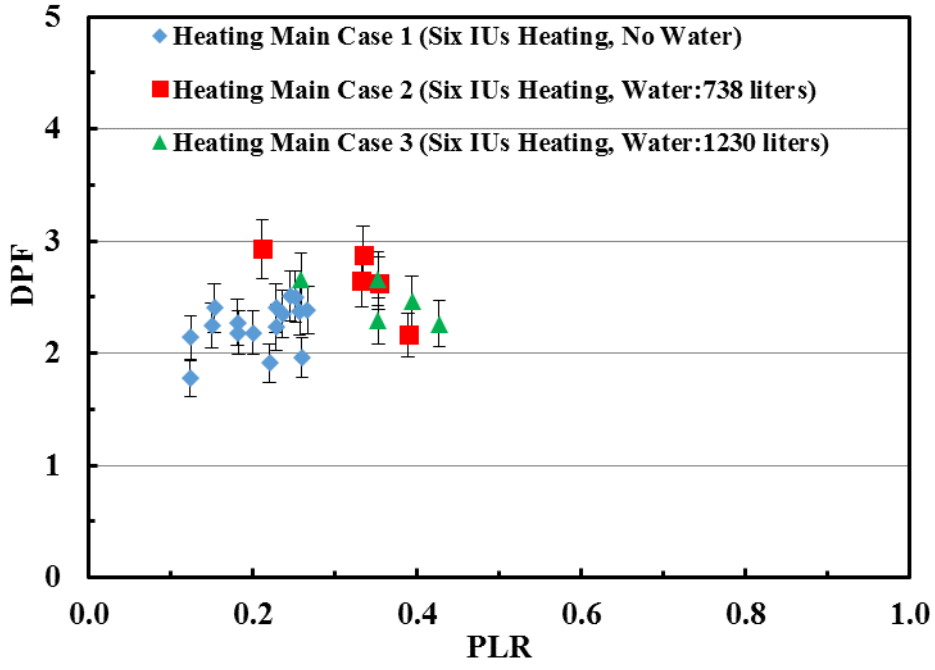

Figure 3-9 Variation of DPF with PLR

3.2.2 Effect of Heat Recovery Operation

The effect of the HR operation is shown in Figure 3-10 and Figure 3-11. When the system operated in the HR operation, its performance reacted very fast as the ambient conditions changed. Therefore, an hourly basis performance analysis was conducted instead of daily basis performance analysis.

Figure 3-10 shows the variation of HPF with the ambient temperature. Figure 3-11 shows the variation of the PLR of the system with the ambient temperature. As shown in Figure 3-10 and Figure 3-11, the performance of the system under the heating only mode was similar to the performance under the heating with only IU#7 in cooling mode. That was because of the low rated nominal cooling capacity of IU#7. When IU#4 and IU#5 were in the cooling mode, the PLR of the system increased from 0.3 to 0.45, and the HPF increased by 17%. One reason was the higher rated nominal cooling capacity of IU#4 and IU#5 when compared to IU#7. The second reason was that those units in the cooling mode (IU#4 and IU#5) were actually installed in a room with high internal load from electronic equipment and human activities. When all units were set to the heating mode, these two IUs would be in standby mode. However, with the HR operation, these two cooling units would be in cooling mode and contribute to the cooling demand of the building.

When the system operated in the HR mode, some of the IUs were working as evaporators which used to work as condensers in the heating mode. In this HR operation (heating main mode), the refrigerant leaving the heating IUs was distributed by the HRUs before entering the cooling IUs. As compared to the heating only mode, the evaporating capacity of the system was separated into two parts: the first part

contributed by the outdoor HX, and the second part contributed by the IUs in the cooling mode. Since the room temperature was higher than the ambient temperature, the evaporating temperature of the system increased. Therefore, when compared to the heating only mode, the compressor frequency dropped to balance the refrigerant mass flow rate while keeping a constant evaporating pressure, leading to a decreased discharge pressure. The average discharge pressure of the system in the heating main mode dropped by 22.2% when compared to heating only case, leading to a decrease of 22.1% drop of pressure ratio, as can be found in Figure 3-12 and Figure 3-13. Therefore, the energy consumption of the whole system was reduced.

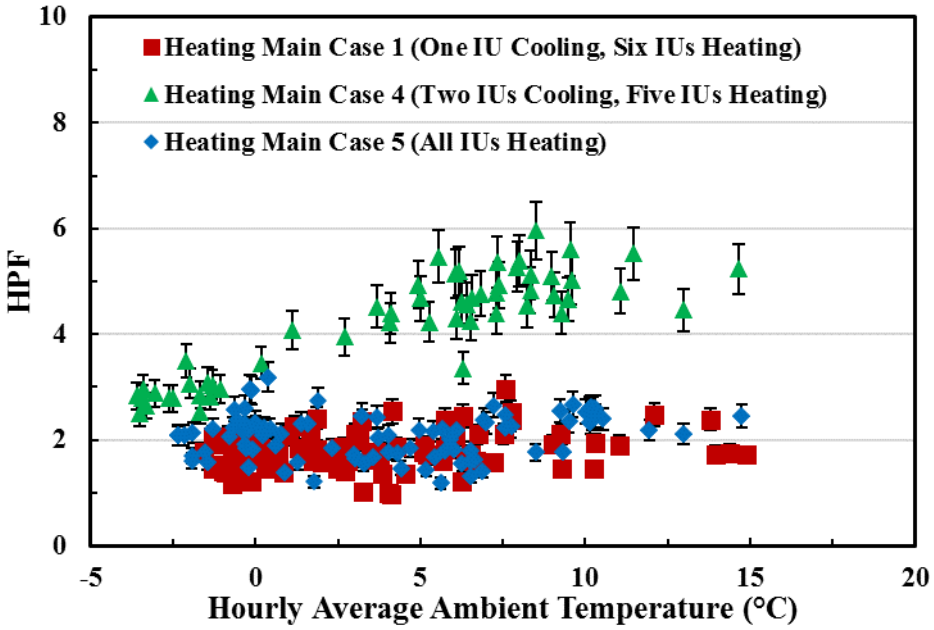

Figure 3-10 Variation of HPF with hourly ambient temperature

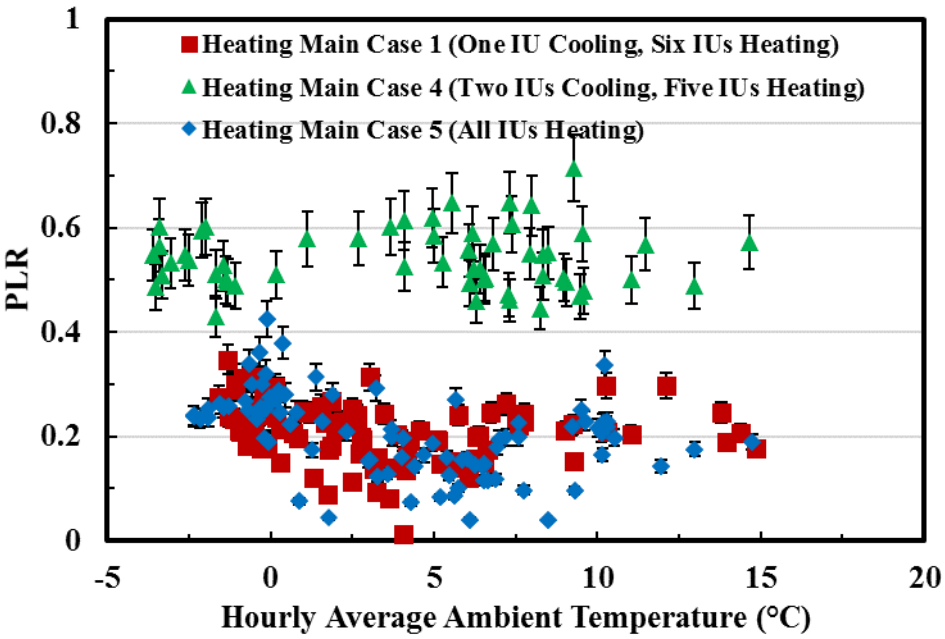

Figure 3-11 Variation of PLR with hourly ambient temperature

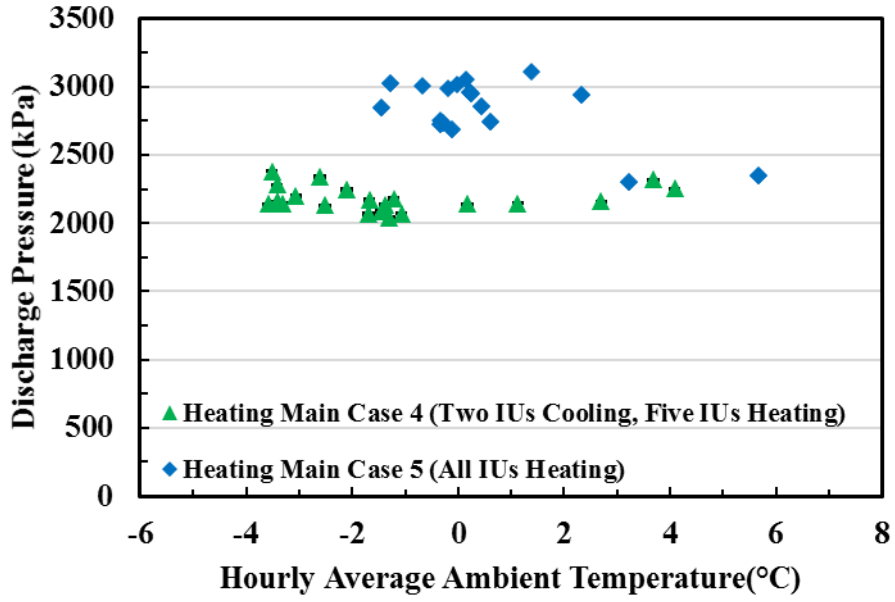

Figure 3-12 Variation of discharge pressure with ambient temperature

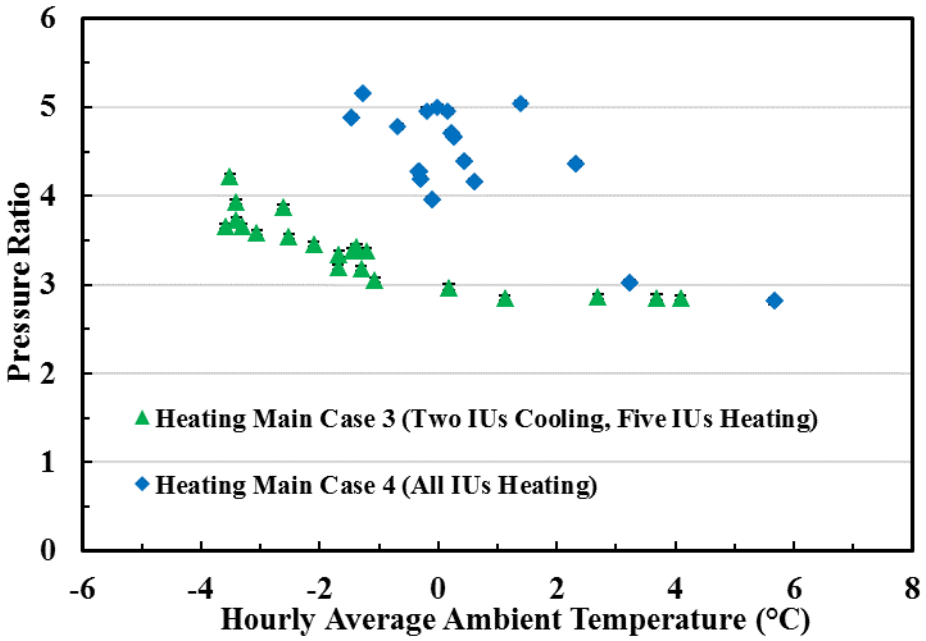

Figure 3-13 Variation of pressure ratio with ambient temperature

4 New Dynamic Modeling of Variable Refrigerant Flow System

4.1 Model Improvement Discussion

Before the development of the new model, it is necessary to discuss the possible model improvement options. As shown in Table 2-3, the hourly deviation of energy consumption and cooling/heating energy reported by previous researches was higher than 15% (15% to 35%). It should also be noted that when the validation was extended to monthly simulation, the deviation was reduced, as found both in previous studies. To improve the accuracy of the model, the following general improvement options should be considered: (a) having accurate performance data during the on/off operation, or more reliable catalogue data; (b) carrying out the validation with a longer period than a week to eliminate the randomness of occupant behavior; (c) creating a detailed building model to include information of thermal walls, solar radiation, and internal gains, while using an accurate local weather data. These improvement options could be concluded into two types: one is to have an accurate estimation of space thermal load; the other is to get an accurate performance map of VRF units. The space load estimation should be the first priority in the model. Therefore, this study firstly focused on the accurate space thermal load estimation before moving to the discussion of the energy consumption calculation of the VRF system. After that, this study analyzed the sources of deviation and discussed the new model.

4.2 Mapping Model Deviation Analysis

The tested MFVRF system was simulated in EnergyPlus 8.0. To simulate such a system, the current EnergyPlus engine needs to be modified to account for both the water heating capability and the heat recovery operation. The flowchart is shown in Figure 4-1. The two key changes made here are the modification of indoor average temperature to include the hot water operation and the heat recovery mode determination. Moreover, to calculate heating capacity of water heating unit (WHU), a WHU model was also created.

4.2.1 Water Heating Unit

The WHU is regarded as a special IU, which always works as a condenser. Therefore, during each simulation time step, the capacity of the WHU is calculated and sent to VRF model to calculate the average heating room side air temperature.

As shown in Equation 4-1, the capacity calculation routine of the WHU is based on regression. The rated capacity $\dot{Q}_{whu,rated}$ is corrected by two factors to obtain the real capacity $\dot{Q}_{whu}$. The first correction factor C_1 calculates the effect of water inlet temperature $T_{whu,in}$ and outdoor air temperature T_{amb}. The second correction factor C_2 takes the water flow rate into consideration.

$$\dot{Q}_{whu} = \dot{Q}_{whu,rated} * C_1 * C_2 \quad \text{Equation 4-1}$$

$$C_1 = a + b * T_{amb} + c * T_{amb}^2 + d * T_{whu,in} + e * T_{whu,in}^2 + f * T_{amb} * T_{whu,in} \quad \text{Equation 4-2}$$

$$C_2 = a + b * ff_{water} + c * ff_{water}^2 \quad \text{Equation 4-3}$$

$$ff_{water} = \frac{Flow_{actual}}{Flow_{rated}} \quad \text{Equation 4-4}$$

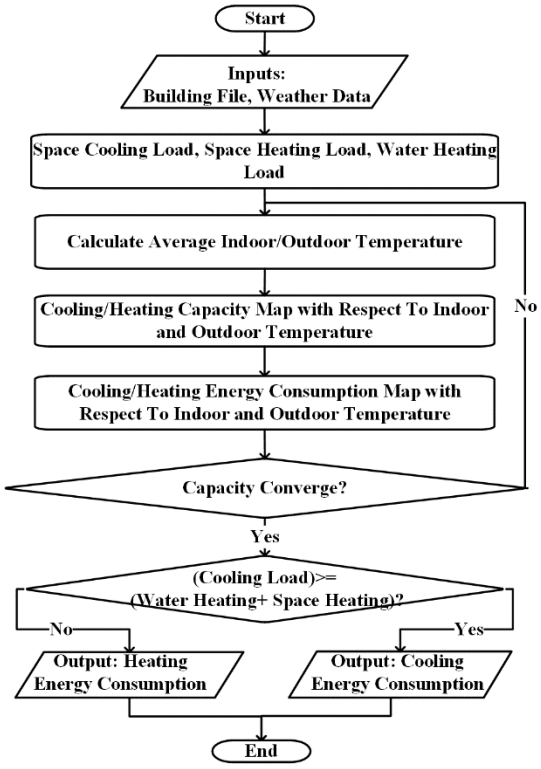

Figure 4-1 MFVRF mapping method model flowchart

4.2.2 Cooling and Heating Season Simulation

The cooling season simulation results were compared to experimental data collected from 2013/07/07 to 2013/07/13. In the heating season validation, the data was chosen from 2014/01/22 to 2014/01/31. In the heating season, the hot water consumption was

chosen as 492 L, which was the hot water demand of two households. The hot water set point was 50°C

The deviation of cooling/heating energy and energy consumption is defined in the following equations by using the hourly averaged data, which are the same as studies covered in Chapter 2. Basically, it is the relative deviation for one hour in percentage.

$$\epsilon_{cap,hr} = \frac{|\bar{Q}_{exp,hr} - \bar{Q}_{sim,hr}|}{\bar{Q}_{exp,hr}} * 100 \qquad \text{Equation 4-5}$$

$$\epsilon_{energy,hr} = \frac{|E_{exp,hr,e} - E_{sim,hr,e}|}{E_{exp,hr,e}} * 100 \qquad \text{Equation 4-6}$$

Similarly, the daily relative deviation is defined as follows, which is based on the accumulated cooling/heating energy or energy consumption in one day.

$$\epsilon_{cap,day} = \frac{|\bar{Q}_{exp,day} - \bar{Q}_{sim,day}|}{\bar{Q}_{exp,day}} * 100 \qquad \text{Equation 4-7}$$

$$\epsilon_{energy,day} = \frac{|E_{exp,day} - E_{sim,day}|}{E_{exp,day}} * 100 \qquad \text{Equation 4-8}$$

Figure 4-2 and Figure 4-3 show the hourly cooling energy and energy consumption validation results. Similarly, Figure 4-4 and Figure 4-5 show the hourly heating energy and energy consumption results. The hourly cooling energy deviation in Figure 4-2 is 20.5%. The hourly energy consumption deviation in cooling mode, shown in Figure 4-3, is 19.5%. These deviation results are within the typical deviation range found in the literature. In heating season, the hourly heating energy deviation in Figure 4-4 is 22.6%. The hourly heating energy consumption deviation in Figure 4-5 is 29.2%. The reason behind the higher deviation in heating season energy consumption is the

oversized heating capacities. It can be found from Figure 4-4 that the hourly heating energy is less than 10 kWh. In this case, the performance map provided by the manufacturers could not provide further information about the cycling of the compressor. If the data is reduced to daily comparison, the cancelling out of the results of opposite signs would lead to a less daily deviation. The daily cooling energy and energy consumption deviation are 9.3% and 5.4%, respectively. The daily heating energy and energy consumption are 8.66% and 18%, respectively. The reduction of the deviations is summarized in Table 4-1.

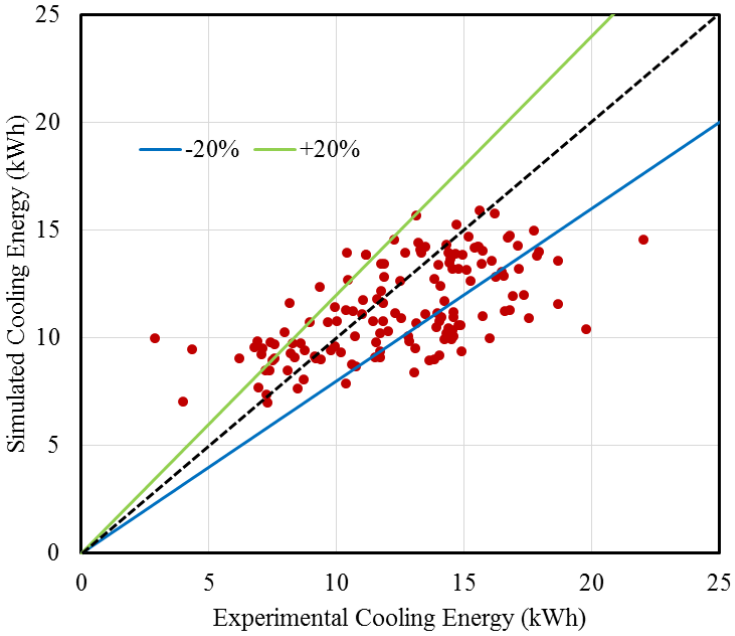

Figure 4-2 Hourly cooling energy validation

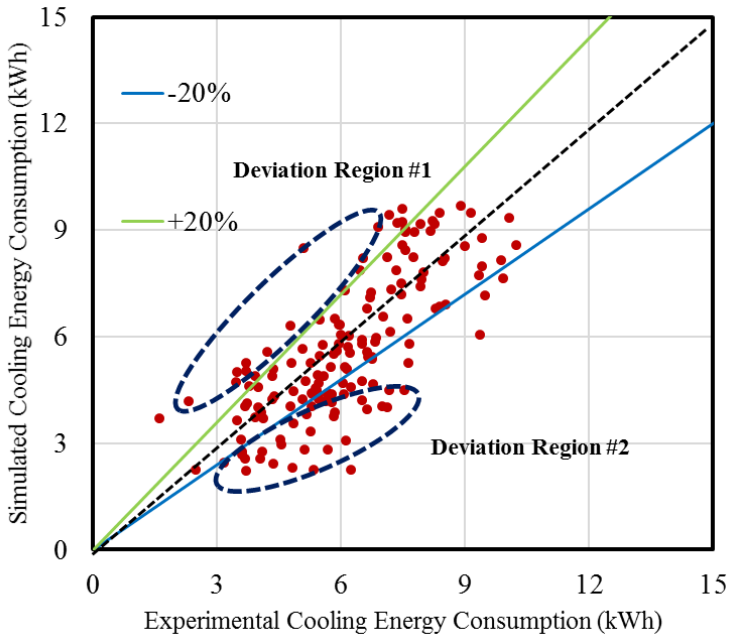

Figure 4-3 Hourly cooling energy consumption validation

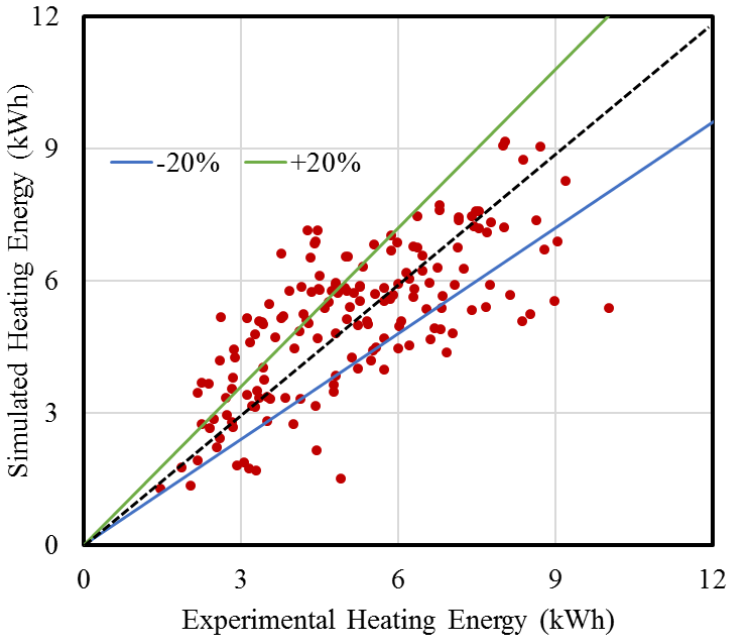

Figure 4-4 Hourly heating energy validation

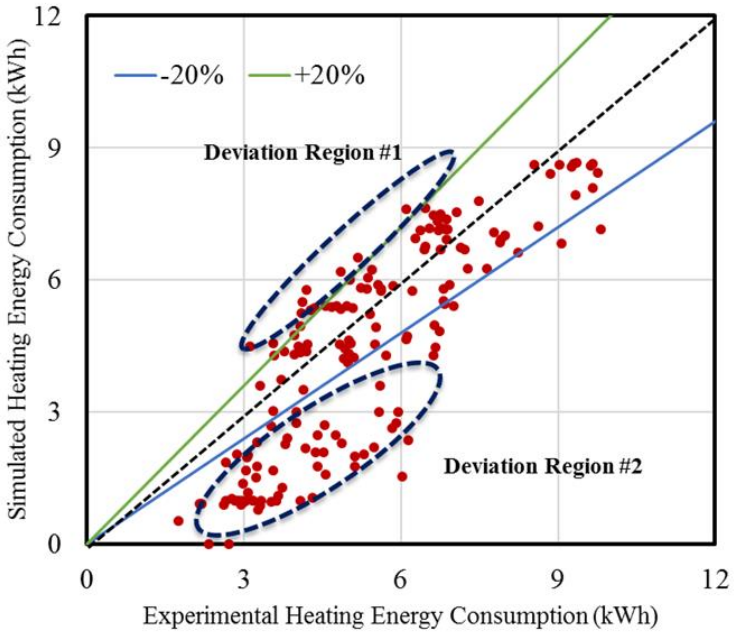

Figure 4-5 Hourly heating energy consumption validation

Table 4-1 Deviation reduction

	Average Hourly Deviation [%]	Average Daily Deviation [%]
Cooling Energy	20.5	9.3
Cooling Energy Consumption	19.5	5.4
Heating Energy	22.6	8.6
Heating Energy Consumption	29.2	18.7

4.2.3 Hourly Data Analysis

The values in Table 4-1 are consistent with the existing studies covered in Table 2-3. However, the existing studies did not further analyze the reasons behind that. Two different regions of deviation: one includes highly underestimated results and another includes high overestimated results can be found from Figure 4-2 to Figure 4-5. To further illustrate the deviation behind the hourly data, two representative hourly cooling data points selected from region #1 and region #2 were taken into further consideration. The simulated results in the region #1 tend to overestimate the performance of the system. The experimental data of compressor frequency in a period of 60 minutes is shown in Figure 4-6. It can be found that the compressor frequency is less than 30Hz for the most time of that period. A frequency of 20 Hz is adopted by manufactures as the on/off cycling threshold. Therefore, in region #1, the performance of the system is fluctuating between low-speed operations and cycling operation. Similarly, the compressor frequency in region #2 is also shown in Figure 4-7. Compared to region #1, the compressor frequency is much higher. In this region, the compressor is fluctuating between a high-speed operation accounting for high room load and a standby operation to maintain the room condition. Based on Figure 4-6 and Figure 4-7, it is therefore clear that the insufficiency of the existing model is the lack of the consideration of the variable speed nature of VRF systems. Performance map could include laboratory tested data under a certain frequency. However, the operation of the system in the real building is much different from the rated map and the conditions in the real application may not be covered by the map, as shown in this study. A carefully calibrated model could probably provide reasonable results in long-term simulation, as

shown in the cooling season results. However, even with such a model, the heating performance could still be problematic. Overall, the accuracy of such a model is not guaranteed.

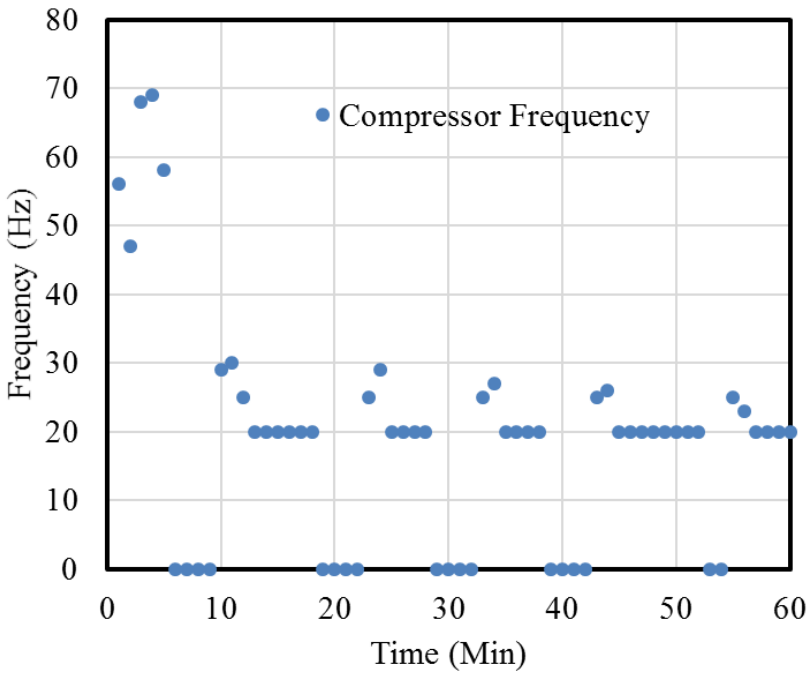

Figure 4-6 Compressor frequency in overestimated region

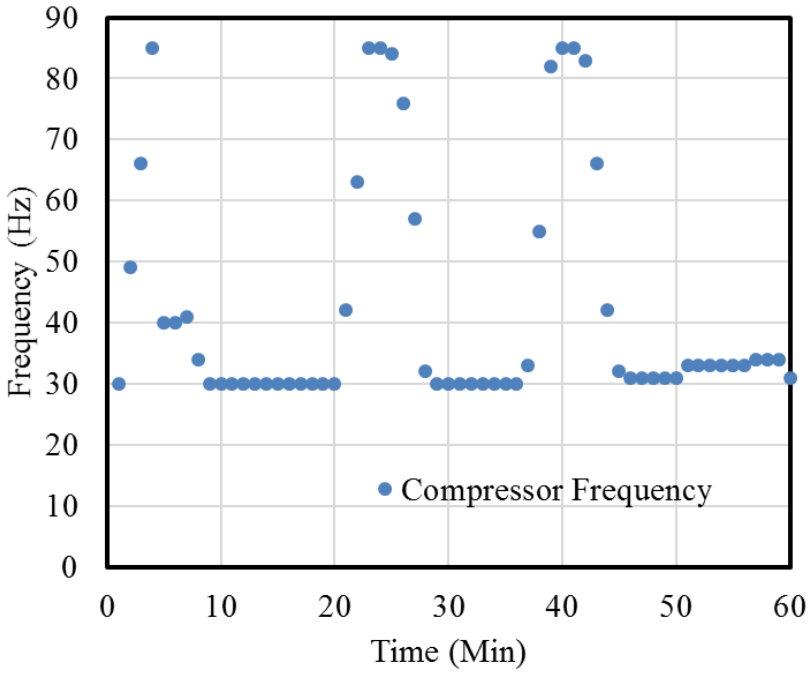

Figure 4-7 Compressor frequency in underestimated region

4.3 New Modeling Approach

Based on the above analysis, the following concepts are included in the new model. First, the building and system layout are improved in the EnergyPlus model. The studies found in open literature highlighted the effect of building thermal walls, solar gain, and internal load on the deviation of the model. However, achieving the accurate solar data or cloud thickness of the location would not be an easy task. Moreover, it would also be difficult to achieve a real internal load profile of the building, even though typical patterns of occupant behavior could be found in ASHRAE standards (ASHRAE 2013). Therefore, in this study, only the effects of building structure and thermal walls are taken into consideration.

Second, in addition to cooling and heating, the MFVRF system is also able to provide hot water. In such cases, the water heating unit (WHU) could be regarded as a special heating unit that requires an increase of discharge refrigerant temperature when in active water heating operation. Therefore, it is necessary to update the WHU model.

Third, a thermodynamic VRF system model is applied to estimate the energy consumption of the system rather than the performance map based model. The current simulation method of VRF systems, which originates from the window AC unit, is a typical regression approach where parameters, such as indoor and outdoor temperatures, are used to generate the performance map (curve-fitting equations) from manufacturer's data. This approach depends on the accuracy of the provided data. The performance map based method is a proper simulation approach for the traditional fixed speed compressor systems. However, the reliability of the data could be problematic when applied to VRF systems because VRF systems are operated under a wide range condition, which the manufacturer's data may not cover. Moreover, the performance of the VRF systems is also affected by certain controllers, which continuously affect the system operation. The thermodynamic model also makes it possible to simulate the control of variable speed compressors in the VRF system.

Lastly, it should also be noticed that part of the reduction of the deviation in the existing studies is due to the increase of the samples in the study. With a higher amount sample, the deviation could be reduced. From the statistical point of view, to quantify the agreement between the experimental data and the simulation results, a more general validation criterion should be used. In this study, the calibration criteria from ASHRAE guideline (ASHRAE 2002) were used to quantify the accuracy of the VRF models

during the hourly validation, where the simulation results are compared against the hourly data collected in validation period of 24 hours. Even though ASHRAE guidelines are recommended for the whole building estimation, it is also a proper guideline for validation of the building VRF systems considered in this study. Two metrics from ASHRAE guideline No.14 were introduced in the validation process: the coefficient of variation of root mean square error (CvRMSE), and the normalized mean bias error (NMBE). The requirements of validation are listed in Table 4-2. The definitions of CvRMSE and NMBE are given in Equation 4-9 and Equation 4-10, respectively.

$$C_v RMSE = 100 * \frac{\sqrt{\sum_{i=1}^{n} \frac{(y_i - \hat{y}_i)^2}{n-1}}}{\bar{y}} \qquad \text{Equation 4-9}$$

$$NMBE = 100 * \frac{\sqrt{\sum_{i=1}^{n} (y_i - \hat{y}_i)}}{(n-1)\bar{y}} \qquad \text{Equation 4-10}$$

Where y_i is the simulation result, $\hat{y}_i$ is the experimental result, n is the amount of testing points, and $\bar{y}$ is the mean of experimental results.

Table 4-2 Validation criteria

Type of Validation	CvRMSE requirement	NMBE requirement
Hourly	≤30%	≤10%
Monthly	≤10%	≤5%

The flowchart of the new VRF model is described in Figure 4-8. The model starts with the implementing of input files which include the building information and weather

data. Based on the inputs, the simulation engine estimates the space cooling, space heating, and water heating load (if exists). Based on the calculated load, the engine calls the thermodynamic model to calculate the required heating and cooling energy consumption. The sum of the cooling load is compared to the sum of the space and water heating load to determine the final system energy consumption. Therefore, the proposed approach can simulate all VRF system options, such as the HPVRF, HRVRF, and MFVRF.

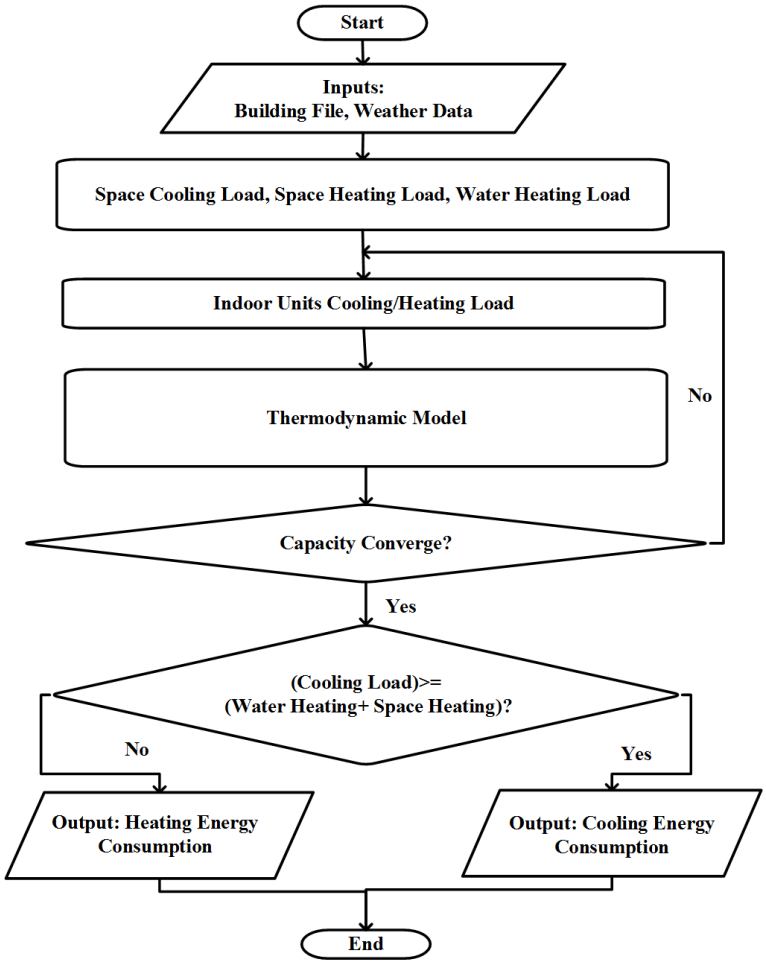

Figure 4-8 New VRF model flowchart

4.3.1 New Thermal Zone Concept

A building model was developed based on the real building layout where the MFVRF system was installed. The floor plan of the third floor is shown in Figure 4-9. The system consisted of seven IUs and one WHU, which was also regarded as a special IU. Seven IUs were installed on the third floor while the WHU was installed on the fourth floor, as shown in Figure 4-9. The HRUs were installed at the plenum above Room C. The OU was also installed on the fourth floor. It should be noted that the rest of building was not served by the MFVRF system. Other spaces and hallways were served by a central cooling and heating system, which maintained the temperature all year round. The dimension and internal load of the rooms are listed in Table 4-3. The specifications of IUs and OU are listed in Table 4-4. Figure 4-10 is the building thermal zone originating from the building layout. In Figure 4-10, the thermal zones excluded from this study are labeled as dummy zones. The hallway thermal zone was defined according to the shape of the thermal zone. The VRF system served Room A to Room E, while the hallway and dummy zones were not controlled. This approach of creating thermal zones, which follows the floor map, is widely adopted for its convenience and simplicity. It is a typical IU-oriented design. This approach applies to most VRF systems, because it allows a flexible arrangement of IU set points. For example, a similar building thermal layout was used in the previous studies by Kwon *et al.* (2012) and Aynur *et al.* (2008). However, this approach, though close to the building floor plan, has several drawbacks.

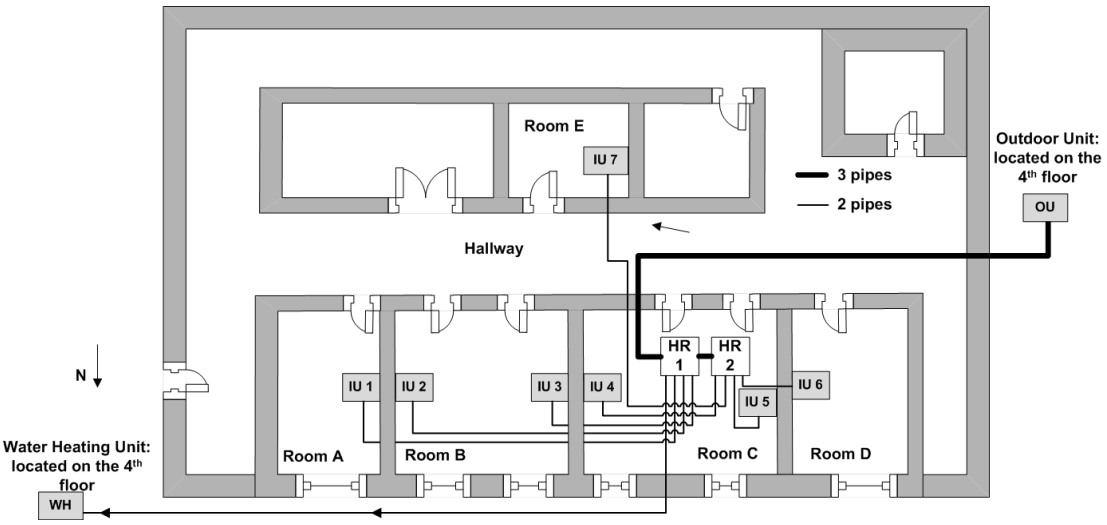

Figure 4-9 Floor plan

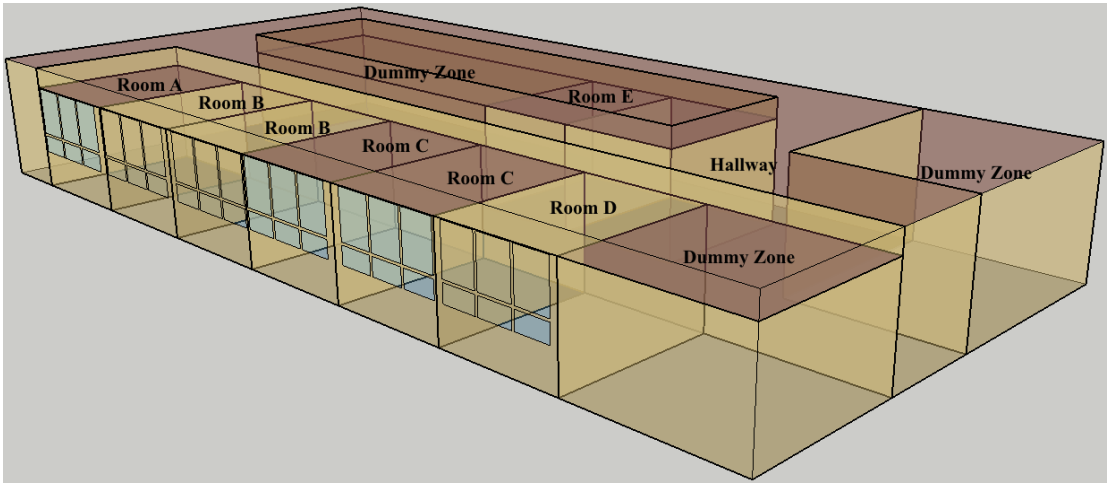

Figure 4-10 Original building thermal zone

Table 4-3 Detailed information of rooms

	Room A	Room B	Room C	Room D	Room E
Space area (m^2)	11.4	22.1	22.4	11.4	9.3
Number of occupants (Person)	1	7	7	1	1
Office Equipment (W/m^2)	30.4	62.1	95.0	34.8	56.8
Lighting (W/m^2)	13.2	13.5	13.4	16.1	13.2

Table 4-4 Cooling and heating capacity of system

Capacity	OU	WHU	IU #1 #6 #7	IU #2 #3	IU #4 #5
Cooling (kW)	28.1	14.1	2.2	3.6	5.6
Heating (kW)	31.6	15.9	2.5	4.0	6.3

The first drawback is the inaccurate thermal boundaries between room B and room C. Thermal zone B and C are divided based on IU installation. However, in this study, by dividing room B and room C into two thermal zones, the model would require a thermal wall inside room B and room C. However, in the actual building, there was no physical wall inside room B or room C. Even though the boundary condition of the imaginary wall could be set as a common surface, which allows the heat transfer between the two adjacent zones, the mass exchange between two zones could not be simulated. In

addition, in EnergyPlus, the default zone air temperature and humidity distribution is assumed uniform in the entire zone. Therefore, by dividing the two zones, even though the set point of each IU could be much more flexible, the thermodynamic assumption of EnergyPlus is violated. Moreover, in this case, since the two IUs were serving the same room, the energy consumption of the IUs would be different from the case where the two IUs were serving two individual zones.

Second, the hallway was set as a non-convex thermal zone for convenience. However, a non-convex zone has difficulties in temperature convergence during each simulation time step if the temperature of the zone needs to be controlled. Therefore, in the layout of Figure 4-10, it is difficult to control the hallway temperature. However, the hallway in Figure 4-9 and Figure 4-10 is actually the most important thermal zones in aspect of surface relationship and inter-zone heat balance. Therefore, with this building layout and thermal wall relationship, the estimation of the load could be problematic. To better reflect the building's thermodynamic condition and thermal wall connection, the following thermal zone distribution was proposed from the view of thermal balance, as shown in Figure 4-11. The dummy zones at the top right corner were removed, because there was no significant heat transfer from Room A to Room E. Meanwhile, the imaginary walls of Room B and Room C were removed to better reflect the uniform psychometric condition in the rooms. Finally, the hallway zones were revised to be made up of only convex zones. These changes made it possible to control the hallway temperature to account for the heat transfer between the hallway and Room A to Room E in the actual building. Meanwhile, since the hallway was also in contact with dummy

zones, the previously uncontrolled dummy zones could be treated similarly as the hallway, which was also more accurate in the building used.

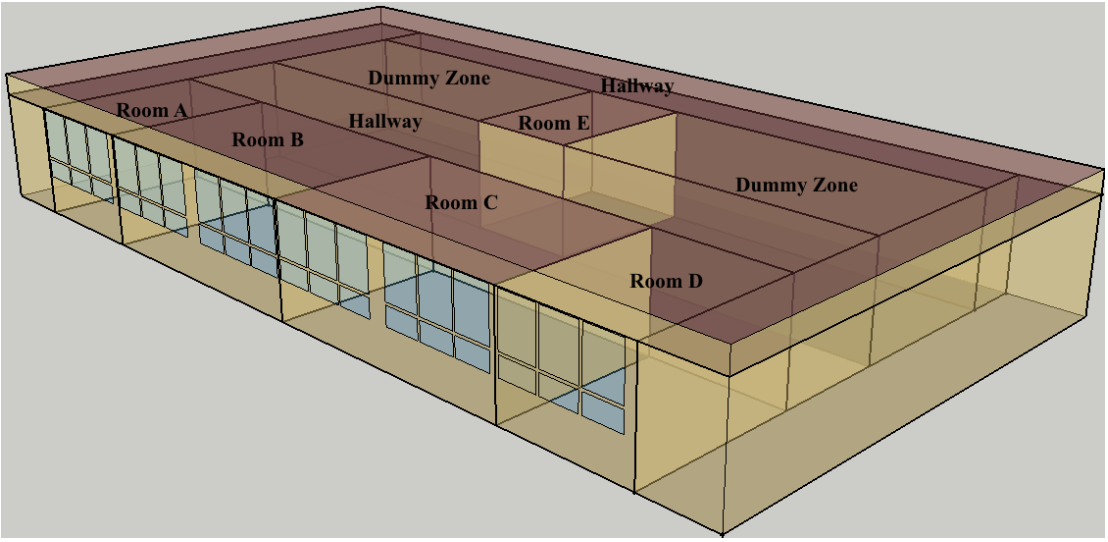

Figure 4-11 Proposed thermal zone distribution

4.3.2 Water Heating Unit Modification

The WHU model needs to be modified before being used in the physical model to estimate the condensing pressure and temperature of the system, as shown in Equation 4-11 and Equation 4-12. When the system is in the cooling main or cooling only mode, which usually happens in summer, the condensing temperature is evaluated with Equation 4-11. In Equation 4-12, when there is no water heating demand, the first term of the equation converges to ambient air temperature. Therefore, in this study, the hot water demand affects the system by increasing the condensing temperature. In Equation 4-12, when the system is in heating only mode, Equation 4-12 converges to the built-in condensing temperature set point. When there is hot water demand, the condensing temperature is affected in the same manner as Equation 4-11.

$$T_{c,cool} = \max\left(T_{whu,out}, T_{amb}\right) + SC + ApprT \quad \text{Equation 4-11}$$

$$T_{c,heat} = \max(T_{whu,out}, T_{c,set}) \quad \text{Equation 4-12}$$

Where $T_{WHU,out}$ means the hot water outlet temperature of WHU, T_{amb} means ambient air temperature, $T_{c,set}$ means the built-in condensing temperature in heating operation, SC means subcooling, and $ApprT$ means the approach temperature between the air and refrigerant at the condenser outlet.

4.3.3 New Thermodynamic VRF Model

The thermodynamic model included models of a variable-speed compressor, a condenser, an EEV, and evaporators. The basic idea is to determine the required compressor frequency and calculate the compressor power. To simulate the real operation strategy of the VRF system, the following practical assumptions were used:

- Lumped parameter models were used for both condenser and evaporator.
- To account for the installation piping length of the VRF system, the pressure drop of the refrigerant flow along the pipes was assumed to happen only between the compressor suction port and IUs, i.e., suction line.
- The condensing temperature in the heating operation and the evaporating temperature in the cooling operation were assumed constant, which was the typical case in the operation strategies of real VRF systems.

The flowchart of the thermodynamic model is shown in Figure 4-12. The model inputs are the operation mode of the system, space cooling load ($\dot{Q}_{sc}$), space heating load ($\dot{Q}_{sh}$), WHU load ($\dot{Q}_{whu}$), operation control parameters, and compressor polynomial equations. The load information was obtained from the thermal balance of the

simulation engine when the weather data and building layout were given. The operation control parameters included the condensing temperature (T_c), evaporating temperature (T_e), subcooling (SC), superheat (SH), and suction pressure drop (PD). These operation parameters could be specified either by testing or using the parameters provided in the operation manual. For example, the user could use measured superheat instead of the superheat mentioned by manufactures' manual (if possible). With measured operation control parameters, the simulation results could show a better agreement with the experimental data. However, to estimate the performance of the VRF system, it is not necessary to measure all the operation parameters. Most manufactures also provide information on the operation control parameters via technical manuals. Therefore, another common practice is to use the default operation control parameters to estimate the long-term performance of the system. For example, in cooling operation, the evaporating temperature and subcooling are usually fixed in most VRF systems. Therefore, instead of measuring all the operation control parameters, the user could also use the built-in operation control parameters to estimate the performance of the system.

The compressor polynomial equations are the basis for the variable speed compressor model. The experimental data was used to generate correlations. After the correlations were created, the model employed the approached recommend by Shao *et al.* (2004) and Dabiri and Rice (1987) to calculate the mass flow rate and energy consumption of the compressor. The details of the model are shown as follows:

First, the experimental data of rated mass flow rate and compressor power under certain frequencies (f_s) was used to derive quadratic correlations based on the condensing and

evaporating temperature, as shown in Equation 4-13 and Equation 4-14. In this study, the rated experimental data under 30, 60, and 90 Hz was used. Therefore, the model required three sets of mass flow rate polynomial equations, namely, for 30, 60, and 90 Hz. Similarly, the model also need three sets of polynomial equations for compressor power.

$$MFR_{rated,f_s} = a_1 T_c + a_2 T_c^2 + a_3 T_c T_e + a_4 T_e^2 + a_5 T_e + a_6 \quad \text{Equation 4-13}$$

$$Power_{rated,f_s} = b_1 T_c + b_2 T_c^2 + b_3 T_c T_e + b_4 T_e^2 + b_5 T_e + b_6 \quad \text{Equation 4-14}$$

Third, the rated mass flow rate and compressor power under this frequency (f) was calculated with a spline interpolation/extrapolation. In this study, the 30, 60, and 90 Hz data were used as the basis for interpolation/extrapolation, as shown in Equation 4-15 and Equation 4-16.

$$MFR_{rated,f} = Interp(MFR_{rated,30Hz,} MFR_{rated,60Hz,} MFR_{rated,90Hz}) \quad \text{Equation 4-15}$$

$$Power_{rated,f} = Interp(Power_{rated,30Hz,} Power_{rated,60Hz,} Power_{rated,90Hz}) \quad \text{Equation 4-16}$$

Finally, in the scenario in this study, the superheat at the compressor inlet could be different from the rated condition. The density difference at the inlet required a superheat correction factor for mass flow rate. The superheat correction factor of mass flow rate was calculated in Equation 4-17. Moreover, the enthalpy change in the compressor would also be different from the rated condition. Therefore, the corresponding compressor power correction factor was calculated, as shown in Equation 4-18.

$$MFR_{real,f} = MFR_{rated,f} * [1 + F_v * (\frac{\rho}{\rho_{rated}} - 1)] \quad \text{Equation 4-17}$$

$$Power_{rated,f} = \frac{MFR_{real,f}}{MFR_{rated,f}} * \frac{\Delta h_{real}}{\Delta h_{rated}}$$ Equation 4-18

In Equation 4-17, the F_v is selected to be 0.75 as recommend by Dabiri and Rice (1987). After collecting the inputs, the model starts with a guess value of compressor frequency (f). Based on the previous compressor model and the operation control parameters, the mass flow rate, compressor power, and the compressor suction port refrigerant state could be calculated.

Based on energy balance of the compressor, the refrigerant state of discharge port could also be calculated. Because the subcooling is known, the model could further calculate the condensing capacity ($\dot{Q}_c$). After the condenser, the refrigerant goes through an isenthalpic expansion in the EEV. The refrigerant state of the EEV outlet and evaporator inlet could therefore be calculated. Based on the enthalpy difference across the evaporator and the mass flow rate, the evaporating capacity ($\dot{Q}_e$) could be calculated. Based on the operation mode, the capacity would be compared to the required load. If the relative difference was less than the tolerance (ε), this frequency was chosen as the frequency that the compressor should run with. The model further calculated the energy consumption of the compressor. Otherwise, the model kept iterating until convergence was reached. The final outputs would be the target compressor frequency matching the load and the energy consumption of the compressor.

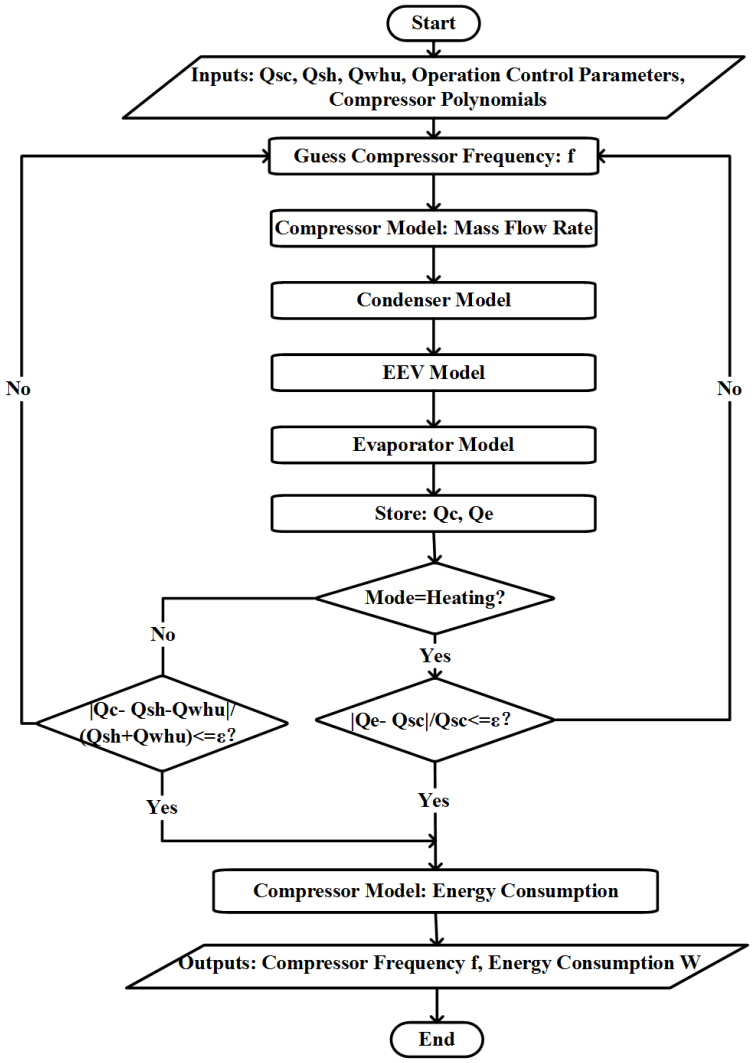

Figure 4-12 Thermodynamic VRF model

4.4 Results and Validation

The field test results of the MFVRF were used to validate the developed model. There were no occupants in the building during the test. All the lights were turned off. Therefore, the only internal load included in the test was the electric equipment load such as computers, printers, and fax machines.

4.4.1 Cooling Energy Validation

The simulated heat transfer capacity was compared to that of the experiment using both improved and original building layout. Figure 4-13 shows the hourly comparison between the simulated and experimental results with the building layout shown in Figure 4-10. Figure 4-14 shows the hourly comparison between the simulated and experimental results with the proposed building layout in Figure 4-11. It can be found in Figure 4-13 that the simulated results using the previous building layout is much higher than the experimental results. The hourly deviation is higher the 20%. The main reason for this deviation is due to the missing temperature information of the hallway. Since the hallway was modeled as an uncontrolled zone, the temperature of the hallway could reach as high as 28°C. In such conditions, the cooling load of the room served by VRF systems would thereafter be overestimated. The proposed building layout resolved the thermal load issue by dividing the hallway into convex subzones. The temperature of the hallway was simulated based on the temperature profile measured in the field tests. The results of the proposed building layout are shown in Figure 4-14. The simulated results distributed within ±20% of the experimental data, and are much improved when compared to Figure 4-13. To quantify the agreement between the experimental data and the improvement by introducing proposed building layout, the CvRMSE and NMBE values are listed in Table 4-5. The proposed building layout only overestimates the room load by 10%.

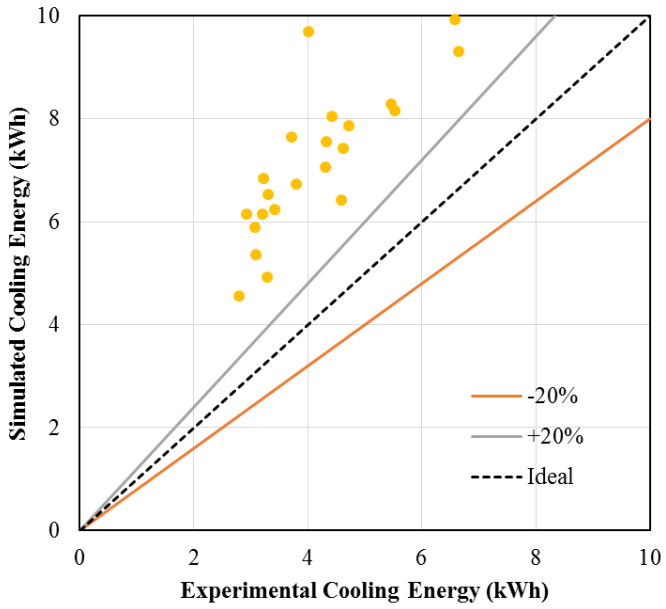

Figure 4-13 Hourly cooling energy validation with previous building thermal zone

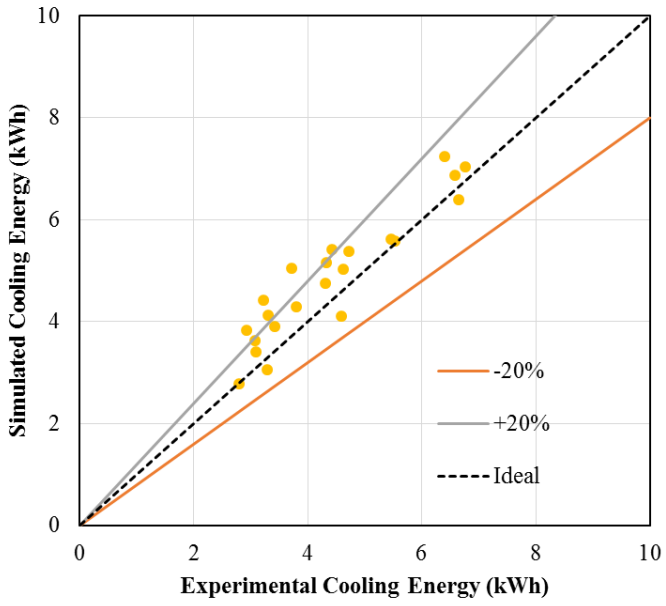

Figure 4-14 Hourly cooling energy validation with proposed building thermal zone

Table 4-5 CvRMSE and NMBE in hourly cooling energy validation

Metrics	Previous Layout (%)	Proposed Layout (%)
CvRMSE	74.2	14.4
NMBE	73.3	9.9

4.4.2 Energy Consumption Validation

As shown in Figure 4-8, the flowchart of the model starts with the load estimation and continues with the thermodynamic model to estimate the energy consumption. Since the proposed building layout could estimate the room thermal load with a 14.4% deviation, the proposed building layout is used to further illustrate the effect by introducing the thermodynamic model.

The hourly energy consumptions of the VRF system with the previous calculation approach and the proposed approach are shown in Figure 4-15 and Figure 4-16, respectively. As shown in Figure 4-15, simulated hourly energy consumptions of the system are still outside of the ±20% bound. The reason is the oversizing of the system. The nominal cooling capacity was 28.1 kW. However, in this study, the cooling load of the building was less than 10 kW. The VRF system was working with a part load ratio (PLR) of less than 50%. Moreover, the compressor worked under a low frequency, and the system could be in On/OFF operation when the frequency was less than a certain threshold. However, the performance map provided by the manufactures does not provide compressor information other than the indoor and outdoor air temperature.

Therefore, previous approach overestimates the energy consumption because the map itself does not consider the variable frequency of the compressor.

On the contrary, the thermodynamic model calculates the performance of the compressor under arbitrary frequency with the compressor polynomial equations. The operation of the compressor, which is excluded from the previous approach, is a very important part of the thermodynamic model. The model seeks to match the load by varying the compressor operation parameters. Therefore, matching the load becomes the first priority. The model does not calculate the energy consumption until the load is matched. The results of the new approach are shown in Figure 4-16. It can be found that most of the results are within ±20% bound. To quantify the improvement, the CvRMSE and NMBE are shown in Table 4-6. The thermodynamic model only overestimates the hourly cooling energy consumption by 10%.

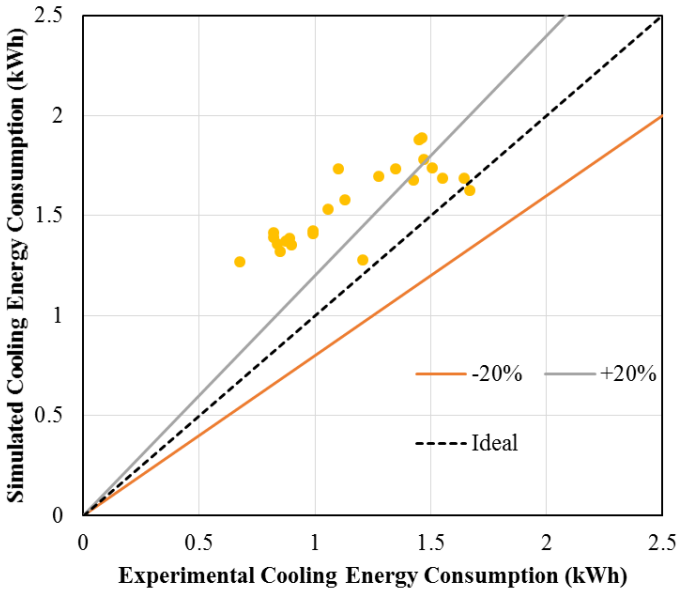

Figure 4-15 Hourly cooling energy consumption validation with previous approach

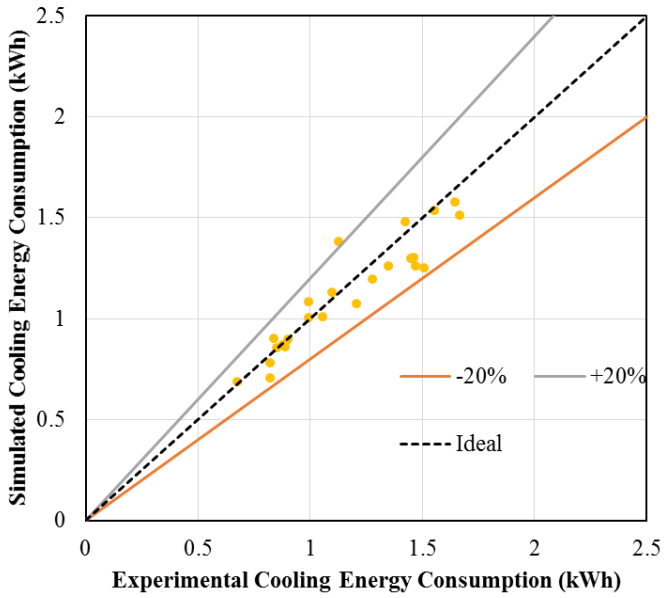

Figure 4-16 Hourly cooling energy consumption validation with proposed new model

Table 4-6 CvRMSE and NMBE in hourly energy consumption validation

Metrics	Previous Approach (%)	New Thermodynamic Model (%)
CvRMSE	37.4	10.0
NMBE	34.6	3.7

4.5 Model Extensibility: Energy Saving Control

The proposed approach with the improved building thermal layout and thermodynamic model could predict the system performance more accurately. However, it should be noted that in the thermodynamic model, the operation control parameters use the data

measured in field tests. In the practical application of the VRF model, it is time-consuming and inefficient to obtain all the working parameters of the system throughout experiments, especially in long-term estimation, such as the annual estimation of the energy consumption of the VRF system. Therefore, a better way would be to estimate the energy consumption based on VRF control algorithm. The new VRF model was designed to be compatible with different control strategies.

4.5.1 Variable-Speed System Control

As mentioned by Chen *et al.* (2005), the control mechanism of VRF system is less discussed in existing literature when compared to the performance of the system. Therefore, it is useful to take a look at the control concept of variable-speed air conditioners before discussing the control strategy of VRF systems. Figure 4-17 and Figure 4-18 show the control concept in cooling and heating operation, respectively. Figure 4-17 shows the relationship between the cooling energy delivered by the system and the evaporating temperature under a series of compressor operation frequencies (f_i). The solid compressor performance lines share the same condensing temperature. The dotted line represents a lower condensing temperature and the dashed line has a higher condensing temperature. Similarly, Figure 4-18 shows the change of heating capacity. In both figures, the compressor frequency increases from f_4 to f_1.

In Figure 4-17, with the same evaporating temperature and condensing temperature, cooling capacity increases along with the increase of frequency, which is shown by the solid compressor performance lines. Meanwhile, with the increase of evaporating temperature, the temperature difference between air and refrigerant decreases. The amount of heat transferred between the refrigerant and the air decreases, as is shown

by the evaporator performance line. If the compressor frequency is fixed at f_1, state A will be the final system state. As shown in Figure 4-17, a cooling capacity of Q_1 is delivered by the system. After the system been stabilized, a change in the operation conditions could cause the state of the system move between the dotted and dashed lines. For example, as Shi (2000) pointed out, with a reduced ambient temperature, the system could move to state C. Similarly, an increase in the ambient temperature could move the system to state B. However, during the cooling operation, when the ambient temperature decreases, the cooling demand of the room decreases. If the compressor frequency is to stay the same, the final state of the system would move to state D to provide a lower cooling capacity of Q_2. However, the evaporating temperature at state D is much lower than designed evaporating temperature, which is usually designed based on state A. The efficiency of the compressor is also lower. Moreover, with a lower evaporating temperature, the latent load is higher. However, the typical latent cooling load in the room is lower at a lower ambient temperature. To address these issues, variable-speed systems reduce the compressor frequency to f_2 to keep the designed evaporating temperature. The final system state moves from A to state E, instead of state D.

The same phenomenon is also observed in heating operation, which is shown in Figure 4-18. In Figure 4-18, when compressor frequency is fixed, a change in heating operation condition would cause the state of the system to move from A' but still stay between the dotted and dashed lines. At higher ambient temperature, the system state moves from C' to a lower state B'. However, when the heating load drops to Q_2 along with the increase of the ambient temperature, the state of the system moves to D'. At

state D', the condensing temperature is much higher than designed condensing temperature. To keep the same condensing temperature, variable-speed systems reduce the compressor frequency to relocate the system to state E'.

However, the detailed control procedures between two states vary from system to system. When compared to other variable-speed systems, VRF systems have higher controller flexibility and systematic complexity. The details of VRF controller mechanism are also less known to the researchers due to commercial confidentiality. What is known so far is that the manufacturers generally use lookup tables to forecast the performance of the system and to control compressors, as reported by Tu *et al.* (2010). This can be shown by Figure 4-19. Based on ambient conditions, the VRF controller estimates the building load in advance. It references a table to find out the proper compressor frequency to meet the estimated building load. The map is generated by laboratory testing based on preset operation conditions. For example, in the cooling operation map, the evaporating temperature is the designed value based on rated condition where the ambient temperature is 35°C. The control method shown in Figure 4-19 is called "conventional VRF control". The conventional VRF control accepts built-in operation control parameters and matches the indoor load by compressor regulation. The conventional VRF control is embedded on the new VRF model before the introduction of energy saving controllers.

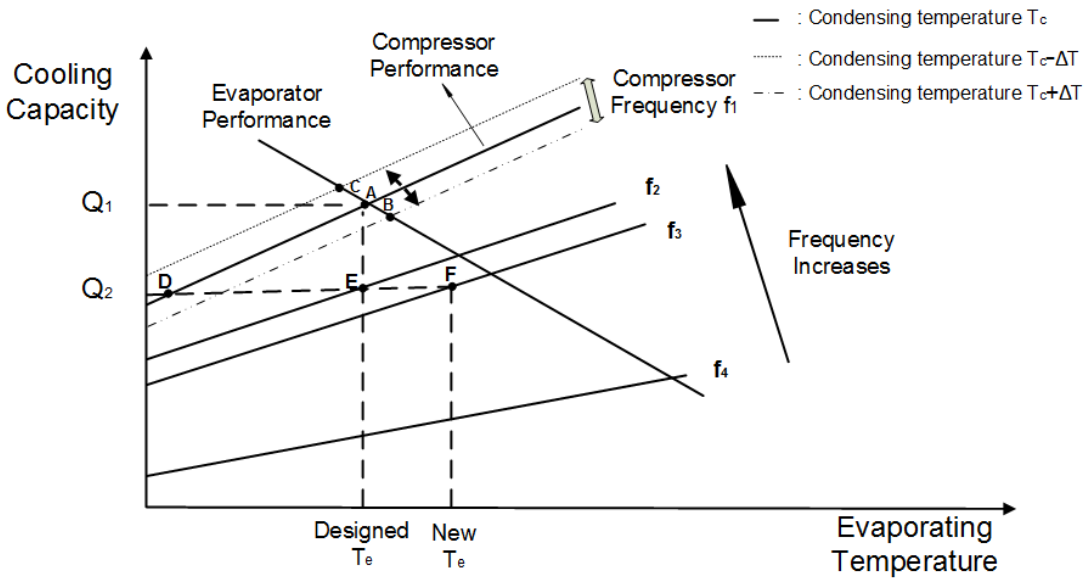

Figure 4-17 Variable-speed system cooling capacity control

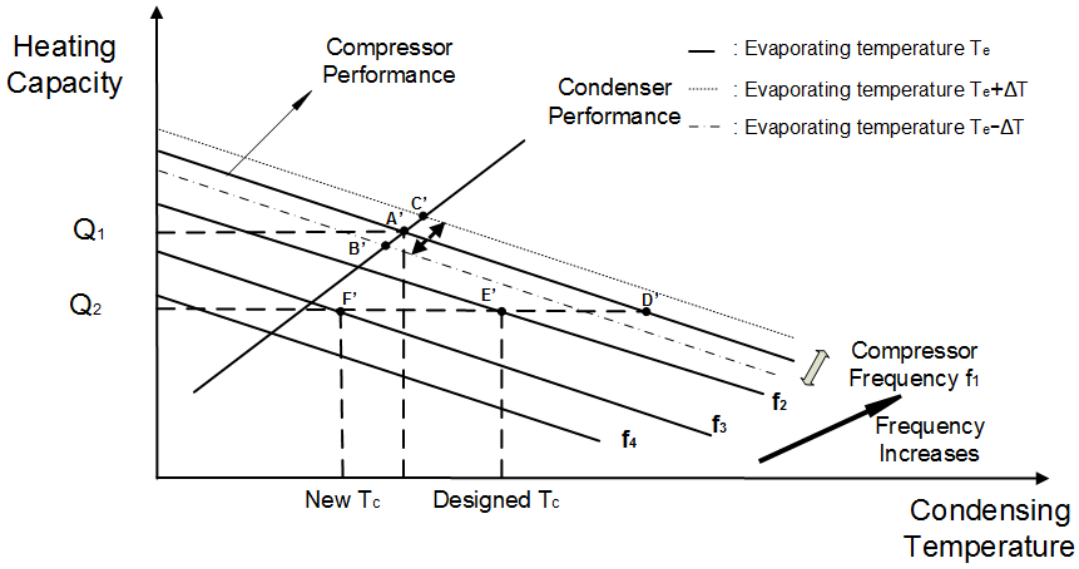

Figure 4-18 Variable-speed system heating capacity control

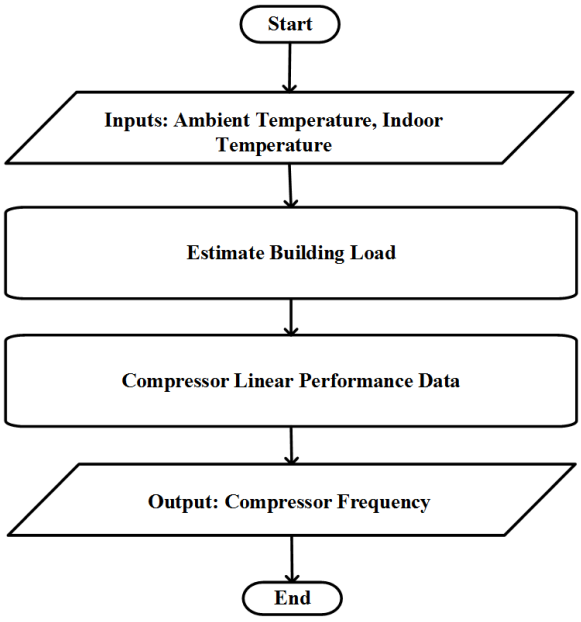

Figure 4-19 Conventional VRF control

4.5.2 Conventional VRF Control

The built-in control parameters of the conventional VRF control were derived from the manufacturer's control manual and field tests. The parameters used for the cooling operation control are listed in Table 4-7. The simulated hourly energy consumption results are shown in Figure 4-20. The effect of the built-in operation control parameters on CvRMSE and NMBE is shown in Table 4-8. In Figure 4-20, the deviation between the experimental and simulation results increases, which is due to the fact that the model is not using measured parameters. Therefore, the CvRMSE, which means the agreement between the experiments and simulation, increases from 10.0% to 11.0%. However, the NMBE is still less than 5%, which means the model is capable of accurately predicting the performance of the system with the built-in control parameters. Therefore, this set of built-in operation control parameters could be used in the long-term simulation to estimate the energy consumption of the system.

Table 4-7 Built-in cooling operation control parameters

Parameters	Built-in Values
Evaporating Temperature	6.2°C
Subcooling	7.5 K
Superheat	5 K

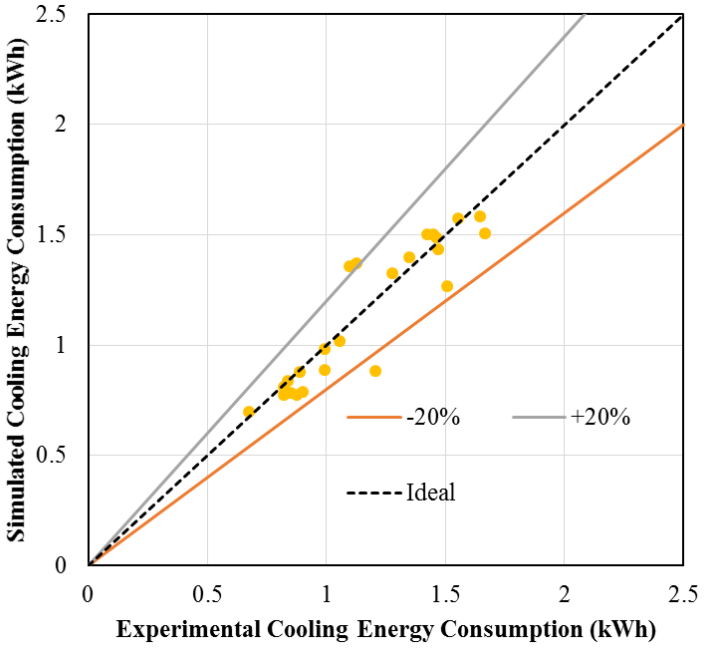

Figure 4-20 Hourly cooling energy consumption validation with conventional VRF control

Table 4-8 Control strategy comparison

Metrics	With Measured Parameters (%)	With Built-in Parameters (%)
CvRMSE	10.0	11.0
NMBE	3.7	2.0

4.5.3 Energy Saving Control

In order to reduce the energy consumption, VRF systems can search for the operation point in a wide range of conditions. For example, as shown in the experimental work from Anyur *et al.* (2008) and Shao *et al.* (2004), VRF systems could operate under a lower frequency with a higher evaporating temperature than the designed condition but still deliver sufficient amount of refrigerant to the IUs, which reduces the energy consumption.

In both cooling and heating mode, it is possible to utilize the wide operation range of VRF system to achieve higher energy saving. As we can find in Figure 4-17, the control of evaporating temperature is critical to energy saving in the cooling season. Zhao *et al.* (2015) tested a 22.4 kW VRF system with four indoor units and found that by increasing the evaporating temperature from 8°C to 12°C, 15% energy saving could be achieved. In Figure 4-17, when the building cooling load decreases to Q_2 with an increase of ambient temperature, we can further move the state of the system to state F by keeping a higher evaporating temperature. The compressor frequency drops and energy saving could be achieved. Moreover, using a higher evaporating temperature at lower ambient temperature can also provide a proper sensible cooling. Similarly, in the

heating operation, a lower condensing temperature could move the state of the system to F' and the system could save more energy. Therefore, instead of using single linear map based on single evaporating/condensing temperature, an energy saving control strategy was proposed to determine the compressor frequency under a varying evaporating/condensing temperature. The control strategy follows two rules:

- The evaporating temperature of the system is adjusted linearly from 11°C to 4.2°C when the ambient air temperature increases from 20°C to 35°C.
- The condensing temperature of the system is adjusted linearly from 50°C to 40°C when the ambient air temperature increases from -10°C to 5°C.

4.5.4 Seasonal Performance of Energy Saving Control

The energy saving control was designed to cover a wide ambient temperature range in both cooling and heating season, respectively. To show its performance improvement, weather data from cities with high cooling/heating load were used. For cooling operation, weather data of Miami was selected due to the high cooling load. For heating operation, weather data of Chicago was used.

The simulated cooling season performances of the energy saving control strategy and conventional invariant control are shown in Figure 4-21. The set point of the rooms was 25°C. The running period of the model was from July to September. The TMY3 weather data of Miami, Florida was used. As shown in Figure 4-21, by using the new control strategy, the daily energy consumption is reduced. Overall, the seasonal energy consumption is reduced from 2,899 kWh to 2,701 kWh with energy saving of 6.8%.

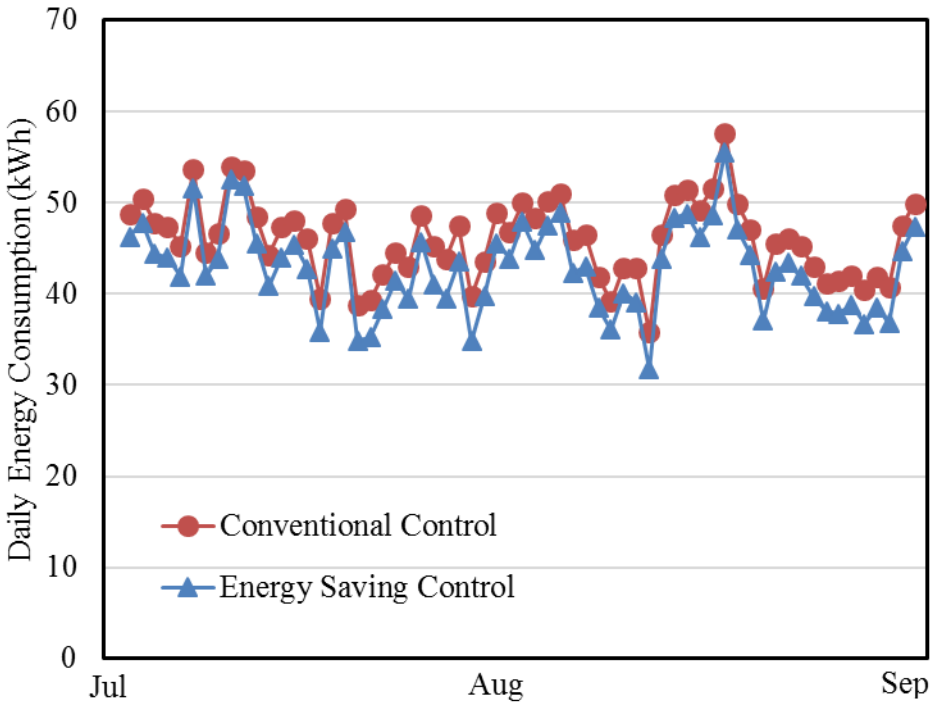

Figure 4-21 Daily energy consumption comparison between two control strategies in cooling (Miami, FL)

Similarly, the simulated heating season performance of the new control strategy is shown in Figure 4-22. The set point of the rooms was 22°C. The running period of the model was set to be from January to March. The TMY3 weather data of Chicago, IL was used. As shown in Figure 4-22, by using the new control strategy, the daily energy consumption is reduced. Overall, the seasonal energy consumption is reduced from 3,814 kWh to 3,276 kWh with energy saving of 14.1%.

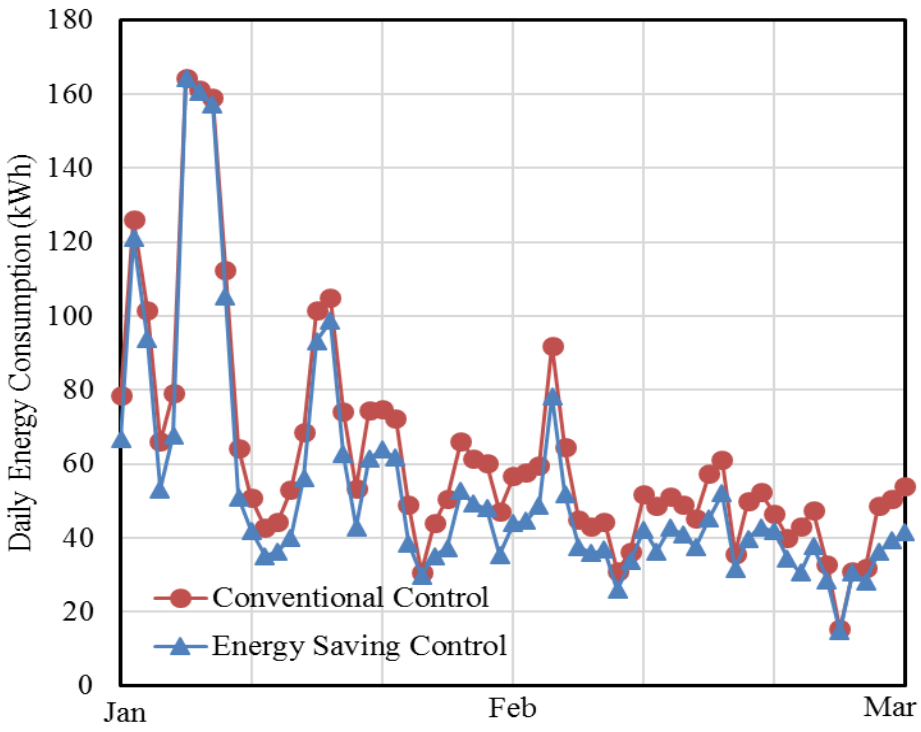

Figure 4-22 Daily energy consumption comparison between two control strategies in heating (Chicago, IL)

To demonstrate the impact of energy saving control when used in different climate zones, this work also investigated the performance of the new control in four representative cities (Miami, Houston, Baltimore and Chicago) for both cooling and heating season performance. The results are shown in Table 4-9 and Table 4-10. Overall, the highest cooling seasonal energy saving by the new control strategy is 10.8% in Chicago and the highest heating seasonal energy saving is 15.4% in Baltimore.

Table 4-9 New control strategy cooling energy saving variation by location

Locations	Miami, FL	Houston, TX	Baltimore, MD	Chicago, IL
Energy Saving (%)	6.8%	5.2%	8.9%	10.8%

Table 4-10 New control strategy heating energy saving variation by location

Locations	Miami, FL	Houston, TX	Baltimore, MD	Chicago, IL
Energy Saving (%)	10.5%	11.2%	15.4%	14.1%

4.6 Model Extensibility: VRF with Chilled Water Storage

4.6.1 VRF with Chilled Water Storage

As found in the field testing, the MFVRF system has a low utilization of water heating unit. Meanwhile, VRF system also has the degradation of the performance during the summer peak period due to the high condensing temperature. Since MFVRF system includes a plate heat exchanger to provide hot water, a new concept was generated to covert the WHU in MFVRF into a chilled water storage (CWS) unit and use the chilled water to reduce the condensing temperature during the cooling peak period. Based on this concept, a VRF system with CWS was proposed. The schematic diagram of the

system in charging mode is shown in Figure 4-23. In Figure 4-23, the discharged refrigerant leaving the compressor rejects heat to the ambient air in the OU HX. The subcooled refrigerant is sent to HRU and further delivered to IUs. Meanwhile, the two-phase refrigerant is sent to the plate heat exchanger after the expansion valve. However, instead of heating up the water, the plate heat exchanger in this case generates chilled water. Therefore, it works similarly to a cooling IU. The chilled water is stored in the water tank.

During the summer peak period, the VRF system is working under a higher condensing pressure than usual. With a high pressure ratio across the system, the performance of VRF system is highly deteriorated, as found in Kwon *et al.*'s study (2012). With CWS, it is possible to switch the system to water-sink operation during summer peak period. The discharging mode of the system is shown in Figure 4-24. In Figure 4-24, by manipulating the solenoid valves, the discharged refrigerant bypasses the OU heat exchanger and flows to the plate heat exchanger. In the plate heat exchanger, the refrigerant is cooled down to liquid state and delivered back to HRU. The HRU further delivers the liquid refrigerant to the IUs that need cooling. What needs to be pointed out is that such a system could not be simulated based on the performance mapping models. The overall modeling approach of this system is shown in Figure 4-25. It has an additional logic loop which decides the operation mode of the system. When the ambient temperature is higher than a certain temperature, the system works in a water-cooled (discharging) mode where the chilled water is used. When the ambient temperature is lower, the system works in the charging mode where the water in the storage tank is cooled down. The model iterates between the chilled water part and the

OU model until the condensing capacity requirement of the OU matches the sensible capacity of the water tank.

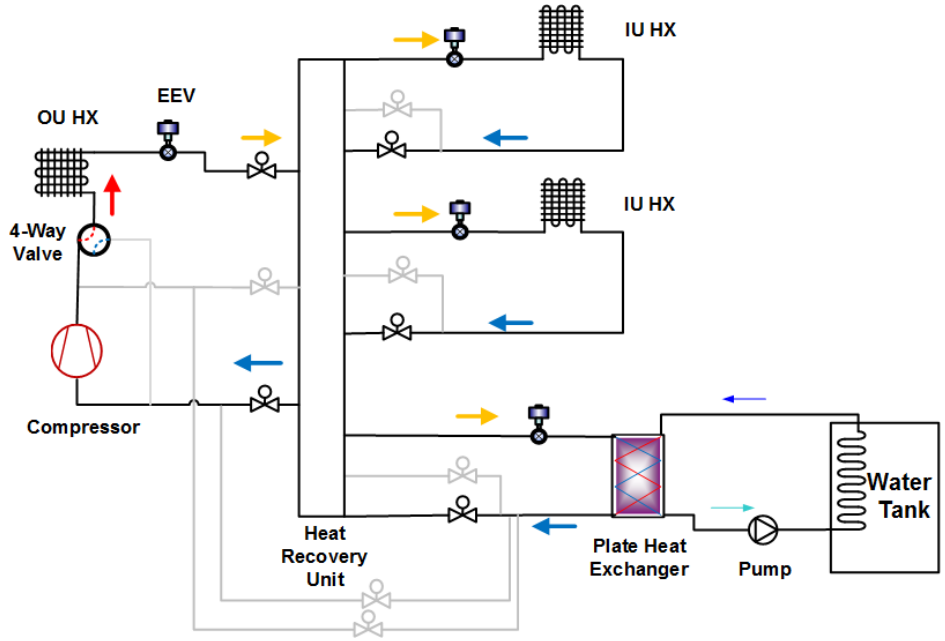

Figure 4-23 VRF with CWS in charging mode

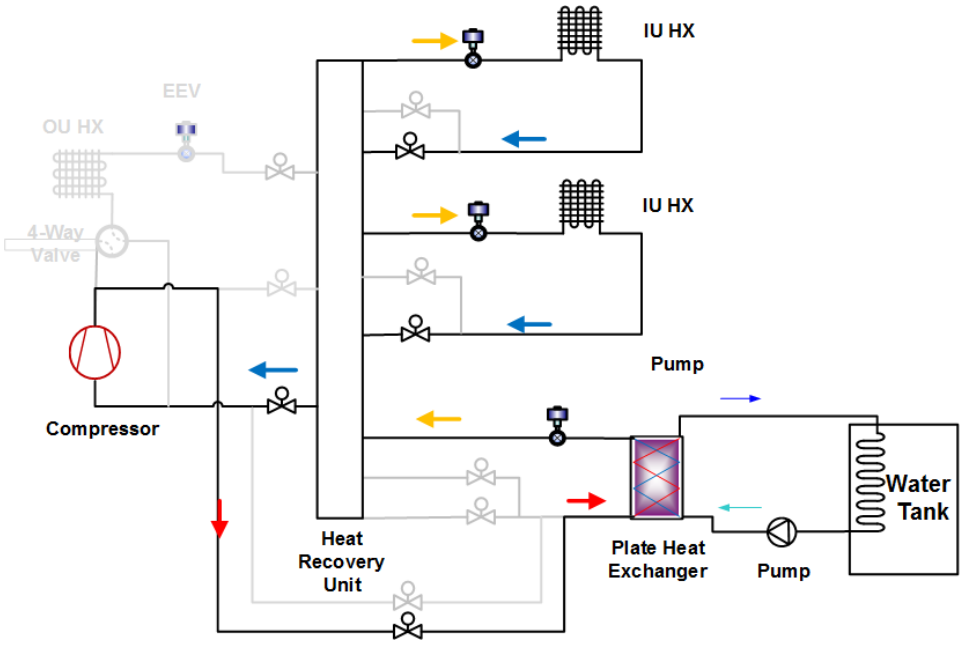

Figure 4-24 VRF with CWS in discharging mode

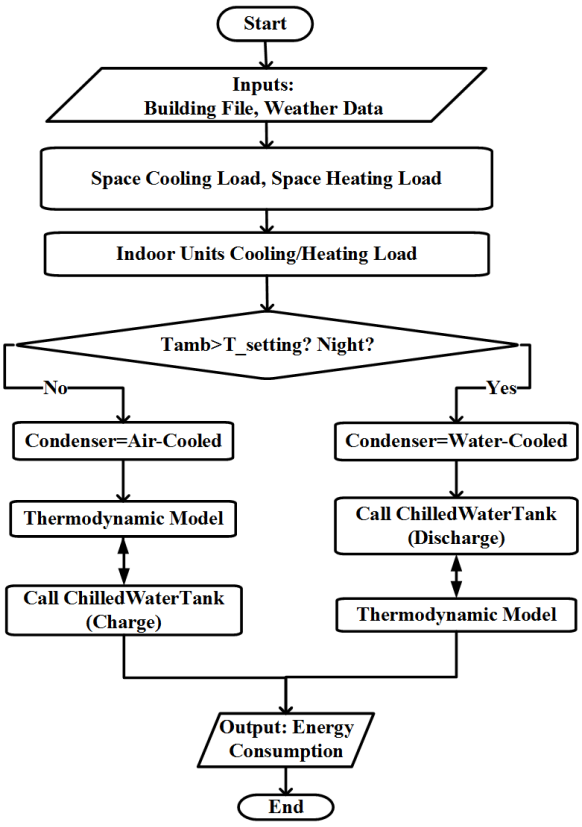

Figure 4-25 Flowchart of VRF with CWS

4.6.2 Seasonal Performance

In the new VRF system with CWS, it was assumed the storage tank had a total volume of 1000 L. The activation temperature of chilled water discharging control was assumed to be 27°C. The target chilled water temperature was assumed to be 20°C. The set point of the rooms was 25°C. The simulation period was from July to September. The TMY3 weather data of Miami, FL was used. The daily energy consumptions of the new system and HPVRF system are shown in Figure 4-26. It could be found that the new system consumes less energy than HPVRF system. Overall, the energy consumption of HPVRF system is 2,899 kWh and that of the new system is 2,587 kWh. The overall cooling seasonal energy saving is 10.7%.

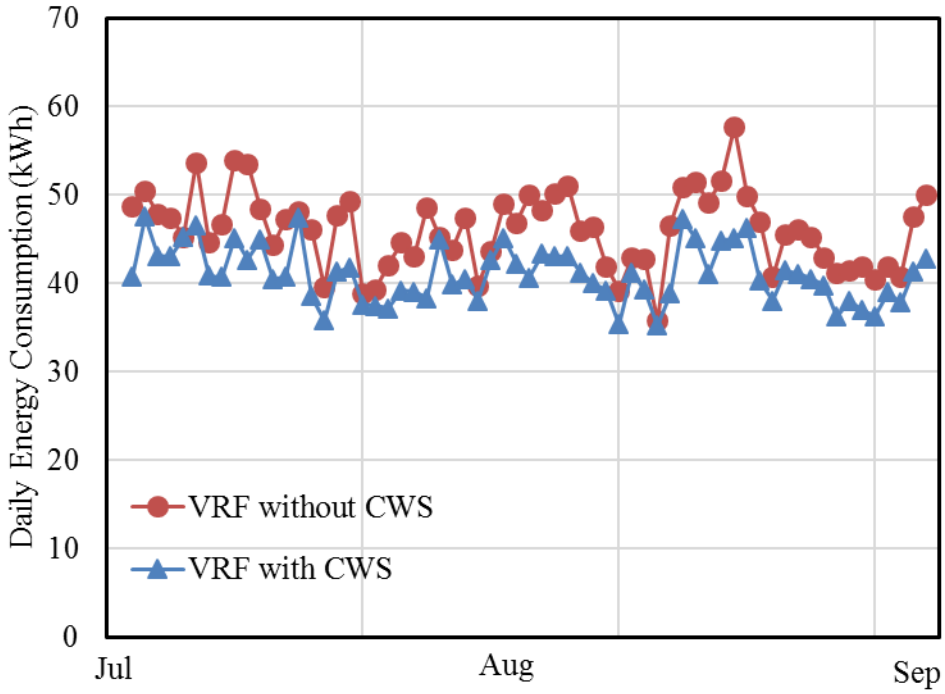

Figure 4-26 Daily energy consumption comparison for VRF systems with and without CWS (Miami, FL)

Similarly, VRF with CWS was also simulated in four representative cities Miami, Houston, Baltimore and Chicago for cooling season performance. The results are shown in Table 4-11. VRF system with CWS has the highest cooling energy saving when used in Houston, which is 12.5%.

Table 4-11 VRF with CWS energy saving variation by location

Locations	Miami, FL	Houston, TX	Baltimore, MD	Chicago, IL
Cooling Season Energy Saving (%)	10.7%	12.5%	6.7%	5.1%

5 Variable Refrigerant Flow System with Phase Change Material Based Thermal Energy Storage

5.1 New VRF System with PCM based TES Configuration

As mentioned in the literature review section, the existing studies of air conditioning systems integrated with TES focus on cooling or heating energy saving. However, VRF systems are designed to work in both cooling and heating seasons. In chapter 4, the possibility of using CWS with VRF was discussed. It should be pointed out that VRF with CWS uses the chilled water to reduce the peak period energy consumption. However, such system could only provide energy saving in the cooling season. Therefore, it is necessary to investigate the possibility of using single TES to provide energy saving in cooling and heating season, which is the focus of this chapter.

This dissertation proposed a VRF system integrated with single TES that supports both cooling and heating season operation. The overall system concept is shown in Figure 5-1. When compared to baseline VRF system, the new VRF system with PCM based TES has an extra TES unit which is connected to HRU. The TES is based on PCM. Moreover, there is a pump located between TES and the IUs. The operation of the new VRF system with PCM based TES is illustrated from Figure 5-2 to Figure 5-5. In Figure 5-2, the IUs are in the cooling mode. The liquid refrigerant from the HRU expands and absorbs heat from TES. The superheated vapor refrigerant leaves the TES and flows back to HRU where it merges with the vapor refrigerant from the IUs and is sent back to the compressor. During this process, the PCM in TES is solidified by the refrigerant flow. After the solidification, it is possible to provide cooling to the rooms by the

melting of PCM, as shown in Figure 5-3. In Figure 5-3, the OU is turned off. The refrigerant leaving the IUs is circulated by the pump and sent to TES. In TES, the refrigerant flow is cooled down by solidified PCM and sent back to the IUs. During this process, the PCM in TES is melt by the refrigerant flow.

The same system could also be used for heating. During the heating operation, the discharged refrigerant vapor from the compressor is sent to HRU. In HRU, part of the refrigerant flows to the TES while the rest to the IUs. In TES, the refrigerant flow melts PCM to the liquid state and is sent back to the HRU. Therefore, after the operation mode shown in Figure 5-4, the TES is filled with liquid PCM. During the heating operation, when the ambient temperature is low, it is possible to use the PCM as the evaporator, as shown in Figure 5-5. In Figure 5-5, the refrigerant is discharged by the compressor and sent to IUs via the HRU. After releasing the heat to the rooms, the liquid refrigerant flows back to HRU. Instead of sending the liquid refrigerant to the heat exchangers in OU, the HRU sends the refrigerant to TES. In TES, the liquid refrigerant expands and absorbs heat from PCM. Therefore, the PCM is solidified by the refrigerant. The operation mode shown in Figure 5-5 increases the evaporating temperature and could reduce the energy consumption of the system.

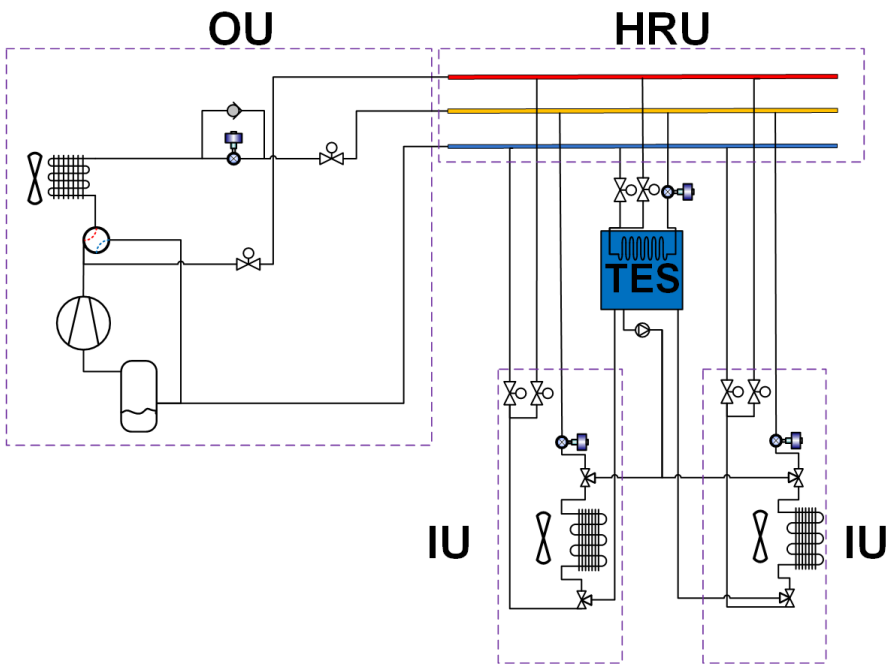

Figure 5-1 Overview of new VRF system with PCM based TES

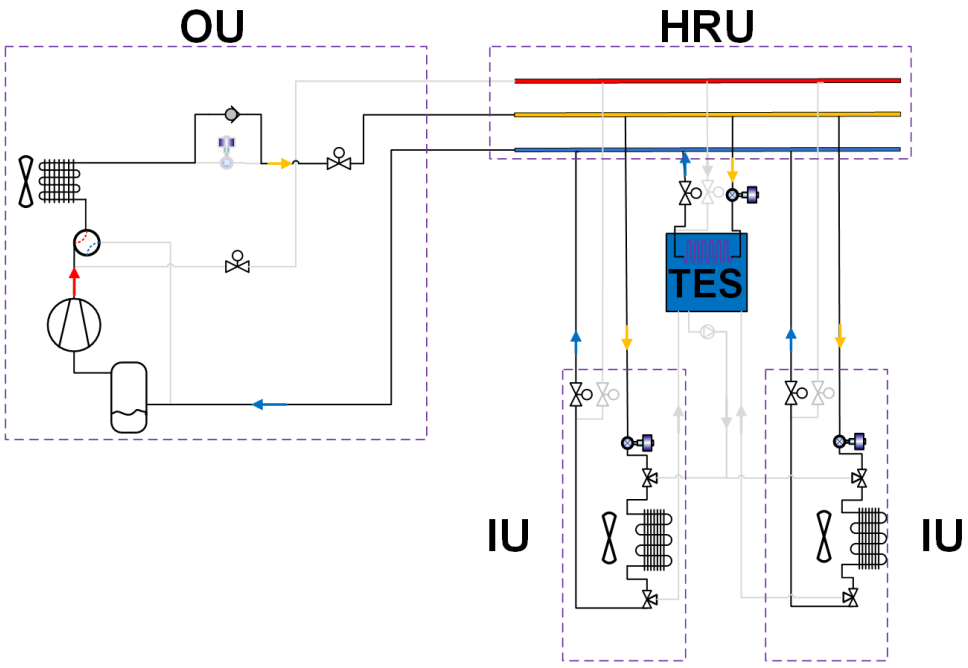

Figure 5-2 New VRF system with TES cooling mode: PCM solidification

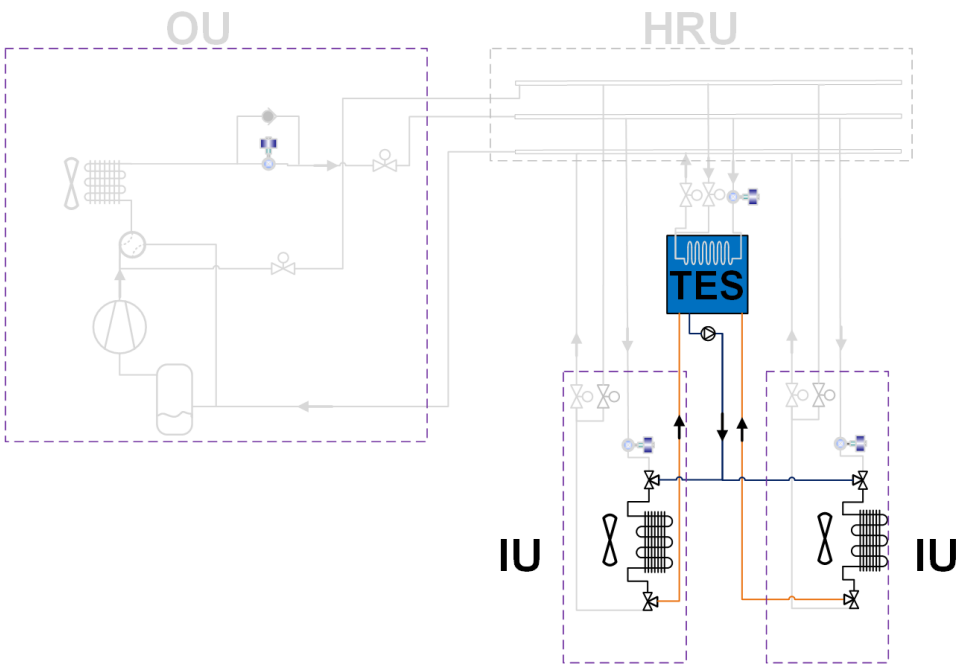

Figure 5-3 New VRF system with TES cooling mode: PCM melting

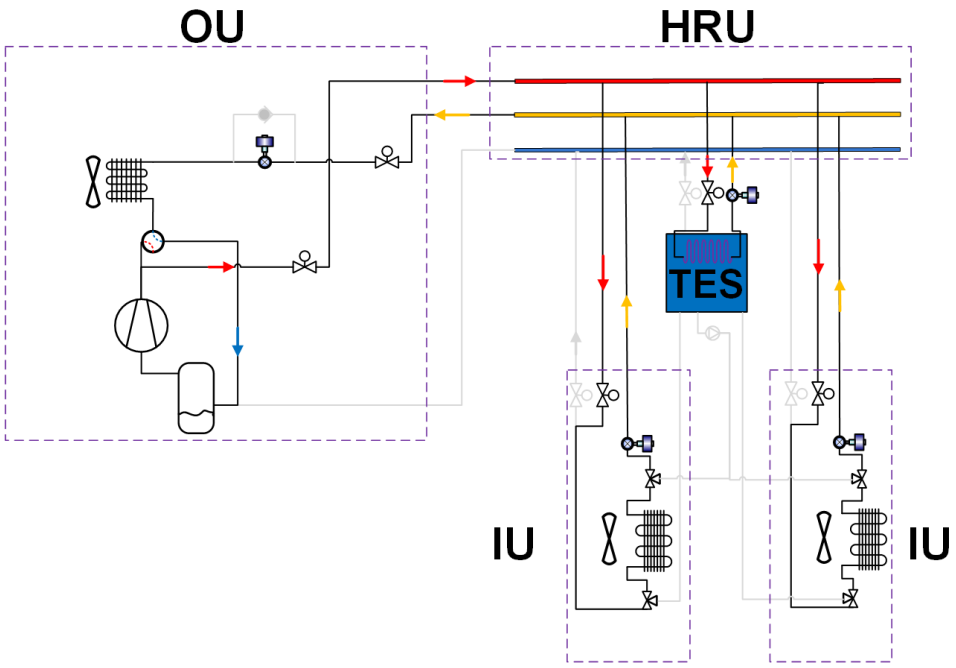

Figure 5-4 New VRF system with TES heating mode: PCM melting

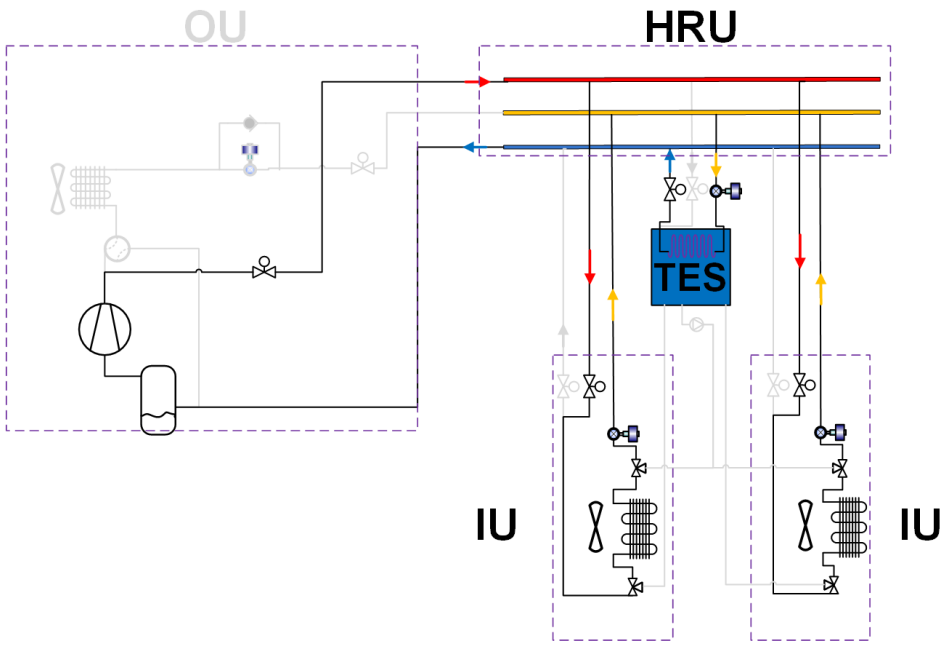

Figure 5-5 New VRF system with TES heating mode: PCM solidification

5.2 Operation Scenario

5.2.1 Overall Architecture

As mentioned in Chapter 1, the benefit of VRF system with TES should consider both EE and DR potential. In order to achieve that, the overall architecture of system operation should follow what is shown in Figure 5-6. As can be seen, Figure 5-6 takes into account three different aspects of operation:

- Incentive programs that motivate the utilizing of TES.
- Facility operation schedules that focus on EE/DR targets.
- Load information of the building.

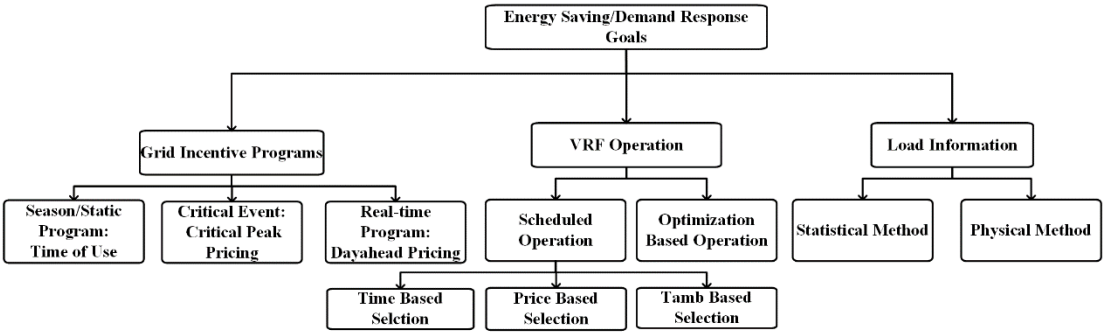

Figure 5-6 Overall architecture of demand response and energy efficiency operation

There are different types of grid incentive programs in the market. For example, time-of-use (ToU) program is a seasonal program by electricity companies. A typical ToU program, as shown in Figure 5-7, is defined by a ToU ratio which describes the difference between peak period and off-peak pricing. The ToU program is provided by companies two to three months ahead of cooling/heating season. It usually applies to the commercial end-users. However, the residential users could also opt in. Since it is provided ahead of the cooling/heating season and lasts for couple of months, it is regarded as a static program. ToU program has a long history and could date back to 1970s. However, during the cooling and heating season, it is possible that grid failures could happen due to emergent events such as extreme weather conditions or infrastructure failure. In order to reduce the congestion of the grid during emergent periods, the grid companies also provide critical peak pricing (CPP) in addition to ToU program. As shown in Figure 5-8, the price during the critical period could be 10 times as high as off-peak period. By doing so, it is expected that the users would avoid high electric demand during the peak period. When compared to ToU program, CPP

program needs to forecast and broadcast the critical events days ahead. Since it is a useful compensation to ToU program, CPP program is also widely used. For example, ToU programs have been used in all of the following states: Maryland, New York, Florida, Texas, California and Washington. Among these states, only Washington does not have a widely used CPP or CPP-like program. One drawback of CPP is that the electricity demand following the critical event is observed to be higher than normal due to the compensation from the user side. Therefore, a future incentive program that introduces the dynamic feature is proposed and tested by grid companies. It is called day-ahead real-time pricing. The basic idea is to provide the users the real-time pricing of the next day six hour ahead. Therefore, the users could determine the operation of the system to achieve the lowest electricity cost. The real-time pricing, as it is designed, could considers both peak demand and the future critical events in the grid. However, the concept of real-time program is much more difficult to implement when compared to ToU or CPP program. For example, when compared to ToU program, real-time programs have only been tested or implemented in part of Maryland, New York and California as pilot programs.

For the facility operation, it could also be categorized into two types: the scheduled operation and optimization-based operation. For example, the scheduled operation could control the operation of the system based on the pricing signal. In addition to the pricing signal, ambient temperature or time could also be used. The drawback of scheduled operation is that it couldn’t capture the real-time performance change of the system and the market.

For the load information, there are two ways of achieving such information: the statistical approach or the physical approach. The statistical approach is based on accumulated historic data to predict the load information of the building. It is fast but it needs sufficient data to make an accurate prediction. The physical approach is based on heat and mass transfer of the building and is usually based on building simulation tools.

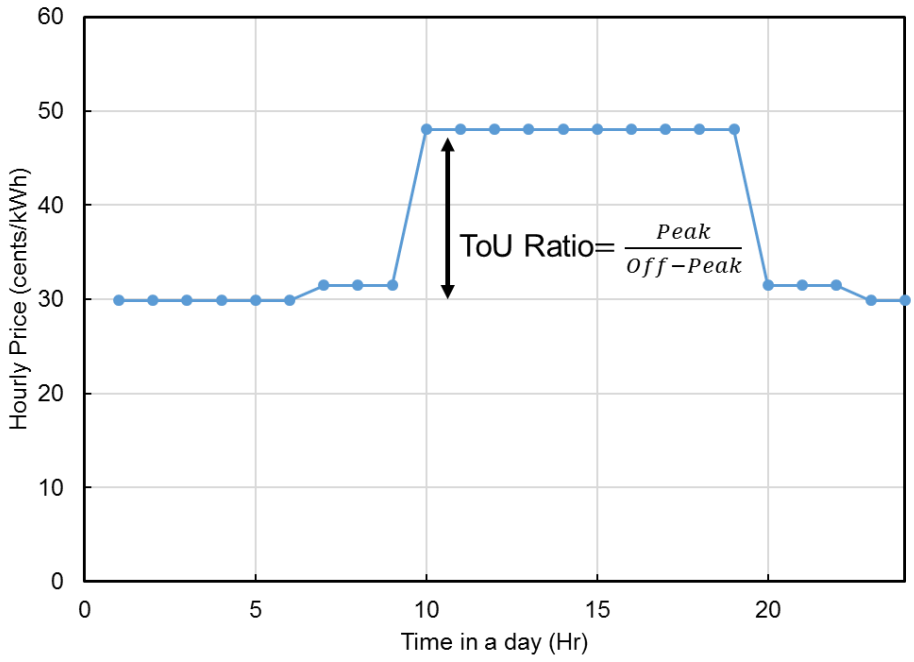

Figure 5-7 Time-of-use pricing

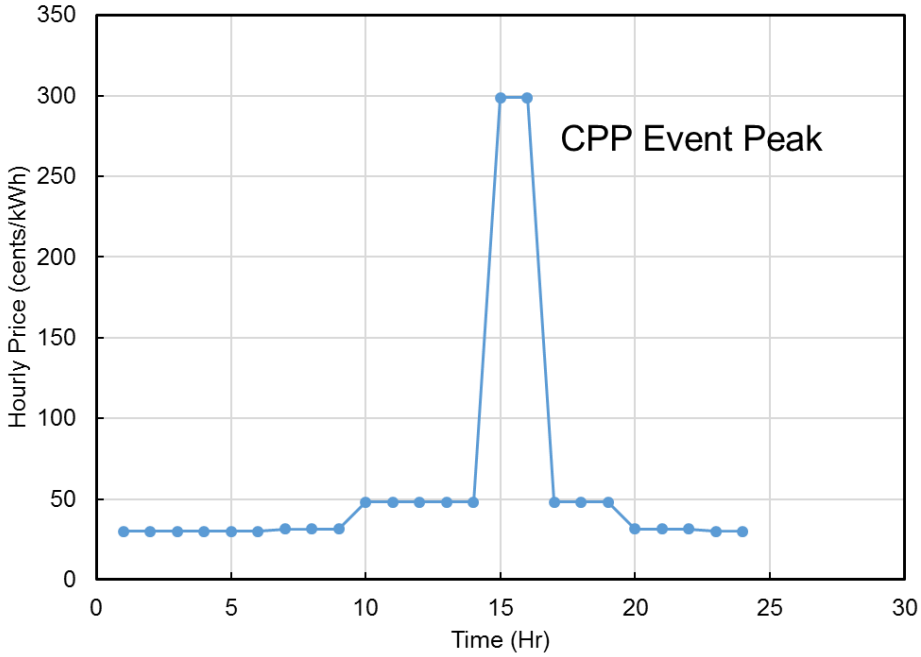

Figure 5-8 Time-of-use with critical peak pricing

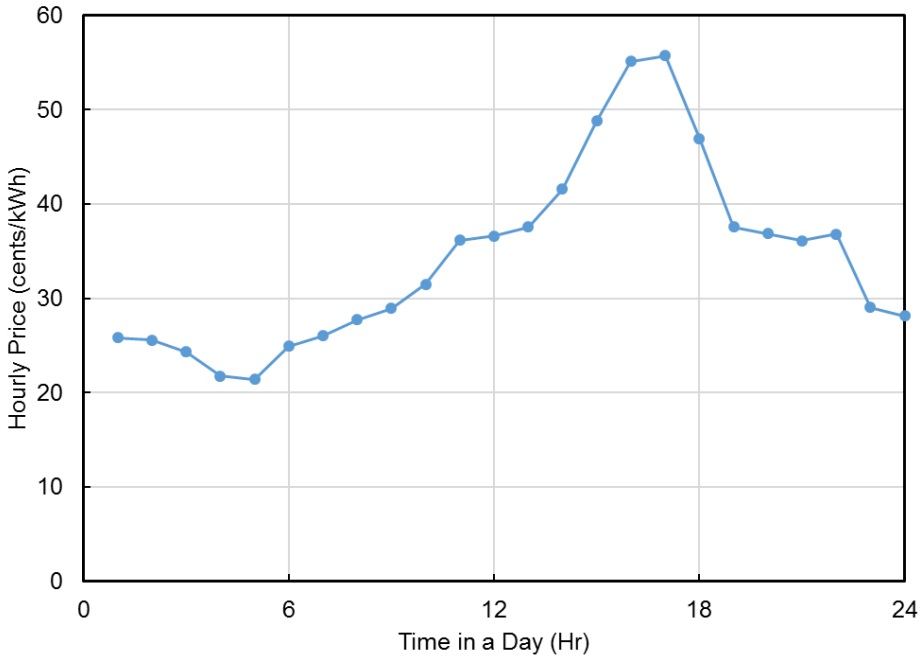

Figure 5-9 Day-ahead real-time pricing

5.2.2 Operation Scheme

The operation of the system could be illustrated in Figure 5-10, which shows the change of building cooling/heating load along with time. In Figure 5-10, it is assumed that the system is attending a day-ahead real-time program. The goal is to operate the system such that the highest EE or DR benefit could be achieved. At 6 PM of Day #0, which is also the assumed "present time", the system collects the load and cost information of Day#1. However, the operation of the TES could span across couple of days. Therefore, in order to achieve the highest benefit in Day #1, it is necessary to include the forecasted information from Day #2 as well. The time scope from Day #0 to Day #2 could be defined as a forecast window. Therefore, the target EE or DR functions are defined in the forecast window rather than the time window of Day #1. To reflect the benefit in both EE and DR domain, three target functions are used in this study:

- Energy consumption function
- Cost function
- Congestion function

The energy consumption function is from the EE domain while the congestion function is from the DR domain. Cost function is the middle ground between EE and DR. The energy consumption and congestion function are illustrated in Figure 5-11. Energy consumption is the accumulated results of system operation while congestion is the results of fluctuation of the operation. The cost function, which is similar to the energy consumption function, is shown in Figure 5-12.

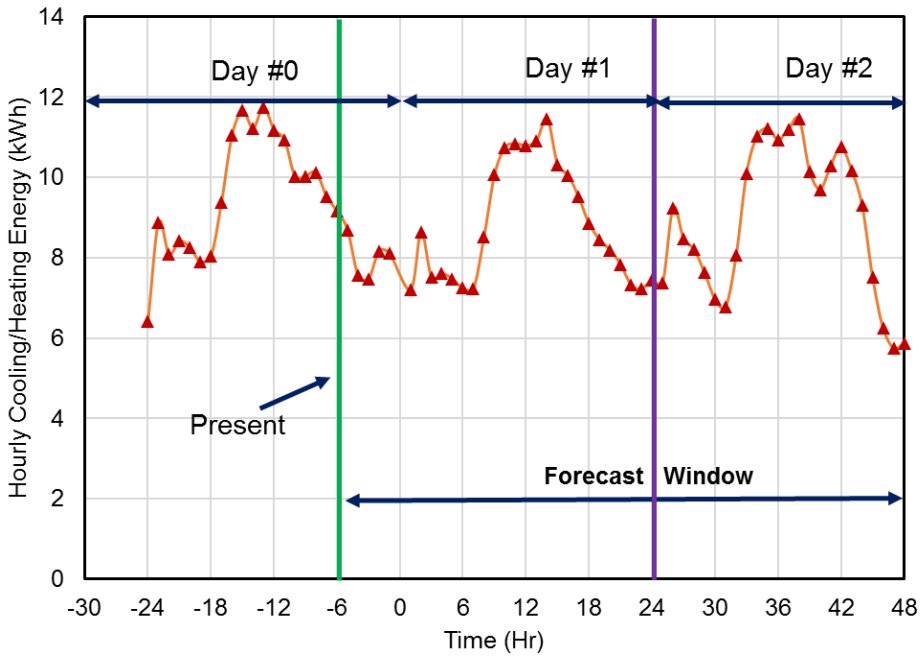

Figure 5-10 Time-wise operation illustration

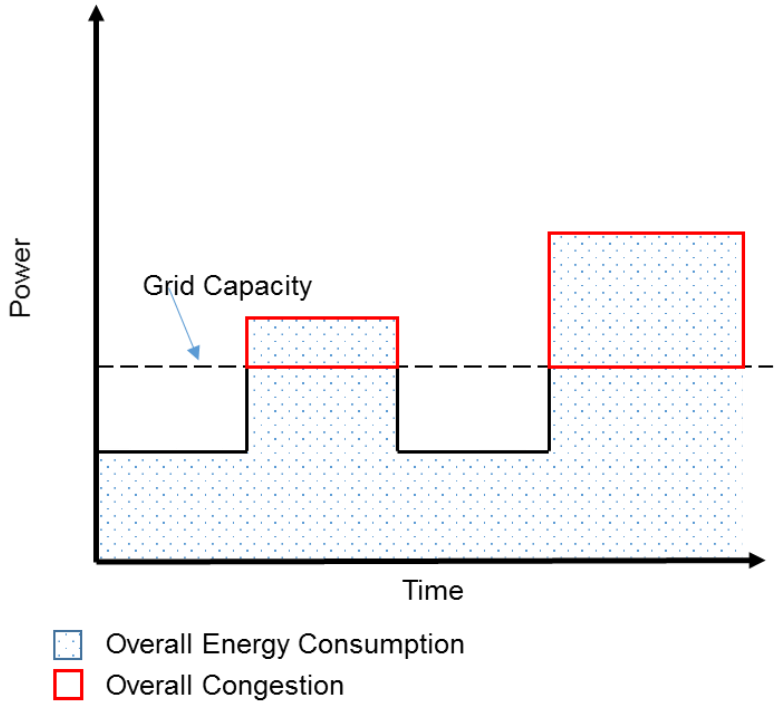

Figure 5-11 Energy consumption and congestion of operation

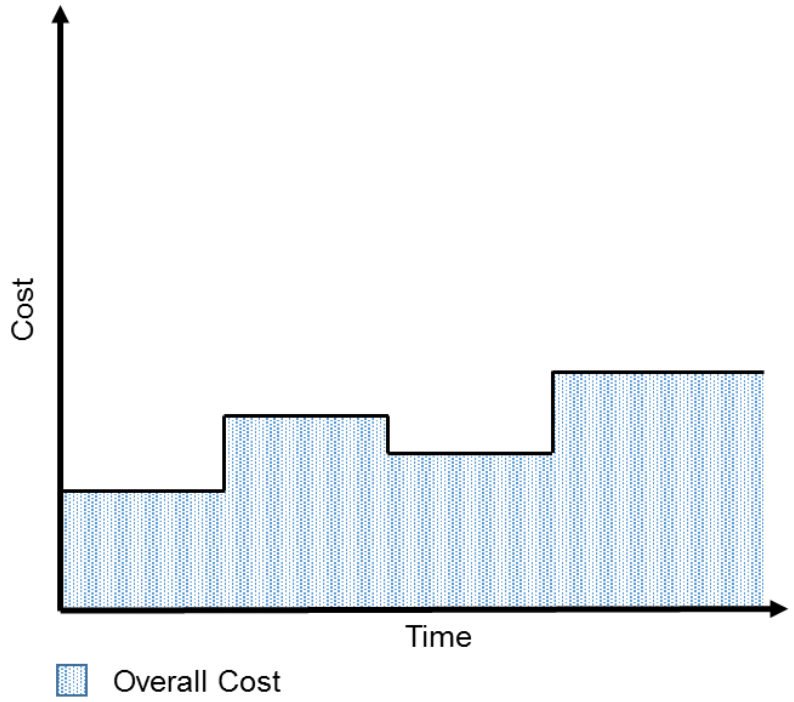

Figure 5-12 Cost of operation

The definition of three functions are shown from Equation 5-1 to Equation 5-3. Equation 5-1 and Equation 5-2 show the energy consumption and cost functions of the new VRF system with PCM based TES and the baseline system. In Equation 5-1 and Equation 5-2, n denotes the hours when TES is not active and m represents the hours with active TES. When r_i and r_j equal to unity, both equations are used to estimate the energy consumption. When r_i and r_j represent the pricing signal, both equations calculate the cost of operation. For either baseline or new VRF system with PCM based TES, Equation 5-3 is used to calculate the congestion function Ψ during the operation.

$$\Phi_{new,system} = \sum_{i=1}^{n} \frac{Q_i}{COP_i} r_i + \sum_{j=1}^{m} \frac{Q_j}{COP_j} r_j \qquad \text{Equation 5-1}$$

$$\Phi_{baseline} = \sum_{i=1}^{n+m} \frac{Q_i}{COP_i} r_i \quad \text{Equation 5-2}$$

$$\Psi = \sum_{k=1}^{n+m} (\max(\frac{Q_k}{COP_k}, \left(\frac{Q_k}{COP_k}\right)_{avg}) - \left(\frac{Q_k}{COP_k}\right)_{avg}) \quad \text{Equation 5-3}$$

5.3 Preliminary Design Month Analysis

In order to show the EE and DR potential of the new VRF system with PCM based TES, a preliminary analysis was carried out. The goal was to investigate the effect of melting point of the PCM based TES. The preliminary analysis was carried out in cooling and heating design months: July and January. It was based on the following assumptions:

- PCM based TES is an ideal cooling supply sink in cooling operation and is an ideal heat source (evaporator) for heating operation. By treating PCM as an ideal sink/source, the detailed simulation of PCM based TES is not considered.
- VRF system operates with built-in operation parameters.
- TES device operation strategy is a timing operation schedule. Therefore, the effect of different operation methods is not considered. The timing operation schedule is defined as follows:
    - Cooling season: PCM is solidified during the night time (8 PM – 7AM). It provides cooling to building during 3-hr day time peak period.
    - Heating season: PCM is melt during the day time (8 AM – 7PM). It is used as an evaporator in the 3-hr night time peak period.

Based on these assumptions, the preliminary results are shown from Figure 5-13 to Figure 5-16. Figure 5-13 and Figure 5-14 show the reduction of energy consumption

and congestion when switching from baseline VRF to the new VRF system with TES during the cooling operation. From Figure 5-13, it can be seen that a lower PCM melting temperature leads to a lower energy saving. The reason is that a lower melting temperature means the evaporating temperature of the refrigerant during the PCM solidification process shall be even lower. Therefore, the energy consumption of the new VRF system with PCM based TES decreases with a lower melting temperature. As can be seen from Figure 5-13, the energy saving potential of the new VRF system is close to 3% when the melting temperature is 4°C. Meanwhile, the cooling energy consumption difference between the solidification process and the cooling supplying process is higher, which means the system has a worse time-wise distribution of the energy consumption during the operation. Therefore, the congestion increases, as shown in Figure 5-14. The congestion increases more than 30% at a melting temperature of 4°C. However, it should also be noticed that even with a higher melting temperature, the congestion of the new VRF system with PCM based TES is still higher than the baseline system. That is due to the fact that the timing schedule operation does not consider the congestion effect. It also indicates the necessity of employing a proper operation strategy to achieve DR domain benefit.

The results in the heating operation are shown in Figure 5-15 and Figure 5-16. In the heating operation, the increase of melting temperature could result in the decrease of energy saving. The reason is that a higher melting temperature also means a higher condensing temperature during the melting process. As can be seen in Figure 5-15, when the melting temperature is 12°C, the energy saving potential is less than 5%. A higher melting temperature also leads to a worse congestion performance. As can be

seen in Figure 5-16, the congestion reduction drops to less than 20% when the melting temperature is 12°C. However, when compared to the cooling operation, the new VRF system with PCM based TES could always reduce the congestion. That is due to the fact that the heating energy consumption of the system during peak period is now lower by using the PCM as the evaporator. Therefore, the difference between the peak period and off-peak period decreases. As can be seen in Figure 5-16, the congestion could be reduced by as higher as 23% when the melting temperature is 4°C. Based on the preliminary analysis, to achieve both EE and DR benefit in cooling and heating season, the melting temperature of PCM is selected to be 8°C.

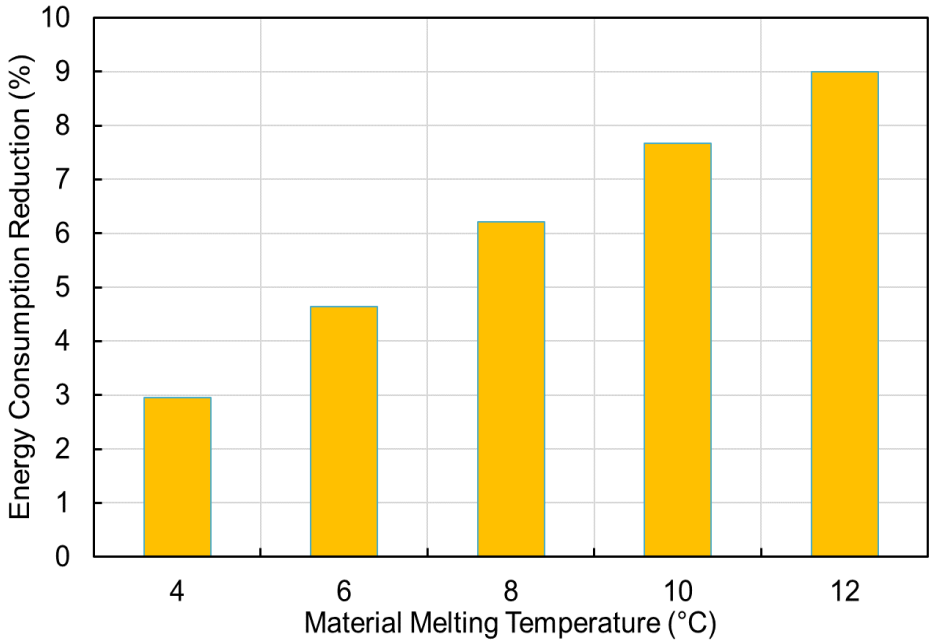

Figure 5-13 Cooling: effect of melting temperature on energy consumption reduction

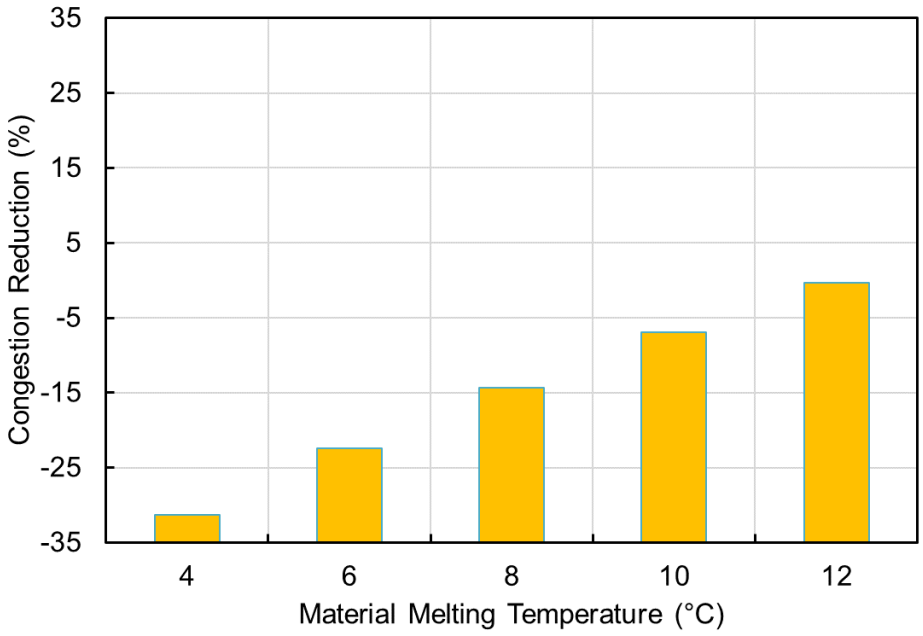

Figure 5-14 Cooling: effect of melting temperature on congestion reduction

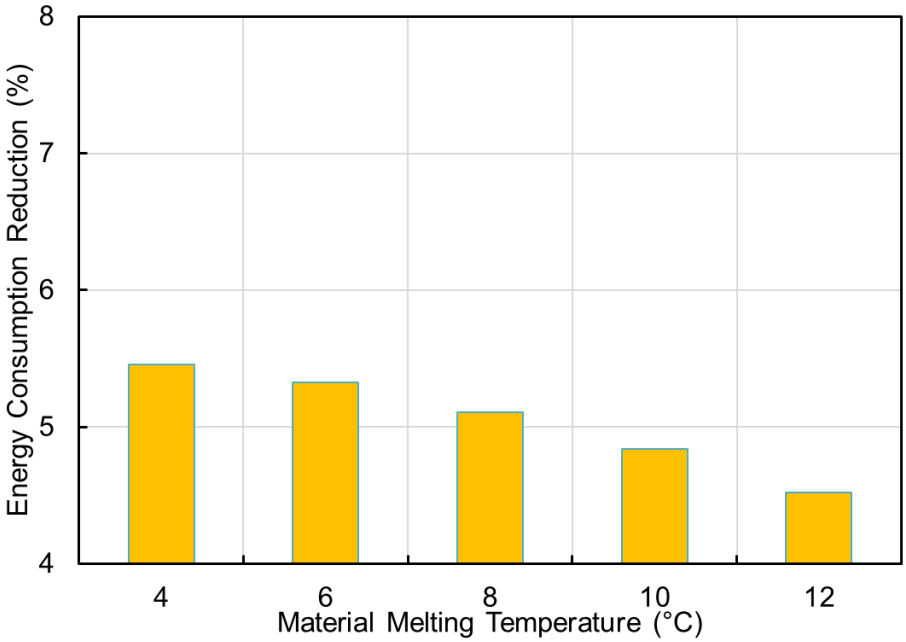

Figure 5-15 Heating: effect of melting temperature on energy consumption reduction

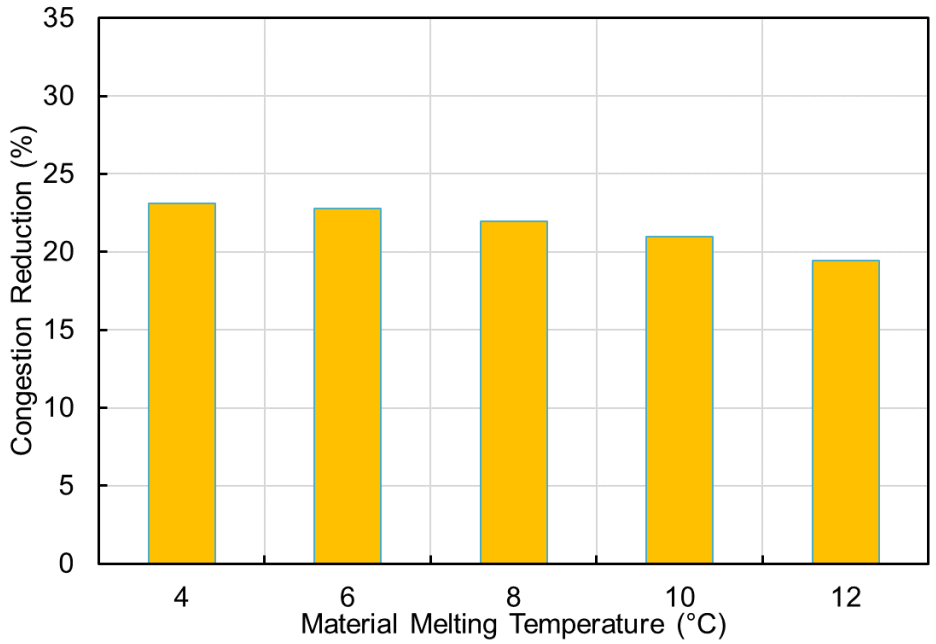

Figure 5-16 Heating: effect of melting temperature on congestion reduction

5.4 Phase Change Material Integrated Heat Exchanger

5.4.1 Phase Change Material Selection

Since the temperature of the PCM is selected to be 8°C, the next step is to select the material. Three PCMs available in the markets are compared. The results are shown in Table 5-1.

Table 5-1 PCM comparison

	RT8 HC	PureTemp8	A8
Company	RubiTherm	PureTemp	PCM Products
Melting Temperature Range (°C)	6~9 (Peak: 7)	6-10 (Peak: 8.5)	8 (Range: N/A)
Solidification Temperature Range (°C)	9~6 (Peak: 8)	10-6 (Peak: 8.5)	8 (Range: N/A)
Heat Storage Capacity (kJ/kg)	190	178	150
Specific Heat (kJ/kg-K)	2	2.15	2.16
Density (kg/m^3)	770(L)/880(S)	860(L)/950(S)	773(L)
Conductivity (W/m-K)	0.2	0.14(L)/0.22(S)	0.21
Price ($/kg)	6.2	6.6	10.0

As can be seen from Table 5-1, the three PCMs considered have a melting temperature close to 8°C. From the design perspective, it is better to have a narrow temperature range of melting and solidification. A wide temperature range could deteriorate the energy saving and DR potential of the system, as shown in Section 5.2. From the storage point of view, a higher material density and a higher energy density mean a compact system in terms of mass/volume. From heat transfer point of view, a higher conductivity also ensures a better heat transfer. If further enhancement of conductivity is needed, a widely used practice is to use graphite ($2.3/kg) to enhance the overall

conductivity. Finally, the cost of PCM is also a factor that should not be neglected. Based on all these aspects, material RT8 HC is chosen to be used in this study.

5.4.2 Phase Change Material Integrated Heat Exchanger Design

After choosing the material, the next step is to design the heat exchanger that could achieve the required melting and solidification capability in cooling and heating season. Since the cooling demand of the building is higher than heating demand, the design of PCM integrated heat exchanger is carried out based on the cooling season operation. In this study, the PCM is designed based on the analytical model of PCM solidification in cooling season.

5.4.2.1 Analytical PCM Heat Transfer Model

The analytical model of PCM heat transfer was built on the assumptions that the natural convection in the liquid phase is not significant and the primary heat transfer mode in PCM is conduction during the solidification process. The solidification of PCM outside of a tube segment could be illustrated in Figure 5-17.

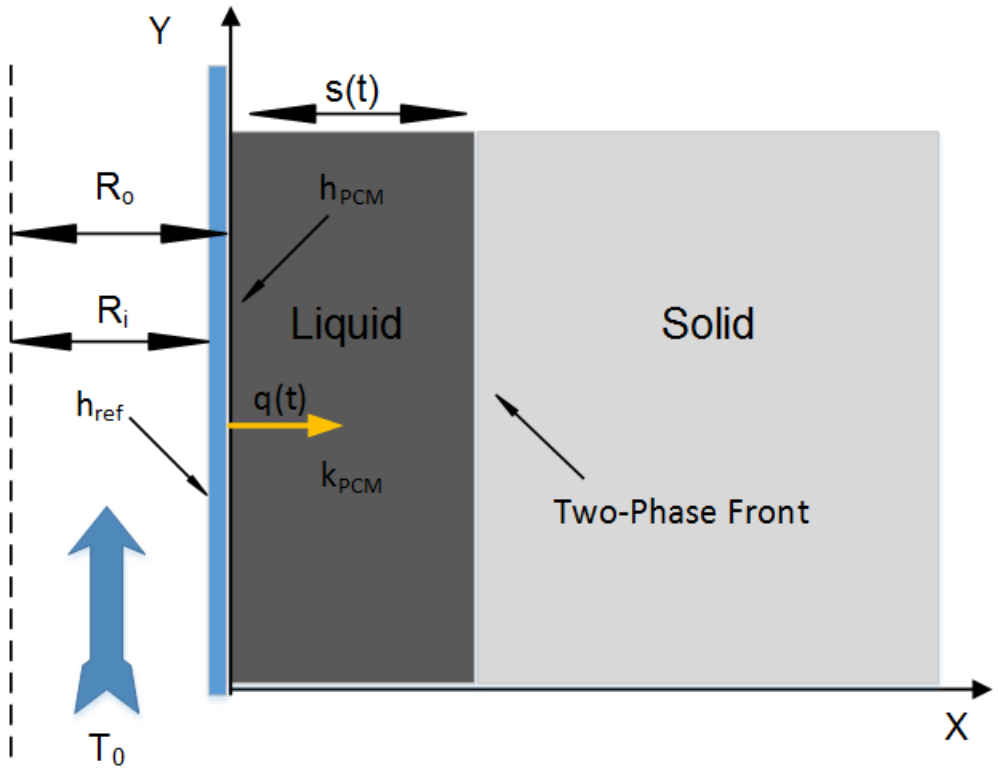

Figure 5-17 Solidification of PCM outside a tube segment

In Figure 5-17, the refrigerant flow at the inlet of the tube has a temperature of T_0. Outside the tube wall, the solid PCM is accumulated at the surface of the tube. The material temperature increases in the x axis until it reaches the two-phase front, after which the material stays in the melting temperature (Ts). From the aspect of melting, the heat flux released by PCM with the movement of two-phase front could be could be represented in the following equation:

$$\dot{q}(t) = 2\pi(R_0 + s(t))\rho_s \Delta h \frac{ds(t)}{dt} \qquad \text{Equation 5-4}$$

Where $s(t)$ is the distance the two-phase front has travelled.

Meanwhile, from the aspect of heat transfer, the heat flux could also be represented in the following heat transfer equation. In Equation 5-5, the thermal resistance of the tube wall is neglected to simplify the analysis.

$$\dot{q}(t) = \frac{T_s - T_0}{\frac{\ln(\frac{R_0 + s(t)}{R_0})}{2\pi k_{PCM}} + \frac{1}{2\pi R_i h_{ref}}} \qquad \text{Equation 5-5}$$

Because of the energy balance, we can set Equation 5-4 and Equation 5-5 to be equal. It is possible to solve both equations and get the implicit solution (Baehr and Stephan 1995). The results are shown from Equations 5-6 to 5-9:

$$t = \frac{\rho L s(t)^2}{2k_{PCM}(T_s - T_0)} f(s', \beta) \qquad \text{Equation 5-6}$$

$$s' = \frac{s}{R_0} \qquad \text{Equation 5-7}$$

$$\beta = \frac{k_{PCM}}{h_{ref}(R_0 - b)} \qquad \text{Equation 5-8}$$

$$f(s', \beta) = \left(1 + \frac{1}{s'}\right)^2 \ln(1 + s') - (1 + \frac{2}{s'})(0.5 - \beta) \qquad \text{Equation 5-9}$$

Once the position of the front is determined, the solidification power could be calculated by Equation 5-4.

5.4.2.2 PCM Integrated Heat Exchanger

With the analytic model, it is possible to calculate the movement of the two-phase front and the solidification power. Therefore, the analytical model was used to design the PCM integrated heat exchanger. The design conditions are as follows:

- The solidification process lasts one hour.
- One-hour solidification removes 54,000 kJ of heat from PCM.

- The temperature difference between the T_0 and T_S is 5K.

The constraints of the design are also listed as follows:

- When filled by liquid, the mass of PCM in the heat exchanger shall be enough to allow a total amount of 54,000 kJ latent heat to be removed.
- The two-phase front should stay within the PCM material to avoid subcooling.

To reduce the volume of the PCM heat exchanger, it is necessary to consider enhancing heat transfer areas using fins. However, the temperature on the fin surface is different from the wall temperature. In the design stage, it is assumed that temperature of the fin is the average of the wall temperature and material melting point and that the efficiency of fin is 0.5. With the introduction of fins, the analytical model of finned tube could be treated similar as a cylinder tube by replacing k_{PCM} with $k_{PCM} * F_{design}$. F_{design} is calculated in Equation 5-10.

$$F_{design} = \frac{A_b + 0.5A_f}{A_t} \qquad \text{Equation 5-10}$$

The design parameters involved in this study include:

- Number of tube banks
- Number of tube rows per bank
- Tube outer diameter
- Tube thickness
- Fin length
- Fin thickness
- Fin density (FPI)
- Vertical tube spacing

- Horizontal tube spacing
- PCM conductivity enhance techniques such as copper sponge or graphite matrix

Based on the analytic model and the constraints, this study selected a set of design parameters, as listed in Table 5-2. Overall, three PCM integrated heat exchangers are used to cover three consecutive hours in cooling season. The designed PCM integrated heat exchanger is illustrated in Figure 5-18. In the cooling season, the entire tank is used. However, in the heating season, due to the lower heating demand, only half of the tank is used.

Table 5-2 Designed PCM integrated heat exchanger

	PCM based TES
Number of tube banks	6
Number of tube rows per bank	6
Width (m)	0.96
Height (m)	0.96
Depth (m)	0.7
Tube length (m)	0.6
Vertical tube spacing (m)	0.16
Horizontal tube spacing (m)	0.16
Tube outer radius R_0 (m)	$6.3e^{-3}$
Tube inner radius R_i (m)	$5.5e^{-3}$
Fin length l_f (m)	0.002
Fin thickness δ (m)	$1.4e^{-4}$
Fin density N (FPI)	25
Fin spacing l_c (m)	$8.76e^{-4}$
PCM material preparation	graphite matrix structure

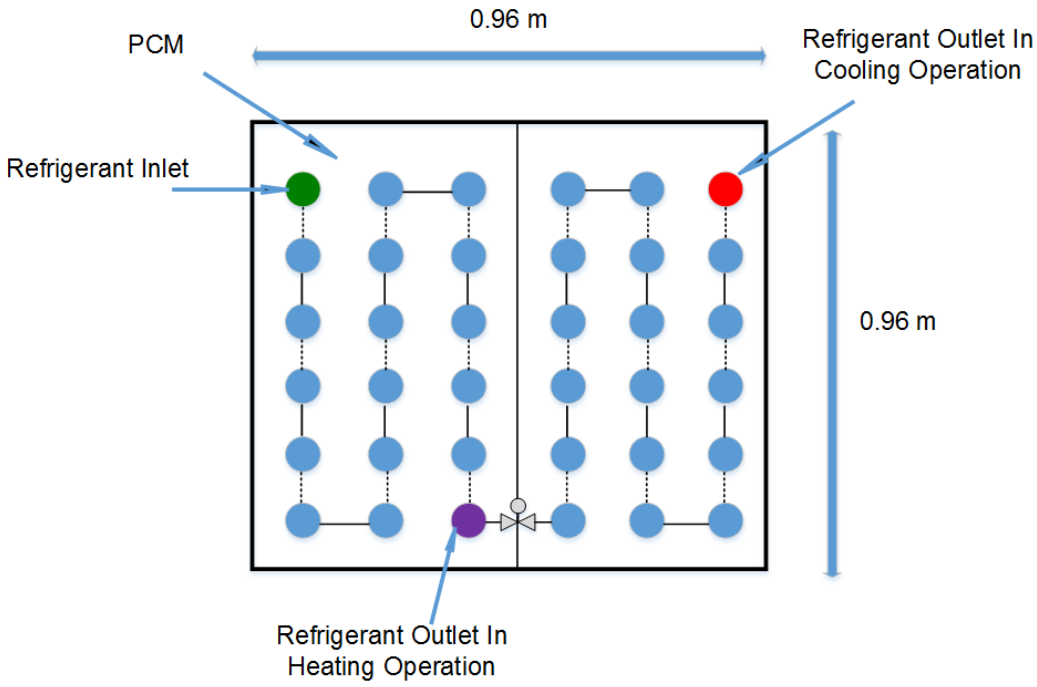

Figure 5-18 Designed PCM heat exchanger

5.4.3 Phase Change Material Integrated Heat Exchanger Simulation

5.4.3.1 Natural Convection Effect and Fin Efficiency

The PCM based TES was designed based on the analytical model of solidification process. In order to simulate the melting and solidification of designed TES in both cooling and heating season, two extra aspects should be considered: the effect of fin temperature distribution on the fin efficiency and the effect of fin on the natural convection.

As mentioned above, heat transfer area increasing techniques such as fins could increase the overall heat transfer area. However, the temperature on the fin is not the same as the base plate temperature. It is necessary to consider fin efficiency during the simulation. The heat transfer in a segment of finned tube during melting process is

shown in Figure 5-19. For the fin segment, the amount of conduction heat is shown in Equation 5-11. At the same time, the amount of heat exchanged through convection could be shown in Equation 5-12. Energy balance of the fin segment could be built as shown in Equation 5-13. When assumed adiabatic boundary condition at the end of the fin, the analytical solution of the fin temperature distribution is shown from Equation 5-14 to Equation 5-17.

$$\dot{Q}_{in} - \dot{Q}_{out} = 2\pi k_f x \delta \frac{\partial^2 T_f}{\partial x^2} \quad \text{Equation 5-11}$$

$$\dot{Q}_{conv} = 4\pi h_{PCM,mt} x (T_f - Ts) \quad \text{Equation 5-12}$$

$$\dot{Q}_{conv} = \dot{Q}_{in} - \dot{Q}_{out} \quad \text{Equation 5-13}$$

$$\frac{T_f - T_s}{T_w - T_s} = \frac{I_0(mx)K_1(mx_2) + I_1(mx_2)K_0(mx)}{I_0(mx_1)K_1(mx_2) + I_1(mx_2)K_0(mx_1)} \quad \text{Equation 5-14}$$

$$m = \sqrt{\frac{2h_{PCM,mt}}{k_f \delta}} \quad \text{Equation 5-15}$$

$$x_1 = R_0 \quad \text{Equation 5-16}$$

$$x_2 = R_0 + l_f \quad \text{Equation 5-17}$$

Based on the temperature distribution, the overall and single fin efficiency could be calculated by Equation 5-18 and Equation 5-19.

$$\eta_{fin} = 1 - \frac{NA_f}{A_t}(1 - \eta_{fs}) \quad \text{Equation 5-18}$$

$$\eta_{fs} = \frac{2x_1}{m(x_2^2 - x_1^2)} \frac{I_1(mx_2)K_1(mx_1) - I_1(mx_1)K_1(mx_2)}{I_1(mx_2)K_0(mx_1) + I_0(mx_1)K_1(mx_2)} \quad \text{Equation 5-19}$$

Where η_{fin} is the overall fin efficiency and η_{fs} is the efficiency of single fin.

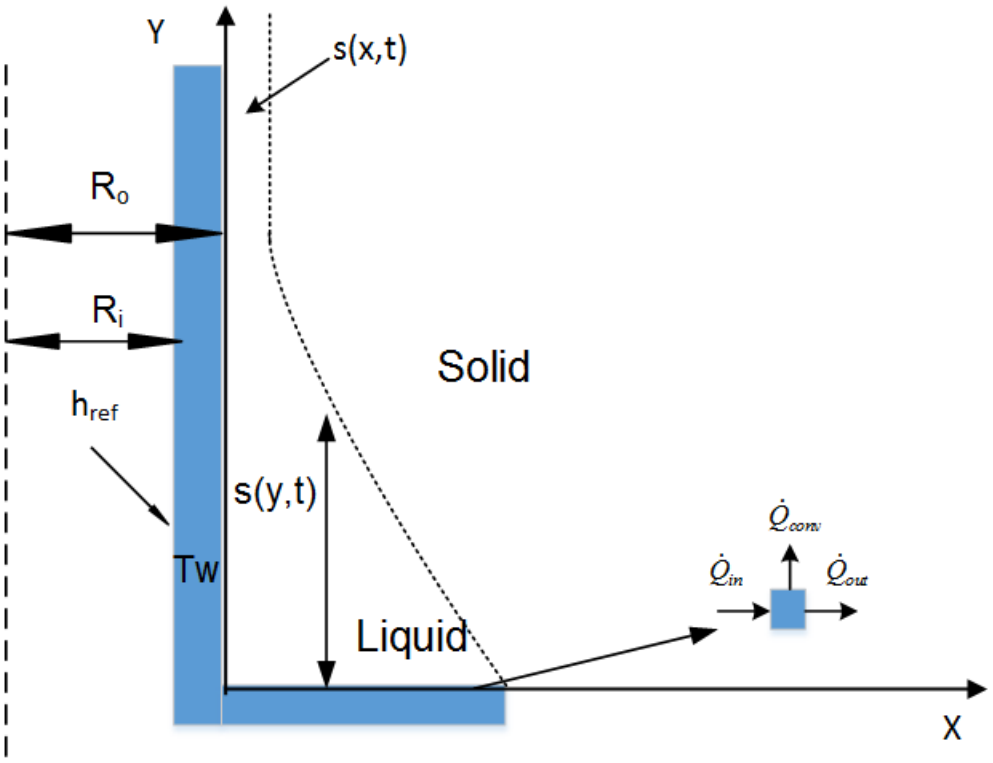

Figure 5-19 Melting process considering fin effect

As can be seen from Equation 5-14 to Equation 5-19, one key aspect of fin efficiency is the heat transfer coefficient between fin and PCM. What is known so far is that the melting process is a combination of conduction and convection. PCM near the fin surface is affected by both the buoyancy force which is caused by the density gradient of the material and the viscous force (Bergman *et al.* 2011). At the early stage of melting, the heat flux from fin surface could not generate enough density gradient that overcomes the viscous force. During that stage, conduction is the exclusive heat transfer mode. With the movement of the two-phase front, the buoyance force becomes stronger and finally takes over. The dominating heat transfer mode becomes

convection. Therefore, the key is the comparison between the buoyance force and the viscous force, which could be represented by the Rayleigh's number (Ra).

From Figure 5-19, the Rayleigh's number could be defined based on the accumulated thickness of PCM that covers the fin segments, as shown in Equation 5-20.

$$Ra = \frac{g(T_f - T_s)\rho_{PCM}^2 C_p S(y,t)^3 \beta_v}{\mu k_{PCM}} \quad \text{Equation 5-20}$$

The transition of heat transfer mode from conduction to convection happens when Ra is higher than a critical value, which is 1708 (Lamberg and Sirén 2017). Therefore, it is possible to derive the critical PCM layer thickness from the Equation 5-21.

$$s(y,t)_{cr} = \left(\frac{1708\mu k_{PCM}}{\beta_v(T_f - T_s)\rho^2 C_p}\right)^{\frac{1}{3}} \quad \text{Equation 5-21}$$

When the thickness of PCM liquid layer is greater than the critical thickness, the convection dominates the heat transfer. From Equation 5-20, it can be seen that a higher temperature difference and a lower conductivity will leads to an earlier transition from conduction to convection. On the contrary, with a higher PCM conductivity, the effect of conduction is strong. It also means that the two-phase front needs to move a further distance before the convection could take over. In the finned tube heat exchanger, the distance the front could move away from the fin surface is limited by the spacing between the fins. Therefore, the fins could impede the transition from conduction to convection. For example, when the temperature difference between the fin and PCM is 45 K and the conductivity of PCM is 0.2 W/m^2-K, the critical thickness is 0.0024 m. Accordingly, the convection becomes dominating only when the fin density is lower than 10 FPI. Once convection becomes the dominating heat transfer mode, the

convection heat transfer coefficient could be calculated by Equation 5-22 and Equation 5-23 (Marshall R 1979; Bergman *et al.* 2011).

$$Nu = 0.072\, Ra^{\frac{1}{3}} \qquad \text{Equation 5-22}$$

$$Nu = \frac{h_{PCM,conv} s(y,t)}{k_{PCM}} \qquad \text{Equation 5-23}$$

What needs to be pointed out is that when substituting Equation 5-20 into Equation 5-21 and 5-22, it could be found that the convection heat transfer coefficient is independent of time and position. It depends on the physical properties of the PCM and the temperature difference between the fin and the PCM. Eftekhar *et al.* (1984) found that when compared to the physical properties of the PCM, the effect of fin temperature is also small. Therefore, in this study, the convection heat transfer coefficient is calculated based on the mean temperature of refrigerant inlet and the PCM melting point. The properties of the liquid PCM are listed in Table 5-3. If convection is the dominating form of heat transfer, the natural convection heat transfer coefficient ($h_{PCM,conv}$) is found to be 56.1 W/m^2-K.

Table 5-3 Material properties

	PCM
Viscosity (μ)	0.02 kg/m-S
Volumetric Expansion Coefficient (β_v)	0.0001 K^{-1}
Density (ρ)	770 kg/m^3
Specific heat (C_p)	0.2 kJ/kg-K
PCM material preparation	graphite matrix structure

To simplify the analysis, it is necessary to introduce an equivalent heat transfer coefficient to consider both conduction and convection heat transfer. The equivalent heat transfer coefficient is shown in Equation 5-24. The introduction of equivalent heat transfer coefficient allows a similar analysis of fin efficiency in both melting and solidification process.

$$h_{eqv} = \frac{k_{PCM}}{l_c} \quad \text{Equation 5-24}$$

Meanwhile, based on the melting process analysis, the overall heat transfer coefficient in the melting process could be calculated by Equations 5-25 and 5-26:

$h_{PCM,mt} = h_{eqv}$ when Ra < 1708 Equation 5-25

$h_{PCM,mt} = h_{PCM,conv}$ when Ra > 1708 Equation 5-26

Now, it is possible to layout the fin efficiency in both melting and solidification process with the heat transfer coefficient given from Equations 5-24 to 5-26. The calculated fin efficiency is listed in the following table:

Table 5-4 Fin efficiency

	Overall Fin Efficiency
Melting: Convection Dominating	0.99
Melting: Conduction Dominating	0.56
Solidification	0.56

Due to the low heat transfer coefficient in the natural convection, the effect of natural convection on the fin temperature distribution is not significant. Therefore, the fin temperature is close to the wall temperature and the fin efficiency is close to one.

However, the space between fins is small, which leads to a low conduction thermal resistance. When conduction is the dominating effect in either solidification or melting process, the fin temperature drops rapidly along with the fin length, which leads to a lower fin efficiency. To show the decay of fin temperature, two non-dimensional values are defined in Equations 5-27 and 5-28:

$$x_{norm} = \frac{x+R}{l_f+R} \text{ w} \qquad \text{Equation 5-27}$$

$$\theta = \frac{|T_f - T_s|}{|T_w - T_s|} \qquad \text{Equation 5-28}$$

Where x_{norm} is normalized fin length and θ is the normalized temperature difference between fin and PCM.

The decay of fin temperature is shown in Figure 5-20. As can be seen, the fin temperature decays along with the fin direction due to the high heat flux of conduction. Overall, the average fin temperature during the conduction is close to the mean of wall

temperature and PCM melting point, which also justifies the assumptions used during the design stage of PCM integrated heat exchanger.

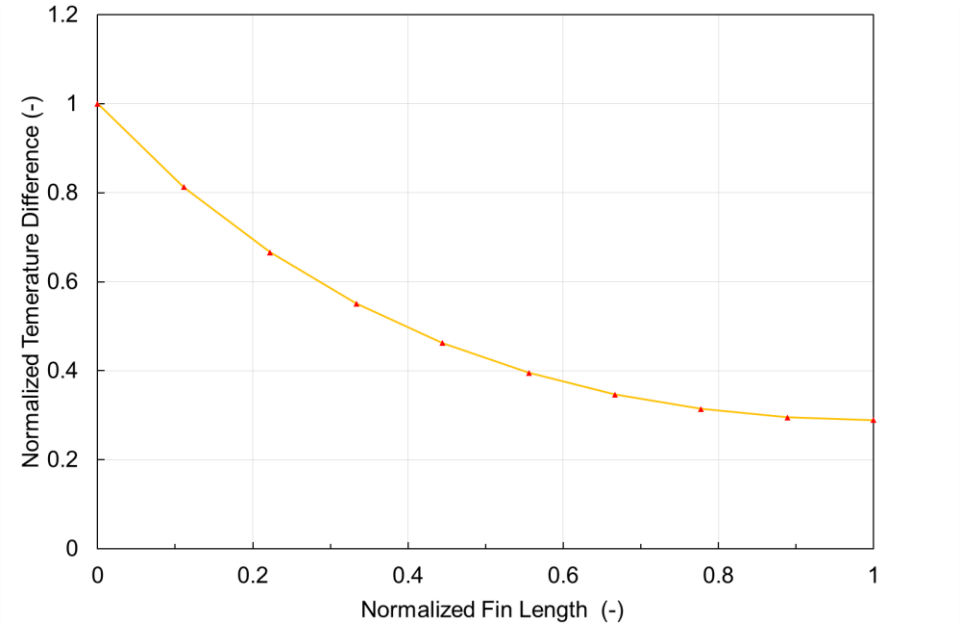

Figure 5-20 Fin temperature decay

5.4.3.2 Formulation

Based on the above analysis, it is possible to create a semi-analytical model to calculate the melting and solidification process in the designed heat exchanger. The model is illustrated in Figure 5-21. At j_{th} time step, the governing equation of the i_{th} segment could be formulated from Equation 5-29 to Equation 5-34. In this study, the time step selected is one second and one tube is divided into ten segments.

$$\dot{Q}_{i,j} = \frac{|T_{i,j-1} - T_s|}{R_{ref,i,j} + R_{PCM,i,j}} \qquad \text{Equation 5-29}$$

$$R_{ref,i,j} = \frac{1}{h_{ref} 2\pi R_i \Delta x} \qquad \text{Equation 5-30}$$

$$Convection: R_{PCM,conv} = \frac{1}{\eta_{fin} h_{PCM,conv} A_t \Delta x} \quad \text{Equation 5-31}$$

$$Conduction: R_{PCM,cond} = \frac{\ln(\frac{R+y_{i,j-1}}{R})}{2\pi F k_{PCM} \Delta x} \quad \text{Equation 5-32}$$

$$R_{PCM,i,j} = \frac{1}{\frac{1}{R_{PCM,cond}} + \frac{1}{R_{PCM,conv}}} \quad \text{Equation 5-33}$$

$$F = \frac{A_b + \eta_{fin} A_f}{A_t} \quad \text{Equation 5-34}$$

In solidification model, Equation 5-31 is neglected since it is assumed that conduction is the only mode of heat transfer. In the melting process, it is still necessary to take a look at the thermal resistance terms. As mentioned before, the convection heat transfer coefficient is independent of time or position. Therefore, it is possible to compare thermal resistance terms to quantify the dominating mode of heat transfer in the melting process. Based on the given PCM integrated heat exchanger specifications and Equation 5-30, the thermal resistance caused by convection in unit tube length is found to be 0.08 K/W. As to the conduction thermal resistance, it increases with the increases of liquid PCM layer thickness. Theoretically, the maximal conduction thermal resistance happens when the space between two neighboring tubes is occupied by the liquid PCM. The maximal conduction thermal resistance is therefore found to be 0.006 K/W. Due to the big difference between the conduction and convection thermal resistance terms, Equation 5-33 is close to the conduction thermal resistance. Therefore, the convection thermal resistance term in Equation 5-33 could be neglected in the melting calculation.

From the view of energy balance, the following equations could be formulated during the heat transfer process:

$$y_{i,j} = \sqrt{\frac{\dot{Q}_{i,j}\Delta t}{\Delta h_{PCM}\rho\pi\Delta x} + y_{i,j-1}^2} \qquad \text{Equation 5-35}$$

$$Melting: \dot{h}_{i,j} = h_{i-1,j} - \frac{\dot{Q}_{i,j}}{\dot{m}} \qquad \text{Equation 5-36}$$

$$Solidification: \dot{h}_{i,j} = h_{i-1,j} \pm \frac{\dot{Q}_{i,j}}{\dot{m}} \qquad \text{Equation 5-37}$$

Where $y_{i,j}$ is the position of phase separation and $\dot{h}_{i,j}$ is the specific enthalpy of the refrigerant flow. In the refrigerant side, the correlations used to calculate heat transfer coefficients are listed in Table 5-5.

Table 5-5 Refrigerant side heat transfer coefficient calculation

	Heat transfer coefficient correlation
Liquid phase refrigerant	Dittus and Boelter 1985
Two-phase refrigerant in boiling	Jung *et al.* 1989
Two-phase refrigerant in condensation	Shah 2013
Vapor phase refrigerant	Dittus and Boelter 1985

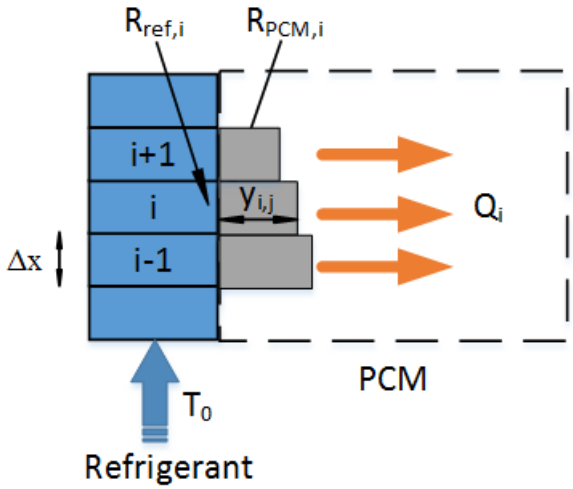

Figure 5-21 Segment heat transfer calculation

5.4.3.3 Solidification and Melting

With the semi-analytical model formulated from Equation 5-28 to Equation 5-37, the hourly melting and solidification in both cooling and heating operation could be simulated. The results are shown from Figure 5-22 to Figure 5-25. As can be seen, at the beginning, TES has the highest solidification/melting power due to the fact that the thickness of the layer is low and the thermal resistance is low. With the movement of the melting/solidification front, the thickness of PCM increases and the thermal resistance also increases. In average, the hourly melting and solidification power in both cooling and heating operation are shown in Table 5-6. It can also be seen that the solidification performance meets the design conditions.

Table 5-6 Hourly average melting/solidification power

	Average power in 3600s (kW)
Cooling: Solidification	15.7
Cooling: Melting	13.7
Heating: Solidification	7.8
Heating: Melting	8.4

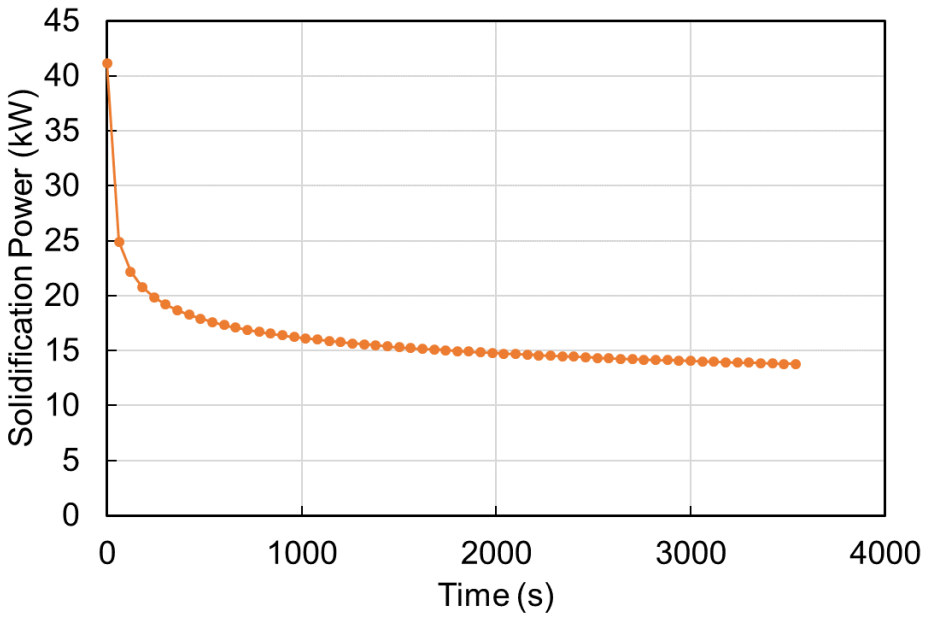

Figure 5-22 Cooling operation: hourly PCM solidification

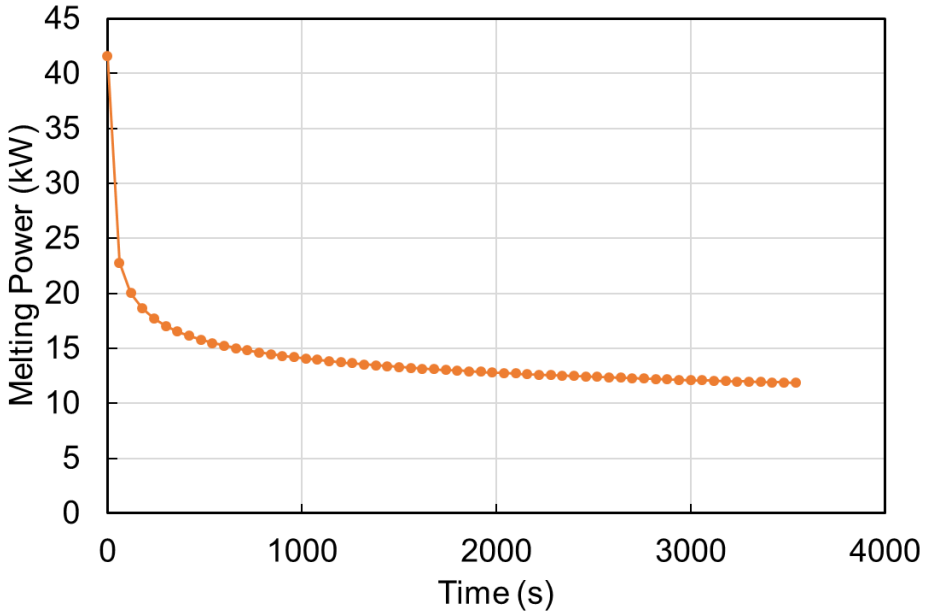

Figure 5-23 Cooling operation: hourly PCM melting

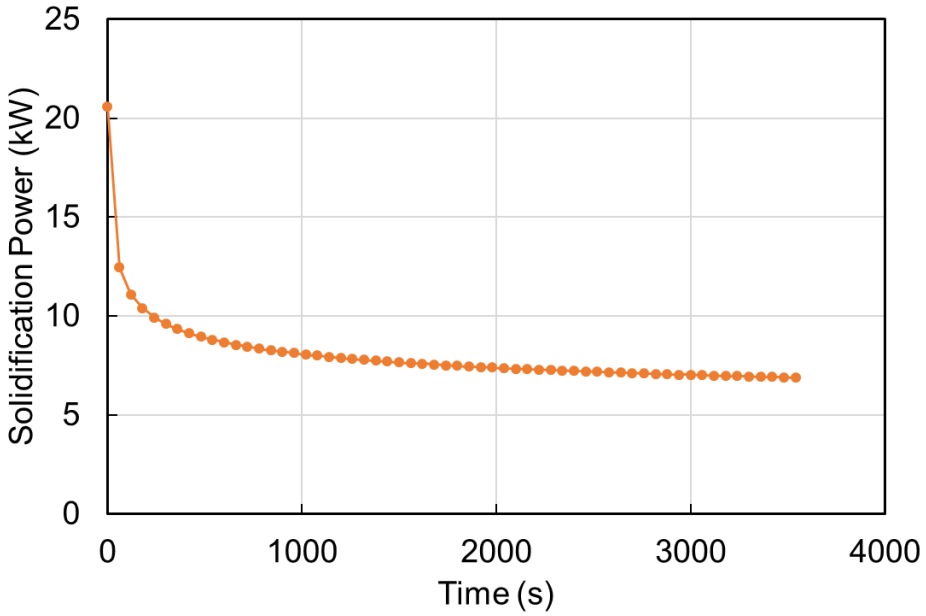

Figure 5-24 Heating operation: hourly PCM solidification

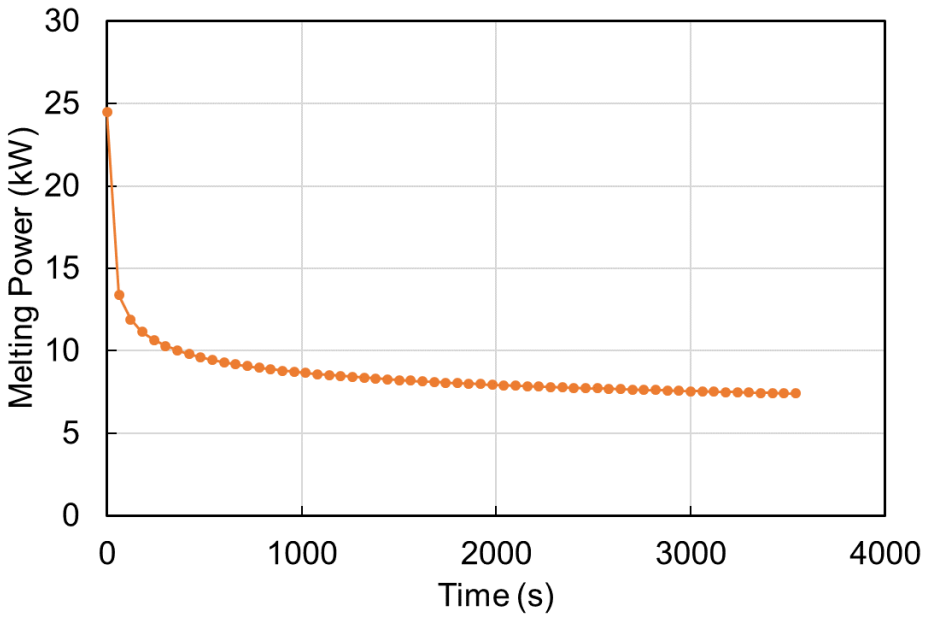

Figure 5-25 Heating operation: hourly PCM melting

5.4.4 Modeling Flowchart

With the development of PCM melting/solidification performance, it is necessary to overhaul the modeling flowchart to include such features. The change of overall calculation flowchart is shown in Figure 5-26. As can been seen, when compared to the baseline VRF system, two more steps are added in the new VRF system: operation sequence generation and PCM solidification/melting. At the beginning of the simulation of both systems, the models collect the building information and the weather data before it estimates the building space cooling, space heating and water heating load. In the baseline VRF model, as shown in Figure 5-26(a), a thermodynamic law based model is used to calculate the energy consumption of the model until the capacity of the system match with the building. However, in the new VRF model, as shown in Figure 5-26(b), the collected load information is used to estimate and generate an

operation sequence for the system. After the operation sequence is generated, PCM solidification/melting model is used to find out the status change of the PCM during the charging and discharging hours. In the new VRF system model, the thermodynamic model is used only after finishing collecting the information from both PCM and the building. The generation of the operation sequence of system in a day-ahead pricing market could be illustrated in Figure 5-27. The scheduled operation is shown in Figure 5-27(a) and the optimization-based operation is shown in Figure 5-27(b). In the schedule operation, at the end of the Nth day, the system collects the information of pricing at the (N+1)th day. Then it collects the estimated building load information of the (N+1)th day and also predicts the pricing information of the (N+2)th day. Since it is a scheduled operation, it selects the feasible operation hours for the system based on the preference such as energy saving or cost reduction. For example, in a pricing signal based cooling operation, scheduled method generates a charging sequence that occupies a certain period of time during which the grid gives the lowest prices. For the optimization-based method, as shown in Figure 5-27(b), it also predicts the load information and the pricing information. However, instead of using explicit sequence generation, the model seeks a charging/discharging schedule that could minimize the target function in the entire scope of the prediction window. The function could be related to either EE or DR domain. After the operation sequence is generated, the solidification/melting model performance illustrated in 5.4.3 is used to find out the status change of the PCM during the operation.

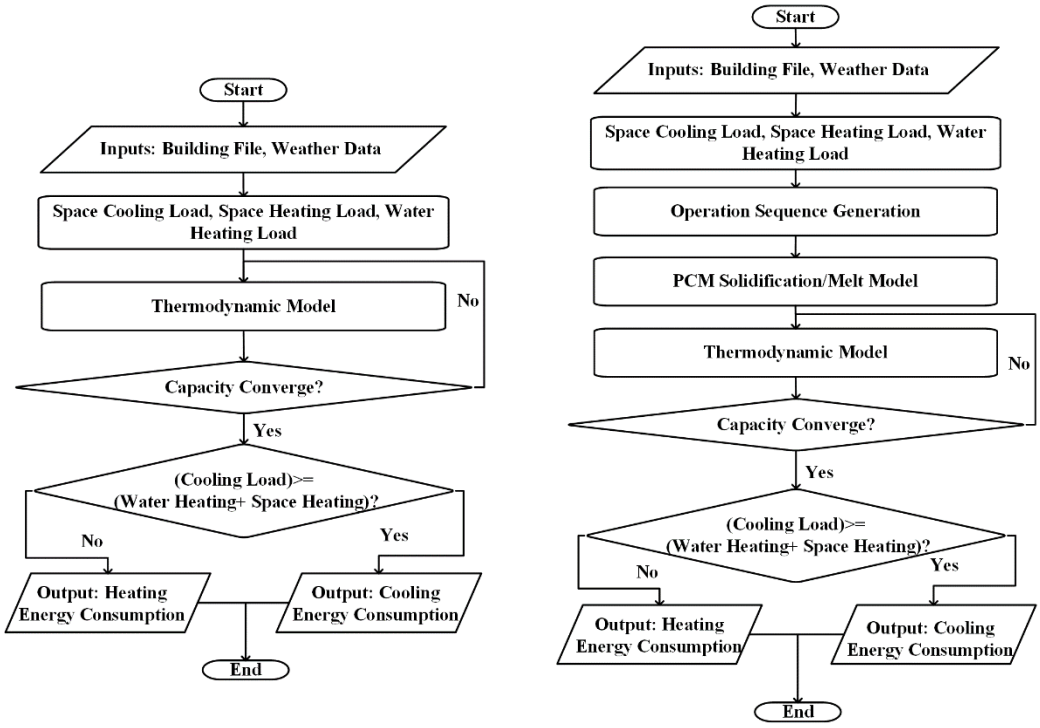

(a) VRF model without PCM based TES

(b) VRF Model with PCM based TES

Figure 5-26 Model flowchart change of VRF with PCM based TES

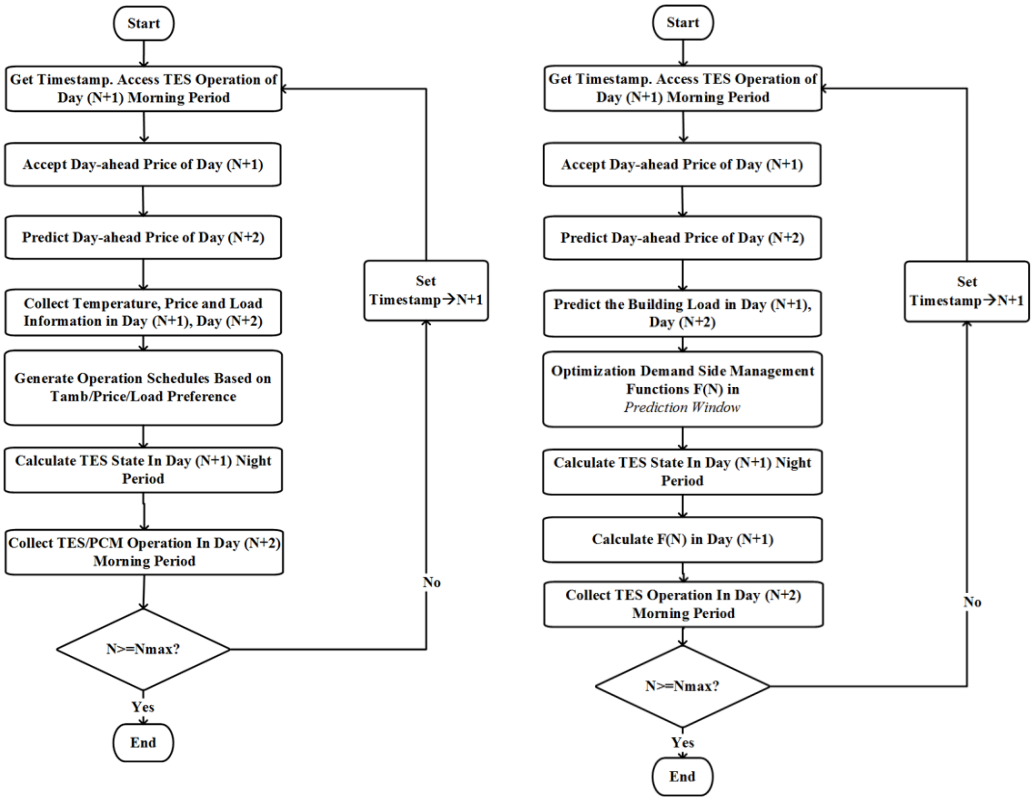

(c) Generation method with scheduled approach

(d) Generation method with optimization approach

Figure 5-27 Operation sequence generation method

5.5 Results and Discussion

5.5.1 Design Month Performance

The performance of the proposed new VRF system with PCM based TES was simulated in Baltimore, Maryland. The running period was selected to be July and January, which are also the design months for the system. To show the design month performance, the optimization-based operation sequence generation was used and the target was set to reduce the energy consumption.

5.5.1.1 Daily Performance

The energy consumption comparison between new VRF system with PCM based TES and the baseline system in a 24-hr cooling operation is shown in Figure 5-28. As can be seen, the energy consumption of the new VRF system with PCM based TES is higher than baseline system during the PCM charging period, which is in the early morning before 9 AM. It is due to the fact that the cooling load of system is increased by the solidification requirement of PCM based TES. During the peak period, which is from 4 PM to 6 PM in Figure 5-28, the cooling is provided by the melting process of PCM based TES. Therefore, the compressor is turned off and the power of the system is reduced to 300 W. Since the operation of PCM based TES could span across couple of days, the change of solid mass fraction in PCM based TES during a period of 48 hours is also shown in in Figure 5-29. It can be found from Figure 5-29 that the solid mass fraction of all three PCM tanks increases in the early morning due to the solidification process. Accordingly, the solid mass fraction drops during the peak period where the refrigerant is cooled down by the PCM based TES.

Similarly, the hourly heating operation is shown in Figure 5-30 and Figure 5-31. In Figure 5-30, the energy consumption of the system decreases due to the fact that the system is using the PCM based TES as evaporator. This could also be seen from Figure 5-31 that the PCM is solidified from 24^{th} hour to the 28^{th} hour. In Figure 5-31, the power of the new VRF system with PCM based TES increases in the afternoon due to the fact that the melting of PCM adds more heating load to the system, as shown by the solid mass fraction decrease from 39^{th} hour to the 42^{nd} hour in Figure 5-31.

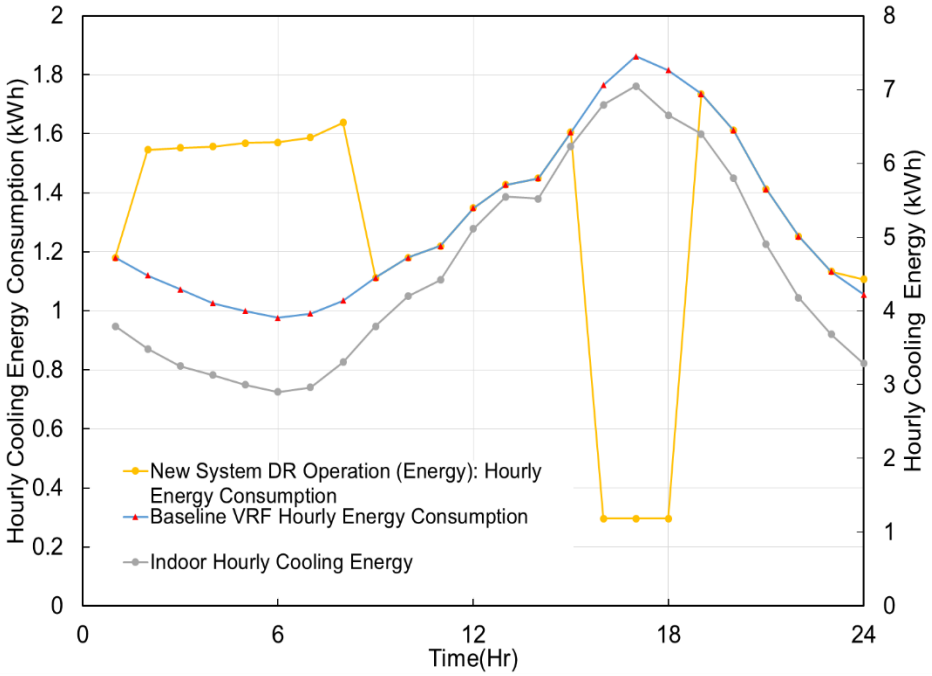

Figure 5-28 Cooling: typical 24-hr energy consumption of new VRF system

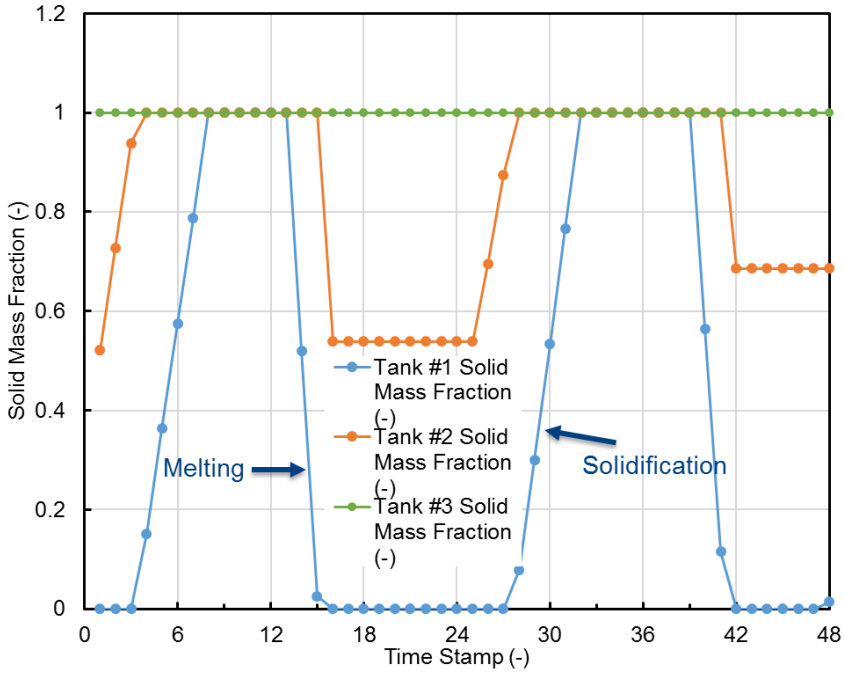

Figure 5-29 Cooling: typical 24-hr status of PCM based TES

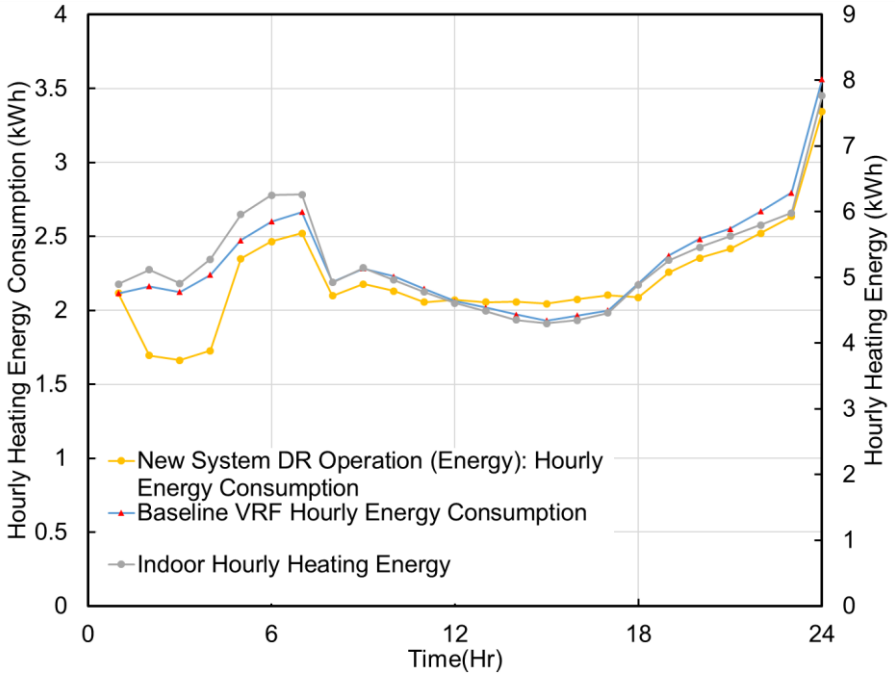

Figure 5-30 Heating: typical 24-hr performance of new VRF system

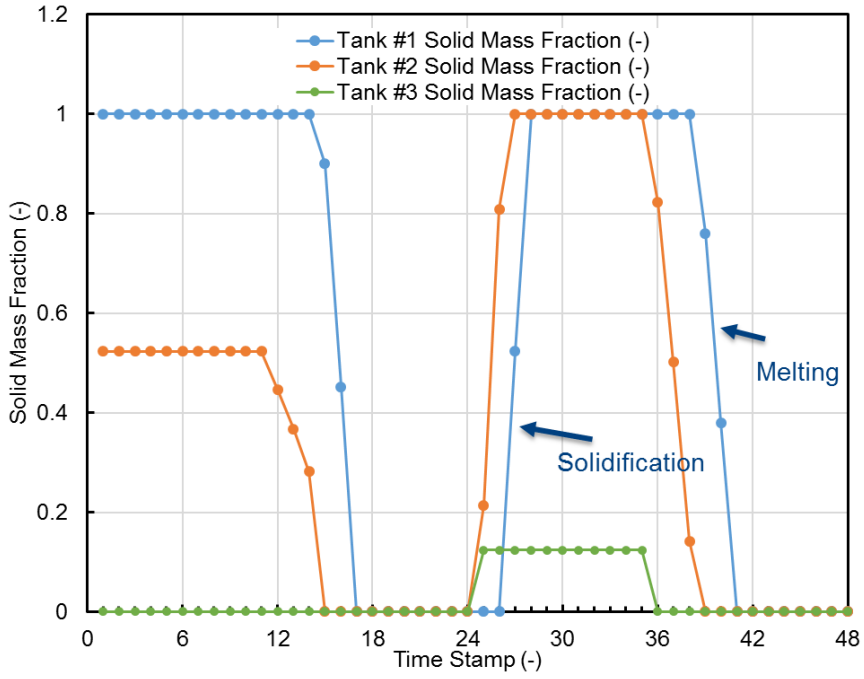

Figure 5-31 Heating: typical 24-hr status of PCM based TES

5.5.1.2 Design Month Analysis

To compare the performance of the new VRF system to that of the baseline system, the COP of cooling and heating operation is defined in Equations 5-38 and 5-39. In both equations, the cooling/heating requirement from the PCM based TES is also considered as part of the overall cooling/heating demand imposed to the VRF system.

$$COP_{cooling} = \frac{\dot{Q}_{\text{room,cooling}} + \dot{Q}_{TES}}{\text{Power}} \qquad \text{Equation 5-38}$$

$$COP_{cooling} = \frac{\dot{Q}_{\text{room,heating}} + \dot{Q}_{TES}}{\text{Power}} \qquad \text{Equation 5-39}$$

The changes of hourly cooling and heating COPs along with the increase of ambient temperature of both the new VRF system with PCM based TES and the baseline system are shown in Figure 5-32 and Figure 5-33, respectivetly. During the cooling operation, as shown in Figure 5-32, the result could be sorted into three regions. In region #1, new VRF system with PCM based TES does not operate PCM based TES. Therefore, the change of hourly performance is essentially the same as the baseline system. In region #2, where the system solidifies the PCM based TES during the low-temperature early morning hours, the COP of the system increases due to the fact that the part load ratio of the system increases. Region #3 is where the new VRF system with PCM based TES is using PCM based TES to provide cooling to the rooms. Since the pump power is much lower than the compressor power, the COP during the PCM melting hours is much higher (~22) and not shown in Figure 5-32. Overall, in the cooling design month, the energy consumption is reduced from 1,155 kWh to 1,081 kWh, which is an energy saving of 6.5%. Similarly, the performance comparison in Figure 5-33 could also be sorted into three regions. In region #1, the PCM based TES is not activated and the

performance of the new VRF system with PCM based TES overlaps with that of the baseline system. When ambient temperature is lower than 0°C, the system has performance degradation due to the defrosting operation. When ambient temperature is as high as 15°C, the performance is also low due to the low part load ratio of the system. After introducing the PCM based TES operation, the new VRF system with PCM based TES has a higher COP in region #2 and #3. In region #2, the reason behind the performance enhancement is the increase of evaporating temperature due to the fact that the melting temperature of PCM is 8°C. In region #3, the PCM is melt by the refrigerant. As a consequence, the overall heating demand increases, which improves the part load ratio of the system. Overall the monthly energy consumption is reduced from 1,772 kWh to 1,612 kWh. The energy saving is 9%, of which region #2 contributes 6.7%.

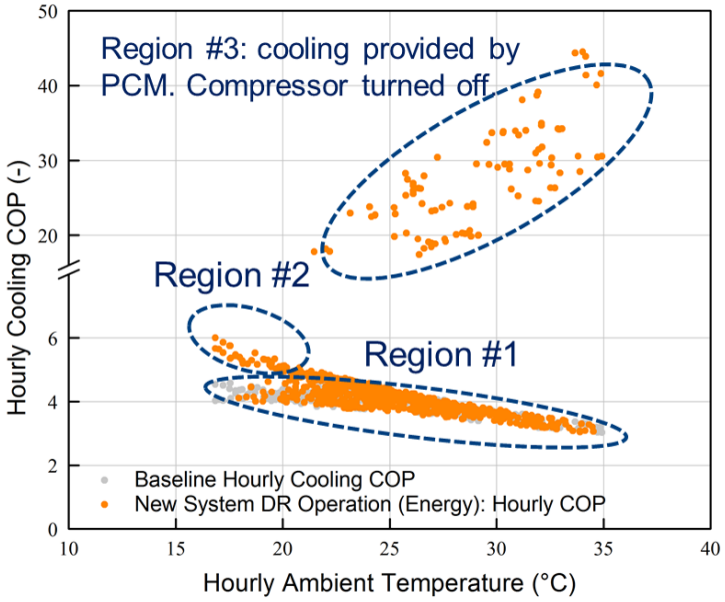

Figure 5-32 Cooling: hourly COP comparison between new system and baseline system

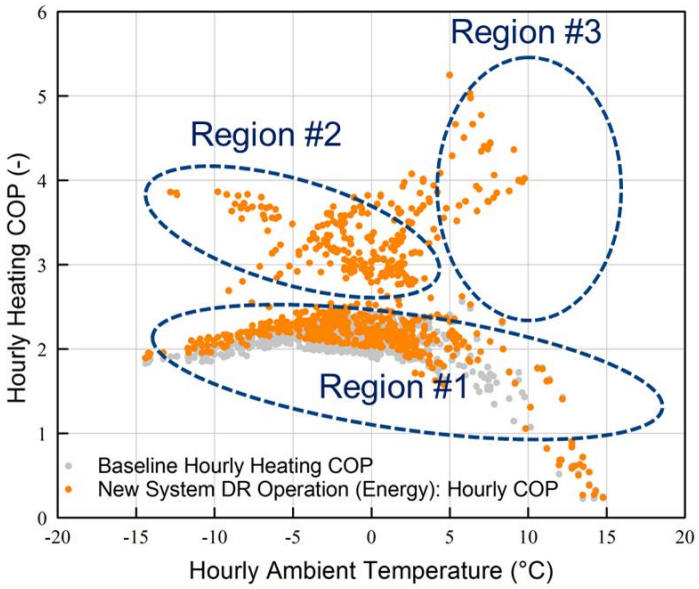

Figure 5-33 Heating: hourly COP comparison between new system and baseline system

5.5.1.3 Effect of Operation Strategy

The new VRF system with PCM based TES could respond to both EE and DR goals by the change of operation sequence based on different target functions. As mentioned before, there are different operation sequence generation methods. Therefore, it is necessary to consider the effect of these methods on the performance of the system. In this study, three methods of operation sequence generation methods were considered: the scheduled operation based on ambient temperature, the scheduled operation based on pricing information and the optimization-based method. The results of the cooling season are shown from Figure 5-34 to Figure 5-36. The results of the heating season are shown from Figure 5-37 to Figure 5-39.

In the cooling season, when the goal is to reduce the energy consumption of the system, the difference between three operation methods is relatively small, as shown in Figure 5-34. Because the cost is closely related to the overall energy consumption, the cost reductions of three methods are also close, as shown in Figure 5-35. Overall, the scheduled methods have consistent performance on the energy saving and cost reduction. However, in terms of the congestion reduction, the optimization-based method has the best performance. As shown in Figure 5-36, when operating the system based on price signal, the system shows a higher congestion than the temperature based method. The reason is that scheduled operation solely based on pricing signal does not consider the energy consumption aspect of the system, which is affected by the ambient temperature. When applying such method to congestion focus operation, it is possible that the time wise distribution of the energy consumption of the system becomes worse, which leads to a higher congestion. Therefore, in Figure 5-36, both scheduled methods could not reduce the congestion. The optimization-based method, on the contrary, evaluates the congestion function based on the entire forecast window. Therefore, it could seek for an operation sequence that reduces both the congestion and the energy consumption, as shown in Figure 5-36. Currently, the pricing information from the grid does not consider the effect of congestion reduction. However, the future grid incentive program is expected to include such features. Therefore, at this moment, the optimization-based method shows similar performance as scheduled methods in cooling operation. However, it is expected to have a better performance in the future when the congestion becomes one part of the incentive programs. Similarly, in the heating operation, the optimization-based method and the scheduled methods have

similar performance in terms of energy consumption and cost reduction. In the heating operation, PCM based TES serves as an evaporator during the peak period and is melt by the refrigerant flow in the off-peak period. The design of the system implicitly considers the reduction of the energy consumption gap between the peak period and off-peak period. Therefore, optimization-based method and scheduled methods have similar performance in congestion reduction. It indicates that, even if the congestion incentive program is introduced in the future, the difference between the operation methods in the heating season will not be significant.

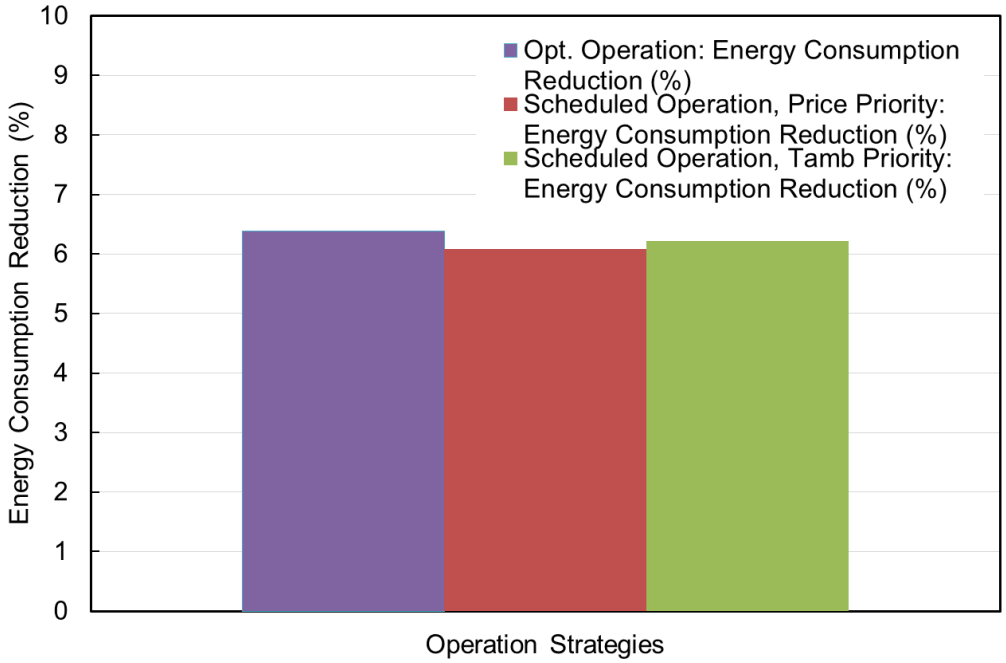

Figure 5-34 Cooling: effect of operation strategy on design month energy saving

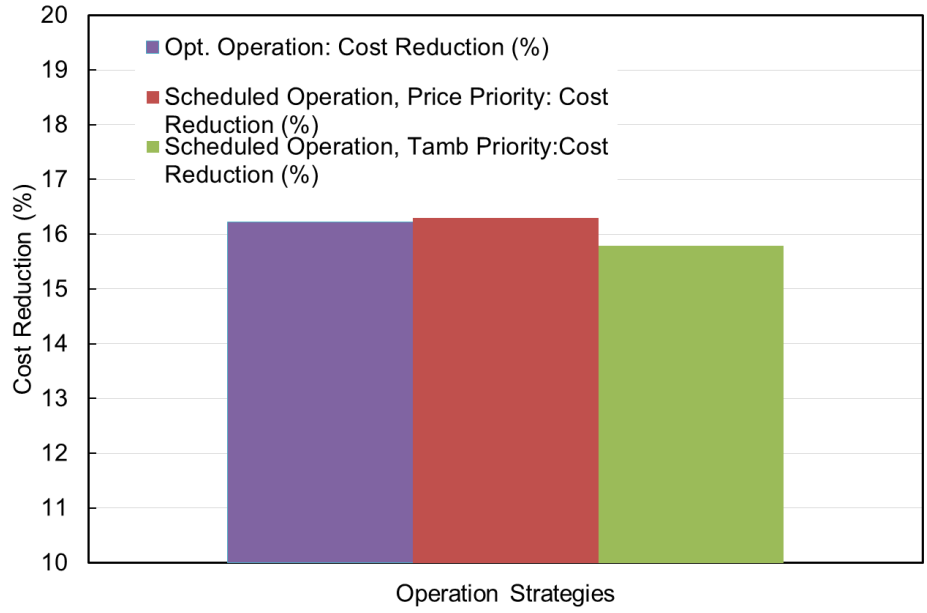

Figure 5-35 Cooling: effect of operation strategy on design month cost reduction

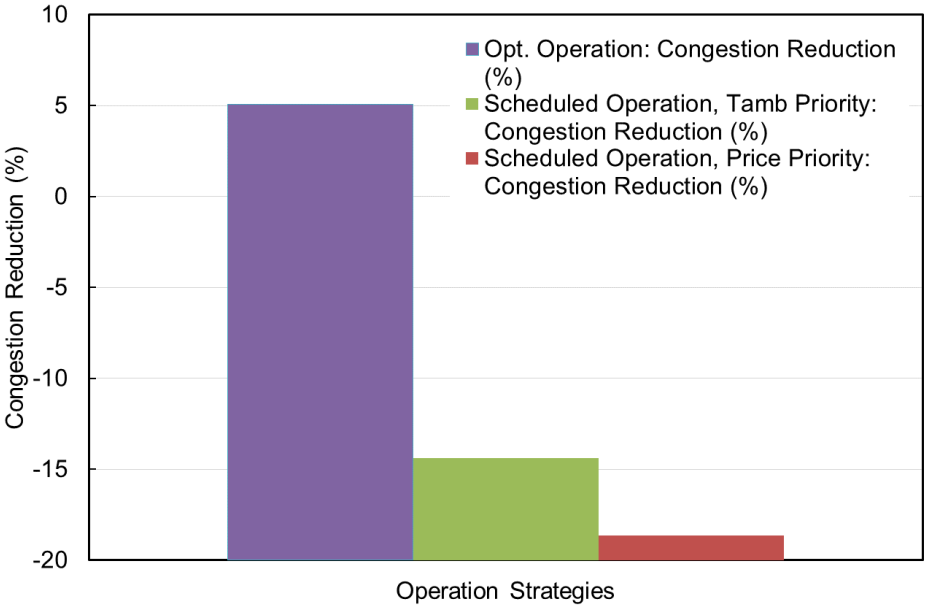

Figure 5-36 Cooling: effect of operation strategy on design month congestion reduction

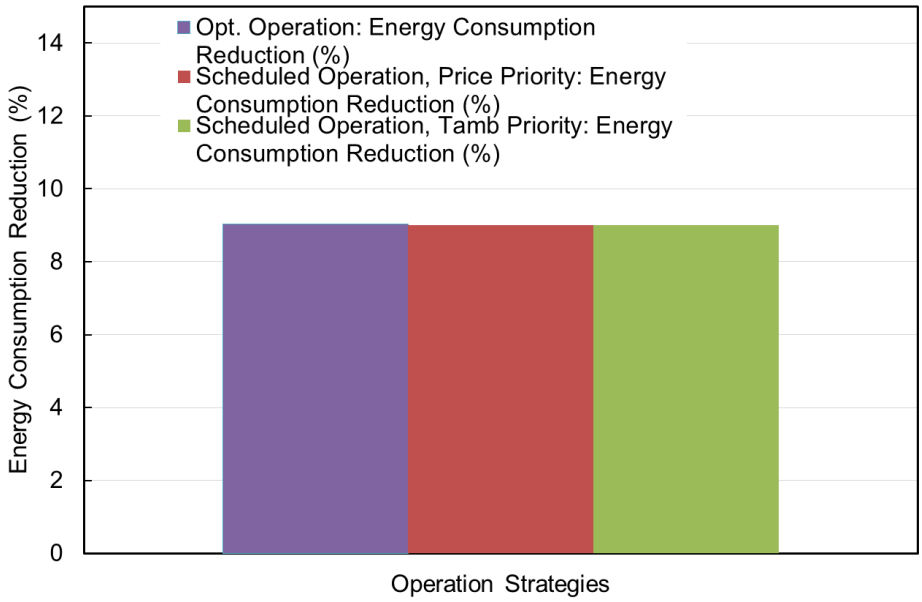

Figure 5-37 Heating: effect of operation strategy on design month energy saving

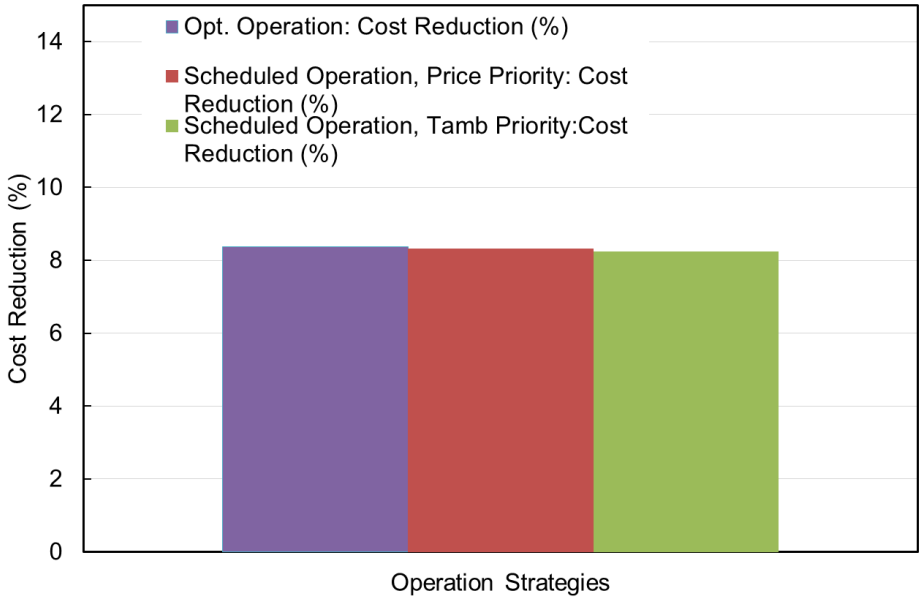

Figure 5-38 Heating: effect of operation strategy on design month cost reduction

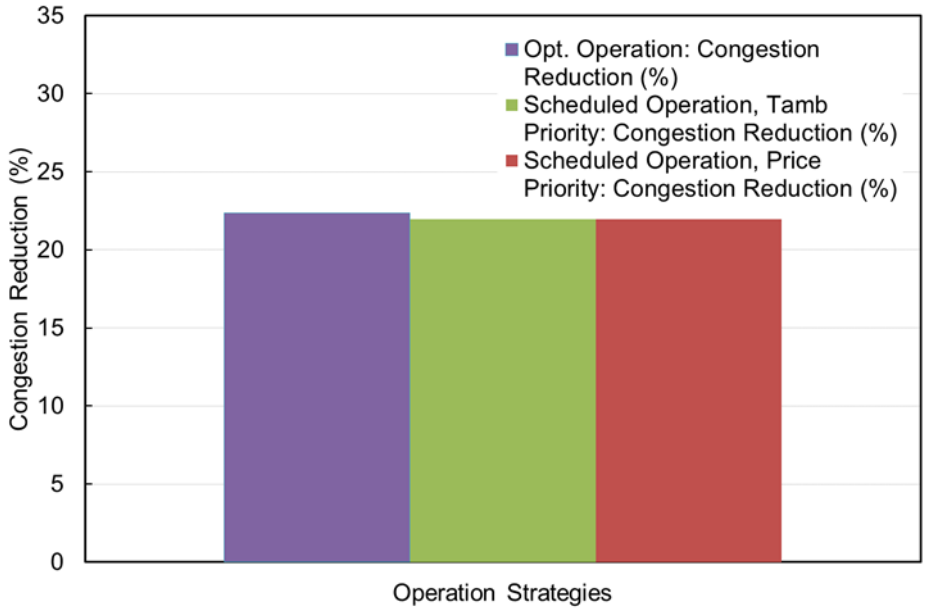

Figure 5-39 Heating: effect of operation strategy on design month congestion reduction

5.5.1.4 Effect of Incentive Program

Operation of the system is also affected by the incentive program. In this study, for both cooling and heating operation, different incentive programs were compared to see their influence on the cost reduction potential of the new VRF system with PCM based TES. Table 5-7 and Table 5-8 show five incentive programs in cooling operation and heating operation, respectively. In both cooling and heating operation, three ToU programs of different peak period ratio and one ToU program with critical peak pricing are considered, in addition to the day ahead real-time program. In cooling season, program #2 is the current ToU program provided by Baltimore Gas and Electric (BGE). In heating season, program #1 is the current ToU program. The results are shown in Figure 5-40 and Figure 5-41. During the cooling design month, the system achieves the lowest cost reduction when it is attending program #1. That is due to the fact that

program #1 has the lowest peak period ratio. With the increase of peak period ToU ratio, the cost reduction increases. When the program considers the peak period pricing, the system could achieve a cost reduction as high as 15%. After introducing the real-time pricing program, the cost reduction could further increase to 16%. From Figure 5-40, it can be seen that the system is most suitable for a real-time program. If used under a ToU program, it could has more cost reduction benefit only when there is a bigger difference between the peak and off-peak period. The effect of programs on the heating cost reduction is shown in Figure 5-41. In Figure 5-41, it is found that variation of cost reduction along with the change of programs is less than 1% in heating operation. Therefore, the impact of incentive programs in heating season is not significant.

Table 5-7 Cooling incentive programs

	Cooling Season Incentive Programs
Program #0	Day ahead real-time program
Program #1	ToU Ratio 1.3
Program #2	ToU Ratio 1.6 (Current Program)
Program #2+CPP	ToU Ratio 1.6+CPP
Program #3	ToU Ratio 2

Table 5-8 Heating incentive programs

	Heating Season Incentive Programs
Program #0	Day ahead real-time program
Program #1	ToU Ratio 1.3 (Current ToU Program)
Program #2	ToU Ratio 1.6
Program #2+CPP	ToU Ratio 1.3+CPP
Program #3	ToU Ratio 2

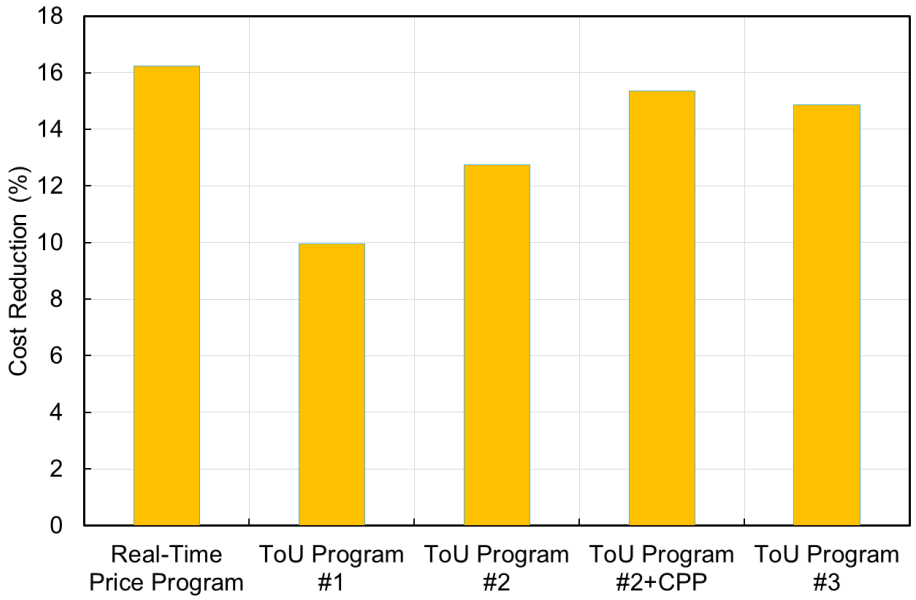

Figure 5-40 Effect of cooling season incentive programs on cost reduction

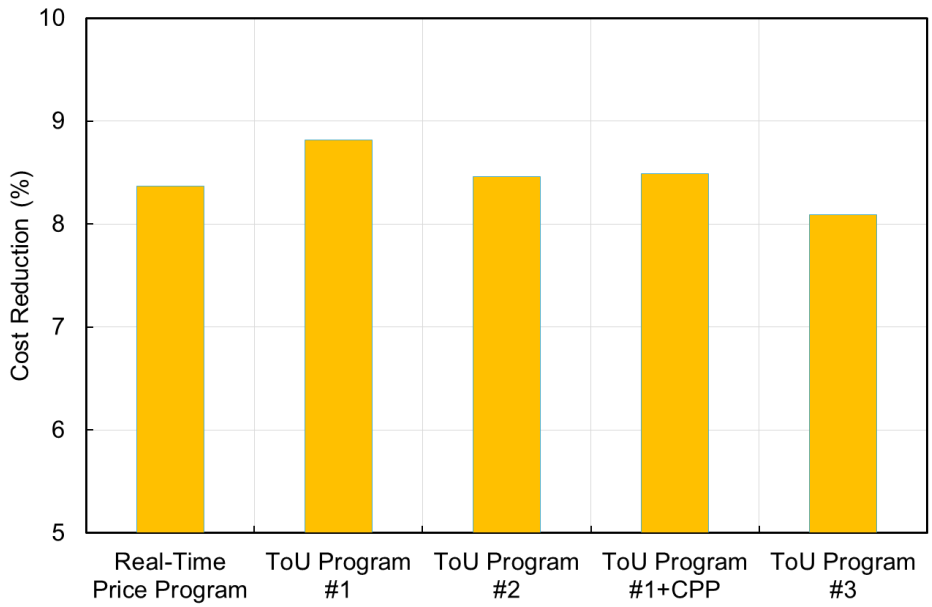

Figure 5-41 Effect of heating season incentive programs on cost reduction

5.5.2 Economic Analysis

As compared to conventional TES systems, the new VRF system with PCM based TES has the advantage that the same TES is used for both cooling and heating operation. In order to achieve the same functionality, the conventional TES system needs to have both cooling season TES and heating season TES. The conventional ice storage could only serve the cooling season. In the heating season, high temperature storage such as hot water needs to be used. To realize the same functionality as the new VRF system with PCM based TES, an ice storage system and hot water system need to be used together. It is assumed that the ice storage system needs a chiller to generate ice and the hot water system needs a heat pump water heater to provide the hot water. The cost comparison between new VRF system with PCM based TES and conventional system is shown in Table 5-9. As can be seen in Table 5-9, the new VRF system with PCM

based TES has a higher cost due to the high cost of PCM. However, PCM based TES has a volume 56% smaller than the conventional system.

From the design month analysis, it could be seen that the new VRF system with PCM based TES could reduce energy consumption, electric cost and grid congestion in both cooling and heating season. In heating operation, the difference between scheduled and optimization-based operation method does not affect the performance of the system. In the cooling season, the selection of operation methods does not affect the energy saving and cost reduction potential.

In this study, the monthly cost savings of the new VRF system when compared to baseline system is shown in Figure 5-42. In Figure 5-42, to ensure the highest annual cost reduction, the incentive program is assumed to be day ahead real-time program and the operation strategy is assumed to be generated by optimization-based method. New VRF system with PCM based TES achieves the highest cooling season cost reduction from June to August and the highest heating season from December to February due to high cooling and heating demand in the building. Overall, the system saves $527 annually. With a total system cost of $6,930, as shown in Table 5-9, the payback period is 13.1 yrs. As mentioned before, the cost reduction of the system is affected by the incentive program. In the real-time pricing program, when the gap between the peak and off-peak is doubled, the annual cost saving is shown in Figure 5-43. As can be seen in Figure 5-43, the increase of cost reduction in the heating season is less significant than that of the cooling season, which is also consistent with the results observed during the design month analysis. In Figure 5-43, the annual cost reduction increases to $980 and the payback period is reduced to 7 yrs.

Table 5-9 Cost comparison between new system and conventional system

	PCM based TES	Ice Storage + Hot Water Storage	
Volume (m^3)	1.1	0.5	2.0
Cost ($)	PCM based TES	Ice Storage	Hot Water Storage
Storage Material Cost ($)	5420	N/A	N/A
System Installation Cost ($)	1510	880	1228
Chiller or HPWH Cost ($)	N/A	2565	1169
Overall Cost ($)	6930	5842	

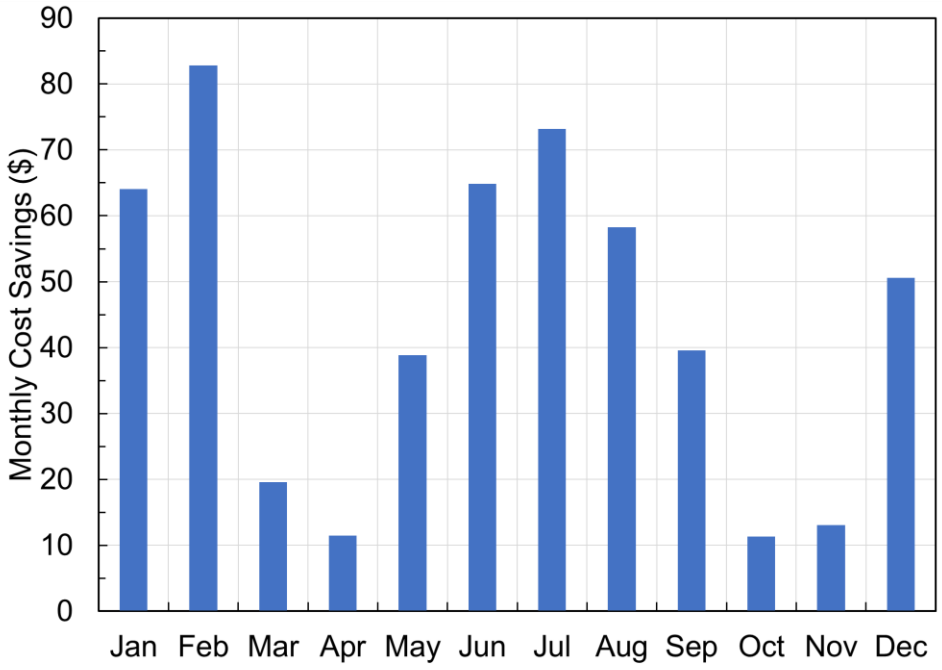

Figure 5-42 Monthly cost savings with day ahead real-time incentive program

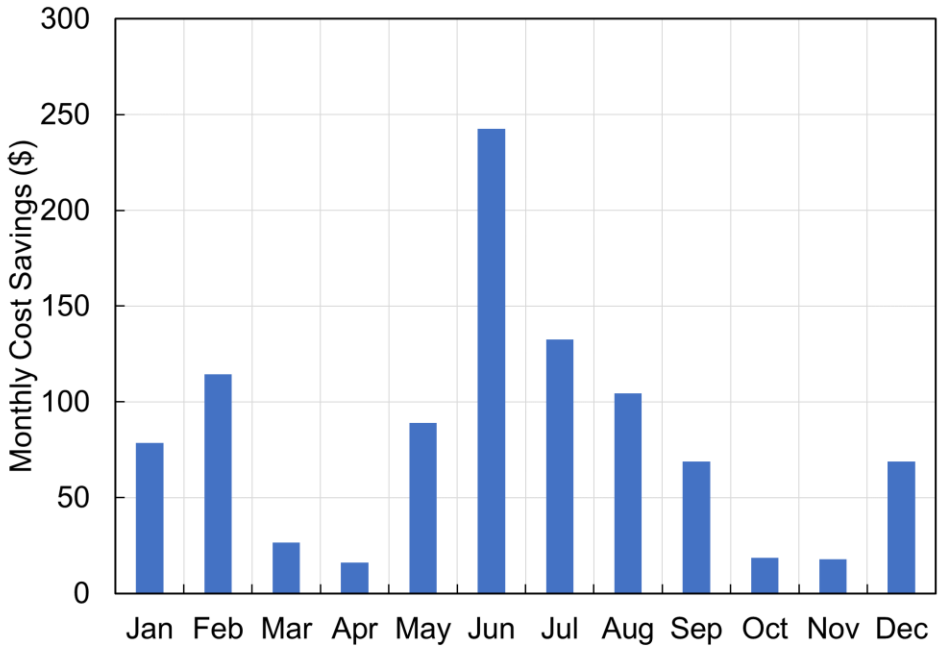

Figure 5-43 Monthly cost savings with day ahead real-time incentive program (double gap)

6 Conclusions and Future Work

6.1 Conclusions

VRF system is a popular building air conditioning system. This dissertation carried out a comprehensive literature review of the existing studies of VRF system, including both experimental work and simulation studies. Based on the literature review, it was found that the previous studies did not reveal the reasons behind the energy savings of VRF system in HR operation and water heating operation. Moreover, the existing dynamic models of VRF system could not achieve an accurate estimation of the system performance. In addition, the mismatch between the building load and the cooling/heating capability of air conditioning system has been a longstanding challenge. However, the concept of integrating TES in VRF system for both cooling and heating operation has not been investigated yet. This work set up a field testing facility of a MFVRF system, which could provide space cooling, heating, and water heating simultaneously, to investigate the effect of HR operations and water heating operation. The experimental work showed that the daily performance factor of the system could be increased by 20.4% in cooling main mode and 7.3% in heating main mode by water heating operation. This was mainly due to the improved HRR, reduced pressure ratio and improved compressor cycling performance. The effect of HR operation was investigated in heating and shoulder season. It was found that the PLR of the system was increased by the HR operation. Meanwhile, the discharge pressure and pressure ratio both decreased.

In the dynamic model, a MFVRF model was developed to simulate the performance of the system in cooling and heating season. The comparison between the experimental data and simulation results showed that the missing of capacity modulation characteristics of the compressor was the reason behind the insufficiency of existing models. A new VRF model based on thermodynamic principles was developed in this work. The new model estimated the hourly energy consumption of the VRF system with a deviation less than 5%. When compared to conventional VRF models, another advantage of the new model was the capability of taking new operation strategies and system configurations into consideration. A cooling and heating energy saving control based on ambient temperature was estimated with the new model. It was found that it could achieve a highest cooling season energy savings of 10.8% in Chicago and highest heating season energy savings of 15.4% in Baltimore. Moreover, due to low water utilization in MFVRF system, a VRF system using CWS as heat sink in the summer peak period was proposed and investigated. The seasonal performance of VRF system with CWS was also estimated with the new model. It was found that the highest cooling season energy savings of the new VRF system with CWS could achieve was 12.5% in Houston.

To solve the mismatch between the building load and the capability of building air conditioning system, a new VRF system with PCM based TES device was proposed. The key concept of the new VRF system with PCM based TES is to utilize the same TES for both cooling and heating operation. In the cooling season, PCM based TES device directly provides cooling to the rooms. In the heating season, PCM based TES is used as an evaporator to reduce the defrosting operation and increase the evaporating

temperature of the VRF system. Due to the load-shifting feature of PCM based TES, the system is able to achieve both EE and DR domain targets. The concept of the new VRF system with PCM based TES was firstly evaluated to investigate the effect of melting temperature of the PCM. Based on the preliminary analysis, the melting temperature of PCM based TES was selected to be 8°C. Based on the cooling load of the building, a PCM integrated heat exchanger which could provide an hourly average solidification of 15 kWh was designed based on the analytical model of the solidification process. Fin efficiency and the magnitude of the natural convection were discussed and quantified. Based on the discussion, a semi-analytical model was created to simulate the solidification and melting process of PCM based TES. The TES model was thereafter incorporated into the new VRF model to investigate the performance of the system in cooling and heating season. Cooling and heating design month analysis showed that the system could achieve 6.5% and 9% of energy saving in cooling and heating operation, respectively. Since the operation strategy and the incentive program are two keys aspects in system operation, the effects of different operation strategy generation methods and incentive programs were investigated. The results show that scheduled method and optimization-based method achieve similar performance in heating operation. In cooling season, scheduled method and optimization-based method show similar performance in energy saving and cost reduction. However, the optimization-based method has more advantages in congestion reduction. For the effect of incentive programs, it was found that the new VRF system with PCM based TES could achieve the best cooling season cost reduction when attending real-time incentive programs. However, in heating season, the effect of incentive program was found to be

insignificant. Cost of the new VRF system with PCM based TES was compared to that of the conventional system with ice storage and hot water storage. The cost of the new VRF system with PCM based TES was higher than conventional system due to the high cost of PCM. Economic analysis was thereafter carried out. With the current real-time incentive programs, the payback period was found to be 13.1 yrs. However, when the gap between peak and off-peak period was doubled, the payback period could be reduced to 7 yrs.

6.2 Future Work

Outside the work covered in this dissertation, the following research could be studied further and should be of significance in the near future:

- The future research should take the humidity and air quality control of VRF systems into consideration. At this moment, one of the challenges of VRF system is the insufficient ventilation when compared to conventional systems. It is usually solved by including extra ventilation systems. However, from the aspect of VRF system, the flexibility of system architecture indicates there is still possibility to realize simultaneous control of room temperature and humidity as well as the indoor air quality within the scope of VRF system. However, experiment and simulation research of such comprehensive VRF systems have not been found yet.
- In the building application, it is also necessary to consider the behavior of the occupants. In the existing studies, the operation of the building and VRF system considers a fixed occupant schedule. However, the future studies should take

the behavior of the occupants into the consideration when estimating the load of the building. This factor becomes even more important in the decision making process of DR and EE operation.

- The coordination of passive and active TES. With the development of building technology and VRF systems, it could be forecasted that more and more VRF systems will be used in green buildings or smart buildings. One feature of these buildings is the introduction of advanced building structures such as PCM embedded wallboards and green rooftop. In these buildings, it is necessary to consider the both active TES and passive TES to achieve the maximal benefit from grid incentive programs.
- The comparison between GSHP and VRF system when considering the integration of TES. Nowadays, both systems become more and more popular. There are several studies comparing the performance of the two systems when installed in the office building. However, when considering the integration of TES, there is no such study that compares the two systems when both systems are used in the demand side management market.

6.3 Contributions

6.3.1 List of Contributions

This dissertation covers experimental study and simulation research of novel VRF system. In the experimental study of VRF system, the contributions are listed as follows:

- Analyze and quantify the effect of heat recovery operation through the field test of MFVRF.
- Analyze and quantify the effect of water heating operation through the field test of MFVRF.

In the simulation research, the contributions are as follows:

- Analyze and discuss the source of deviation of existing VRF models.
- Develop a new VRF model with higher accuracy.
- Investigate the seasonal performance of cooling/heating season energy saving control and VRF system with chilled water storage.

In the new VRF system, the contributions are as follows:

- Develop a new VRF system with single PCM based TES that supports both cooling and heating season operation.
- Investigate EE and DR potential of the new VRF system.
- Investigate the effect of operation strategy and incentive programs on the new VRF system with PCM based TES.

6.3.2 List of Publications

Journal papers:

Lin, X., H. Lee, Y. Hwang, and R. Radermacher. 2015. A Review of Recent Development in Variable Refrigerant Flow Systems. *Science and Technology for the Built Environment* 21, no. 7: 917-933.

Lin, X., H. Lee, Y. Hwang, R. Radermacher, and S. Oh. 2015. Field Test of Multi-Functional Variable Refrigerant Flow System. *Science and Technology for the Built Environment* 21, no. 5: 648–657.

Lin, X., H. Lee, Y. Hwang, R. Radermacher, and B. Kim. 2016. A New Variable Refrigerant Flow System Simulation Approach in EnergyPlus. *International Journal of Air-Conditioning and Refrigeration* 24, no.1: 1650001.

Co-authored journal papers:

Lee, H., X. Lin, Y. Hwang, and R. Radermacher. 2016. Performance Investigation on Solid Desiccant Assisted Mobile Air Conditioning System. *Applied Thermal Engineering* 103: 1370–1380.

Conference papers:

Lin, X., H. Lee, Y. Hwang, R. Radermacher, J. Kwon, and C. Kwon. 2014. Experimental Investigation of Desiccant Wheel Assisted MAC System. In *SAE World Congress & Exhibition*. Detroit.

Lin, X., H. Lee, Y. Hwang, R. Radermacher, S. Oh, C. Park, G.L. Martin, and H. Bldg. 2014. Experimental Investigation of Multi-Functional Variable Refrigerant Flow System. In *International Refrigeration and Air Conditioning Conference*. West Lafayette.

Lin, X., Y. Hwang, R. Radermacher, and S. Oh. 2016. Review of Temperature and Humidity Control Technology for Heat Pump and Air Conditioning Systems. In *International Refrigeration and Air Conditioning Conference*. West Lafayette.

Lin, X., Y. Hwang, R. Radermacher, and B. Kim. 2017. Performance of Chilled Water Storage Assisted Variable Refrigerant Flow System. In *12th IEA Heat Pump Conference*. Rotterdam.

Lin, X., Y. Hwang, R. Radermacher, and B. Kim. 2017. A New Control Strategy for Variable Refrigerant Flow Systems. In *Building Simulation Applications 2017*. South Tyrol.

Abbreviation

AC	air conditioning
COP	coefficient of performance
CPP	critical peak pricing
CvRMSE	coefficient of variation of root mean square error
DOE-2	“Department of Energy”-2
DR	demand response
DPF	daily performance factor
DVM	digital variable multiple
EE	energy efficiency
EER	energy efficiency ratio
EEV	electronic expansion valve
eQUEST	Quick Energy Simulation Tool
ERV	energy recovery ventilator
FDD	fault detection and diagnosis
GSHP	ground source heat pump
HP	heat pump
HPF	hourly performance factor
HR	heat recovery

HRR	heat recovery ratio
HRU	heat recovery unit
HX	heat exchanger
IAQ	indoor air quality
IU	indoor unit
IPLV	integrated part load value
IDVS	integrated solid desiccant heat pump and VRF system
IHVS	integrated heat recovery ventilation and VRF system
JIS	Japanese Industrial Standards
MCU	mode change unit
MEAC	multi-evaporator air conditioning
MFVRF	multi-functional variable refrigerant flow
NMBE	normalized mean bias error
OAP	outdoor air processor
OA	outdoor air
OU	outdoor unit
OUHX	outdoor unit heat exchanger
PCM	phase change material
PID	proportional integral derivative
PLR	part load ratio
PWM	pulse width modulation
RH	relative humidity
SDHP	solid desiccant heat pump

SCHX	subcooler heat exchanger
SEER	seasonal energy efficiency ratio
TES	thermal energy storage
ToU	time-of-use
TRNSYS	Transient System Simulation Tool
VAV	variable air volume
VRF	variable refrigerant flow
VRV	variable refrigerant volume
WHU	water heating unit

Symbols

A_b	base plate area
A_f	fin area
A_f	total heat transfer area
$ApprT$	approach temperature at the condenser outlet
b	tube thickness
C_1	WHU capacity correction factor #1
C_2	WHU capacity correction factor #2
C_d	flow coefficient
C_p	specific heat
$Energy_{exp,hr}$	hourly experimental cooling/heating energy consumption

$Energy_{sim,hr}$ hourly simulated cooling/heating energy consumption

$Energy_{exp,day}$ daily average experimental cooling/heating energy consumption

$Energy_{sim,day}$ daily average simulated cooling/heating energy consumption

ff_{water} dimensionless flow rate

$Flow_{actual}$ actual flow rate

$Flow_{rated}$ rated flow rate

f compressor frequency

f_s compressor frequency given in performance table

F_v mass flow rate correction factor due to superheat

F equivalent heat transfer area enhance ratio

g gravitational acceleration

h_i enthalpy of refrigerant

$h_{PCM,conv}$ natural convection heat transfer coefficient of PCM

h_{eqv} conduction equivalent convection heat transfer coefficient

hr hour

h_{ref} phase changer material heat exchanger refrigerant inlet enthalpy

Δh enthalpy difference across the indoor unit

I_i ith order modified second type Bessel function

i segment number

j time step

K_i ith order modified second type Bessel function

k_{PCM} phase change material thermal conductivity

L	specific energy storage capability per volume
l_c	fin spacing
l_f	fin length
MFR_{rated,f_s}	mass flow rate of compressor under rated condition and f_s
$MFR_{rated,f}$	mass flow rate of compressor under rated condition and f
m	hours where the TES is active
$\dot{m}_i$	refrigerant mass flow rate in indoor unit
$\dot{m}_{total}$	total mass flow rate
n	number of experimental data points/ hours where the TES is not active
N	fin density
Nu	Nussel number
PD	compressor suction line pressure drop
$Power_{rated,f_s}$	compressor power under rated condition and f_s
$Power_{rated,f}$	compressor power under rated condition and f
$\bar{P}_{OU,hr}$	average outdoor unit hourly energy consumption
$\bar{P}_{IU,hr}$	average indoor units hourly energy consumption
$\bar{P}_{Pump,hr}$	average water pump hourly energy consumption
$\bar{Q}_{whu,rated}$	WHU rated capacity
$\dot{Q}_{sc}$	space cooling load
$\dot{Q}_{sh}$	space heating load
$\dot{Q}_{whu}$	WHU real capacity
$\dot{Q}_c$	condensing capacity

$\dot{Q}_e$ evaporating capacity

$\bar{Q}_{cooling/heating}$ calculated cooling or heating capacity of indoor unit

$\bar{Q}_{total,cooling,hr}$ hourly averaged all IU cooling energy

$\bar{Q}_{total,heating,hr}$ hourly averaged all IU heating energy

$\bar{Q}_{waterheating,hr}$ hourly averaged water heating energy

$\bar{Q}_{exp,hr}$ hourly averaged experimental cooling/heating energy

$\bar{Q}_{sim,hr}$ hourly averaged simulated cooling/heating energy

$E_{exp,day}$ daily experimental cooling/heating energy consumption

$E_{sim,day}$ daily simulated cooling/heating energy consumption

$\dot{Q}_{in}$ fin segment inlet heat flow

$\dot{Q}_{out}$ fin segment outlet heat flow

$\dot{Q}_{conv}$ fin segment convection heat flow

$\dot{Q}_{conv}$ fin segment conduction heat flow

$\dot{q}(t)$ time wise melting/solidification power

R thermal resistance

R_0 tube outer diameter

Ra Rayleigh number

R_i calculated mass flow rate / tube inner diameter

s_t one-dimension solidification analysis front position

$s_{y,t}$ two-dimension solidification analysis y-direction front position

s' normalized two-phase front

SC subcooling

SH	superheat
T_{amb}	outdoor air temperature
T_c	condensing temperature
T_e	evaporating temperature
$T_{whu,in}$	WHU inlet water temperature
$T_{whu,out}$	WHU oulet water temperature
$T_{c,cool}$	condensing temperature in cooling mode
$T_{c,heat}$	condensing temperature in heating mode
$T_{c,set}$	Built-in condensing temperature set point
T_s	phase change material melting temperature
T_o	heat transfer fluid temperature
t	testing duration/time
$T_{w,in}$	water inlet temperature of plate heat exchanger
$T_{w,out}$	water outlet of plate heat exchanger
y_i	simulation results/segment phase change material front position
$\widehat{y_i}$	experimental results
ΔP_i	pressure difference through expansion valve
ρ_i	density at the inlet of expansion valve
ε	tolerance
η_{fin}	overall fin efficiency
η_{fs}	single fin efficiency
Δh_{real}	refrigerant enthalpy change across compressor in real condition

Δh_{rated}	refrigerant enthalpy change across compressor in rated condition
ρ	refrigerant density at compressor suction port
ρ_{rated}	refrigerant density at compressor suction port under rated condition
$\epsilon_{cap,hr}$	hourly cooling/heating capacity absolute deviation in percentage
$\epsilon_{energy,hr}$	hourly cooling/heating energy absolute deviation in percentage
$\epsilon_{cap,day}$	daily average cooling/heating capacity absolute deviation
$\epsilon_{energy,hr}$	daily average cooling/heating energy absolute deviation
$\Phi_{new,system}$	energy/cost function of new VRF system
$\Phi_{baseline}$	energy/cost function of baseline VRF system
Ψ	congestion of new VRF system or baseline VRF system
ρ_s	density of solid PCM
δ	fin thickness
μ	viscosity
β_v	volumetric expansion coefficient
x	radial fin distance
x_{norm}	normalized radial fin distance
θ	normalized fin temperature difference

Reference

Al-Abidi, A.A., S. Bin Mat, K. Sopian, M.Y.Y. Sulaiman, C.H.H. Lim, and A. Th. 2012. Review of Thermal Energy Storage for Air Conditioning Systems. *Renewable and Sustainable Energy Reviews* 16, no. 8: 5802–5819.

Arteconi, A., N.J. Hewitt, and F. Polonara. 2012. State of the Art of Thermal Storage for Demand-Side Management. *Applied Energy* 93: 371–389.

Arteconi, A., N.J.J. Hewitt, and F. Polonara. 2013. Domestic Demand-Side Management (DSM): Role of Heat Pumps and Thermal Energy Storage (TES) Systems. *Applied Thermal Engineering* 51, no. 1–2: 155–165.

ASHRAE. 2002. *ASHRAE Guideline 14-Measurement of Energy and Demand Savings*. Atlanta: American Society of Heating, Refrigerating and Air-conditioning Engineers, Inc.

ASHRAE. 2013. *ANSI/ASHRAE/IES Standard 90.1-2013 Energy Standard for Buildings Except Low-Rise Residential Buildings*. Atlanta: American Society of Heating, Refrigerating and Air-conditioning Engineers, Inc.

Aynur, T., Y. Hwang, and R. Radermacher. 2008. Simulation Evaluation of the Ventilation Effect on the Performance of a VRV System in Cooling Mode—Part II, Simulation Evaluation. *HVAC&R Research* 14, no. 5: 783–795.

Aynur, T.N. 2008. Experimental and Simulation Evaluation of a Multi-Split Type Air Conditioning System Under Steady-State and Transient Conditions. University of Maryland, College Park.

Baehr, H.D., and K. Stephan. 1995. *Wärme- Und Stoffübertragung*. *Springer-Verlag*.

Wiley-VCH Verlag GmbH & Co. KGaA.

Benli, H. 2011. Energetic Performance Analysis of a Ground-Source Heat Pump System with Latent Heat Storage for a Greenhouse Heating. *Energy Conversion and Management* 52, no. 1: 581–589.

Bergman, T.L., A.S. Lavine, F.P. Incropera, and D.P. DeWitt. 2011. *Fundamentals of Heat and Mass Transfer.* 7th ed. Wiley.

Cabeza, L.F.F., A. Castell, C. Barreneche, A. de Gracia, and A.I.I. Fernández. 2011. Materials Used as PCM in Thermal Energy Storage in Buildings: A Review. *Renewable and Sustainable Energy Reviews* 15, no. 3: 1675–1695.

Chen, W., X. Zhou, and S. Deng. 2005. Development of Control Method and Dynamic Model for Multi-Evaporator Air Conditioners (MEAC). *Energy Conversion and Management* 46, no. 3: 451–465.

Cheung, H., and J.E. Braun. 2014. Component-Based, Gray-Box Modeling of Ductless Multi-Split Heat Pump Systems. *International Journal of Refrigeration* 38:30–45.

Dabiri, A.E., and C.K. Rice. 1987. A Compressor Simulation Method with Corrections for the Level of Suction Gas Superheat. *ASHRAE Transactions* 2: 771–782.

Department of Energy. 2012. *2011 Buildings Energy Data Book.* http://buildingsdatabook.eren.doe.gov/ChapterIntro1.aspx.

Diaconu, B.M. 2012. Energy Analysis of a Solar-Assisted Ejector Cycle Air Conditioning System with Low Temperature Thermal Energy Storage. *Renewable Energy* 37, no. 1: 266–276.

Dieckmann, J.H. 2016. Latent Heat Storage in Concrete.

Dittus, F.W., and L.M.K. Boelter. 1985. Heat Transfer in Automobile Radiators of the

Tubular Type. *International Communications in Heat and Mass Transfer* 12, no. 1: 3–22.

Eftekhar, J., A. Sheikh, and D. Lou. 1984. Heat Transfer Enhancement in a Paraffin Wax Thermal Storage System. *Solar Energy Engineering* 106: 299–306.

Fang, G., S. Wu, and X. Liu. 2010. Experimental Study on Cool Storage Air-Conditioning System with Spherical Capsules Packed Bed. *Energy and Buildings* 42, no. 7: 1056–1062.

Fujimoto, I., K. Ueno, K. Saito, K. Ohno, H. Murata, and H. Nakamura. 2011. Performance Evaluation of VRF Systems. In *International Congress of Refrigeration*.

Goldman, C., M. Reid, L. Roger, and S. Alison. 2010. *Coordination of Energy Efficiency and Demand Response*.

Gu, Z., H. Liu, and Y. Li. 2004. Thermal Energy Recovery of Air Conditioning System - Heat Recovery System Calculation and Phase Change Materials Development. *Applied Thermal Engineering* 24, no. 17–18: 2511–2526.

Hamada, Y., M. Nakamura, and H. Kubota. 2007. Field Measurements and Analyses for a Hybrid System for Snow Storage/melting and Air Conditioning by Using Renewable Energy. *Applied Energy* 84, no. 2: 117–134.

Hong, T., X. Pang, O. Schetrit, L. Wang, S. Kasahara, Y. Yura, and R. Hinokuma. 2014. A New Model to Simulate Energy Performance of VRF Systems. In *ASHRAE Summer Conference*. Seattle.

Jiang, Y., T. Ge, and R. Wang. 2013. Performance Simulation of a Joint Solid Desiccant Heat Pump and Variable Refrigerant Flow Air Conditioning System in

EnergyPlus. *Energy and Buildings* 65: 220–230.

Jiang, Y., T. Ge, and R. Wang. 2014. Comparison Study of a Novel Solid Desiccant Heat Pump System with EnergyPlus. *Building Simulation* 7, no. 5: 467–476.

Jiang, Y., T. Ge, R. Wang, and Y. Huang. 2014a. Experimental Investigation on a Novel Temperature and Humidity Independent Control Air Conditioning System – Part I: Cooling Condition. *Applied Thermal Engineering* 73, no. 1: 782–791.

Jiang, Y., T. Ge, R. Wang, and Y. Huang. 2014b. Experimental Investigation on a Novel Temperature and Humidity Independent Control Air Conditioning System – Part II: Heating Condition. *Applied Thermal Engineering* 73, no. 1: 773–781.

Joo, Y., H. Kang, J.H. Ahn, M. Lee, and Y. Kim. 2011. Performance Characteristics of a Simultaneous Cooling and Heating Multi-Heat Pump at Partial Load Conditions. *International Journal of Refrigeration* 34, no. 4: 893–901.

Jung, D.S., M. McLinden, R. Radermacher, and D. Didion. 1989. A Study of Flow Boiling Heat Transfer with Refrigerant Mixtures. *International Journal of Heat and Mass Transfer* 32, no. 9: 1751–1764.

Kang, H., Y. Joo, H. Chung, Y. Kim, and J. Choi. 2009. Experimental Study on the Performance of a Simultaneous Heating and Cooling Multi-Heat Pump with the Variation of Operation Mode. *International Journal of Refrigeration* 32, no. 6: 1452–1459.

Kwon, L. 2013. Experimental Evaluation of a Multifunctional Variable Refrigerant Flow System in an Educational Office Building.

Kwon, L., Y. Hwang, R. Radermacher, and B. Kim. 2012. Field Performance Measurements of a VRF System with Sub-Cooler in Educational Offices for the

Cooling Season. *Energy and Buildings* 49: 300–305.

Kwon, L., Y. Hwang, R. Radermacher, L. Kwon, R. Radermacher, and B. Kim. 2012. Field Performance Measurements of VRF System with Subcooling Heat Exchanger. In *International Refrigeration and Air Conditioning Conference*. West Lafayette.

Kwon, L., H. Lee, Y. Hwang, R. Radermacher, and B. Kim. 2014. Experimental Investigation of Multifunctional VRF System in Heating and Shoulder Seasons. *Applied Thermal Engineering* 66, no. 1–2: 355–364.

Lamberg, P., and K. Sirén. 2017. Analytical Model for Melting in a Semi-Infinite PCM Storage with an Internal Fin.

Lee, M.P., B. Foster, D. Kathan, O. Meghan, P. April, and S. Periovi. 2016. *2016 Assessment of Demand Response and Advanced Metering*.

Li, G., Y. Hwang, and R. Radermacher. 2012. Review of Cold Storage Materials for Air Conditioning Application. *International Journal of Refrigeration* 35, no. 8: 2053–2077.

Li, T., R. Wang, and T. Yan. 2015. Solid–gas Thermochemical Sorption Thermal Battery for Solar Cooling and Heating Energy Storage and Heat Transformer. *Energy* 84: 745–758.

Li, Y., and J. Wu. 2010. Energy Simulation and Analysis of the Heat Recovery Variable Refrigerant Flow System in Winter. *Energy and Buildings* 42, no. 7: 1093–1099.

Lin, X., H. Lee, Y. Hwang, R. Radermacher, S. Oh. 2014. Experimental Investigation of Multi-Functional Variable Refrigerant Flow System. In *International Refrigeration and Air Conditioning Conference*, 1–10.

Liu, X., and T. Hong. 2010. Comparison of Energy Efficiency between Variable Refrigerant Flow Systems and Ground Source Heat Pump Systems. *Energy and Buildings* 42, no. 5: 584–589.

Long, J., and D. Zhu. 2008. Numerical and Experimental Study on Heat Pump Water Heater with PCM for Thermal Storage. *Energy and Buildings* 40, no. 4: 666–672.

Marshall R. 1979. Experimental Determination of Heat Transfer Coefficient in a Thermal Storage Containing a Phase Change Material- The Rectangular Cavity. In *International Conference on Future Energy Concept*.

Mehling Harald, and L.F. Cabeza. 2008. *Heat and Cold Storage with PCM*. Heat and Mass Transfer. Berlin, Heidelberg: Springer Berlin Heidelberg.

Nigusse, B., and R. Raustad. 2013. Verification of a VRF Heat Pump Computer Model in EnergyPlus. *ASHRAE Transactions* 119: 101-117.

Palensky, P., and D. Dietrich. 2011. Demand Side Management: Demand Response, Intelligent Energy Systems, and Smart Loads. *IEEE Transactions on Industrial Informatics* 7, no. 3: 381–388.

Pan, Y., X. Xu, L. Xia, and S. Deng. 2012. A Modeling Study on the Effects of Refrigerant Pipeline Length on the Operational Performance of a Dual-Evaporator Air Conditioning System. *Applied Thermal Engineering* 39: 15–25.

Parameshwaran, R., S. Harikrishnan, and S. Kalaiselvam. 2010. Energy Efficient PCM-Based Variable Air Volume Air Conditioning System for Modern Buildings. *Energy and Buildings* 42, no. 8: 1353–1360.

Parameshwaran, R., S. Kalaiselvam, S. Harikrishnan, and A. Elayaperumal. 2012. Sustainable Thermal Energy Storage Technologies for Buildings: A Review.

Renewable and Sustainable Energy Reviews 16, no. 5: 2394–2433.

Qi, Q., Y. Jiang, and S. Deng. 2008. A Simulation Study on Solar Energy Seasonal Storage by Phase Change Material. *2008 IEEE International Conference on Sustainable Energy Technologies*: 106–109.

Raustad, R. 2013. A Vriable Refrigerant Flow Heat Pump Computer Model in EnergyPlus. *ASHRAE Transactions* 119: 299–308.

Raustad, R., B. Nigusse, C. Sharma, J. Cummings, R. Domitrovic, and H. Upadhye. 2013. *Technical Subtopic 2.1:Modeling Variable Refrigerant Flow Heat Pump and Heat Recovery Equipment in EnergyPlus*.

Schossig, P., H.-M. Henning, S. Gschwander, and T. Haussmann. 2005. Micro-Encapsulated Phase-Change Materials Integrated into Construction Materials. *Solar Energy Materials and Solar Cells* 89, no. 2–3: 297–306.

Shah, M.M. 2013. General Correlation for Heat Transfer during Condensation in Plain Tubes: Further Development and Verification. *ASHRAE Transactions* 119: 3.

Shao, S., W. Shi, X. Li, and H. Chen. 2004. Performance Representation of Variable-Speed Compressor for Inverter Air Conditioners Based on Experimental Data. *International Journal of Refrigeration* 27, no. 8: 805–815.

Sharma, A., V.V. V Tyagi, C.R.R. Chen, and D. Buddhi. 2009. Review on Thermal Energy Storage with Phase Change Materials and Applications. *Renewable and Sustainable Energy Reviews* 13, no. 2: 318–345.

Sharma, C., and R. Raustad. 2013. Compare Energy Use in Variable Refrigerant Flow Heat Pumps Field Demostration and Computer Model. In *ASHRAE Annual Conference*. Denver.

Shen, B., and C.K. Rice. 2012. Multiple-Zone Variable Refrigerant Flow System Modeling and Equipment Performance Mapping. In *2012 ASHRAE Winter Conference*, 118:1–8.

Shen, B., C.K. Rice, T.P. Mcdowell, and V.D. Baxter. 2013. Energy Simulation of Integrated Multiple- Zone Variable Refrigerant Flow System. In *2013 ASHARE Annual Conference*, 1–9.

Shi, W. 2000. Research on Characteristics and Control Strategy of the Variable Refrigerant flow(VRF) Air Conditioning System. Tsinghua University.

Stritih, U., and V. Butala. 2010. Experimental Investigation of Energy Saving in Buildings with PCM Cold Storage. *International Journal of Refrigeration* 33, no. 8: 1676–1683.

Tu, Q., K. Dong, D. Zou, and Y. Lin. 2011. Experimental Study on Multi-Split Air Conditioner with Digital Scroll Compressor. *Applied Thermal Engineering* 31, no. 14–15: 2449–2457.

Tu, Q., Z. Feng, S. Mao, K. Dong, R. Xiao, and W. Song. 2010. Heating Control Strategy for Variable Refrigerant Flow Air Conditioning System with Multi-Module Outdoor Units. *Energy and Buildings* 42, no. 11: 2021–2027.

Tu, Q., J. Xu, Y. Feng, S. Mao, D. Guo, and J. He. 2012. Determination Criterion of Defrosting Condition for Variable Refrigerant Flow Air Conditioning System. *Energy and Buildings* 48: 61–70.

Wang, S. 2014. Energy Modeling of Ground Source Heat Pump vs. Variable Refrigerant Flow Systems in Representative US Climate Zones. *Energy and Buildings* 72: 222–228.

Yan, T., R. Wang, T. Li, L. Wang, and I.T. Fred. 2015. A Review of Promising Candidate Reactions for Chemical Heat Storage. *Renewable and Sustainable Energy Reviews* 43: 13–31.

Yau, Y.H., and B. Rismanchi. 2012. A Review on Cool Thermal Storage Technologies and Operating Strategies. *Renewable and Sustainable Energy Reviews* 16, no. 1: 787–797.

Zhai, X., X. Wang, T. Wang, and R. Wang. 2013. A Review on Phase Change Cold Storage in Air-Conditioning System: Materials and Applications. *Renewable and Sustainable Energy Reviews* 22: 108–120.

Zhang, D., X. Zhang, and J. Liu. 2011. Experimental Study of Performance of Digital Variable Multiple Air Conditioning System under Part Load Conditions. *Energy and Buildings* 43, no. 6: 1175–1178.

Zhao, D., X. Zhang, and M. Zhong. 2015. Variable Evaporating Temperature Control Strategy for VRV System under Part Load Conditions in Cooling Mode. *Energy and Buildings* 91: 180–186.

Zhou, Y., and R. Wang. 2006. Module Development and Simulation of the Variable Refrigerant Flow Air Conditioning System under Cooling Conditions in Energyplus. In *International Conference for Enhanced Building Operations*. Shenzhen.

Zhou, Y., J. Wu, R. Wang, and S. Shiochi. 2007. Energy Simulation in the Variable Refrigerant Flow Air-Conditioning System under Cooling Conditions. *Energy and Buildings* 39, no. 2: 212–220.

Zhou, Y., J. Wu, R. Wang, S. Shiochi, and Y.M Li. 2008. Simulation and Experimental

Validation of the Variable-Refrigerant-Volume (VRV) Air-Conditioning System in EnergyPlus. *Energy and Buildings* 40, no. 6: 1041–1047..

Zhu, Y., X. Jin, Z. Du, B. Fan, and X. Fang. 2014. Simulation of Variable Refrigerant Flow Air Conditioning System in Heating Mode Combined with Outdoor Air Processing Unit. *Energy and Buildings* 68: 571–579.

Zhu, Y., X. Jin, Z. Du, B. Fan, and S. Fu. 2013. Generic Simulation Model of Multi-Evaporator Variable Refrigerant Flow Air Conditioning System for Control Analysis. *International Journal of Refrigeration* 36, no. 6: 1602–1615.

Zhu, Y., X. Jin, Z. Du, X. Fang, and B. Fan. 2014. Control and Energy Simulation of Variable Refrigerant Flow Air Conditioning System Combined with Outdoor Air Processing Unit. *Applied Thermal Engineering* 64, no. 1–2: 385–395.

Zhu, Y., X. Jin, X. Fang, and Z. Du. 2014. Optimal Control of Combined Air Conditioning System with Variable Refrigerant Flow and Variable Air Volume for Energy Saving. *International Journal of Refrigeration* 42: 14–25.